VILNIUS UNIVERSITY
CENTER FOR PHYSICAL SCIENCES AND TECHNOLOGY

SAULIUS TUMĖNAS

OPTICAL RESPONSE OF ZnMgRE QUASICRYSTALS

Doctoral Dissertation
Physical sciences, Physics (02P), Semiconductor Physics (P265)

Vilnius 2013

This work has been carried out in 2008 – 2013
at the Semiconductor Optics Laboratory
of Center for Physical Sciences and Technology

Scientific supervisor
Dr. Vytautas Karpus (Center for Physical Sciences and Technology,
physical sciences, physics 02P, semiconductor physics P265)

Consultants
Prof. Dr. Habil. Gintautas Jurgis Babonas (Center for Physical Sciences and Technology, physical sciences, physics 02P, semiconductor physics P265)

Prof. Dr. Hans Arwin (Linköping University,
physical sciences, physics 02P, condensed matter P260)

Contents

Introduction

Quasicrystals are in a focus of the wide-range investigations both because of their fascinating atomic arrangement, and of unexpected physical properties they exhibit.

The physical properties of quasicrystals are quite unusual in light of their chemical composition, – they are just metallic compounds. Still, there are essential differences in mechanical, electrical, and thermal properties of quasicrystals as compared to those of common metals.

Most quasicrystals are noteworthy for their high hardness, which is comparable to that of high-carbon steel, the low coefficient of friction, which is comparable to that of diamond, and the low adhesion energy, approaching that of teflon. The mechanical properties of quasicrystals are employed in practice – quasicrystals are used as specific coatings and as hardening precipitates in metallurgy. The best known example is the Sandvic Nanoflex steel, which incorporates AlCuFe quasicrystalline phase. The precipitates of the ZnMgRE quasicrystals are expected to solve the problem of a replacement of aluminium metallurgy by that of magnesium.

The most intriguing physical feature of quasicrystals is their unexpected electrical characteristics. Their electric conductivity is many orders of magnitude lower than that of the usual metals. Contrary to the known conductivity behavior of metals, the conductivity of quasicrystals increases with an increase of temperature, and is lower in structurally perfect samples than in the poor quality ones.

The physical reasons of the strange electrical properties are unknown. This is because the problem of the electronic structure of quasicrystals, despite of its importance, remains to be unsolved. Nobody knows are the electronic states in quasicrystals localized, extended or critical.

Scope of the dissertation

The main goal of the present dissertation was to reveal the electronic structure of ZnMgRE (RE = Y, Ho, Er) quasicrystals (grown in Prof. W. Assmus laboratory, Frankfurt am Main) by the optical spectroscopy techniques.

The performed X-ray diffraction (XRD) study of the quasicrystals aimed at a determination of the reciprocal quasicrystalline lattice vectors, which define the atomic potential field acting on an electron subsystem.

The goal of the experimental optical investigations, carried out by a combined spectroscopic ellipsometry and reflectance spectroscopy technique, was to reveal the ZnMgRE dielectric function and the optical conductivity spectra in a wide spectral range, which would enable us to distinguish the intraband Drude-type and anticipated interband optical transitions.

To interpret the experimental optical spectra, we expanded the ZnMgRE electronic structure model, which was previously suggested by our group for an interpretation of photoemission spectra, and performed theoretical calculations of an optical response of ZnMgRE electronic subsystem within the framework of the adjusted model.

Finally, a detailed analysis of the experimental optical spectra was carried out on a basis of theoretical modelling results, and the parameters of ZnMgRE electron energy spectrum in a vicinity of the Fermi level were determined.

Summarizing, the dissertation comprises the experimental XRD and optical studies of ZnMgRE quasicrystals, a construction of their electron subsystem model, and a theoretical description of their optical response.

Scientific novelty

The experimental optical and XRD studies of ZnMgRE quasicrystals, carried out in the present dissertation, are in a mainstream of the wide-range investigations of a contemporary quasicrystal physics.

A novelty of the present experimental optical investigations is the employed combined spectroscopic ellipsometry and reflection spectroscopy technique, based on a suggested anchor-window method of reflectivity data analysis. The technique allowed us to obtain detailed, wide-spectral range ZnMgRE optical conductivity spectra. The spectra recorded, we suppose, make the ZnMgRE optical response to be the most comprehensively studied as compared to known optical spectra of other quasicrystals.

The new experimental result obtained in our XRD study is an observation of Bragg peaks with the unusually large complementary fci-ZnMgY reciprocal lattice vectors up to $g_{\perp}a = 23.9$. This is to be compared with the literature result of $g_{\perp}a = 17.3$, obtained in the synchrotron-facilities fci-ZnMgY XRD study. The manifestation of the large complementary $\boldsymbol{g}_{\perp}$-vectors indicates an exceptional structural quality of the studied ZnMgRE quasicrystals.

From a point of view of the general quasicrystal physics, the novel and most important result of the dissertation is the revealed ZnMgRE electronic structure model, which describes in details both the experimental optical spectra of the quasicrystals, recorded in the present work, and previously recorded ZnMgRE valence band photoemission spectra.

Among new results to be mentioned, we would like to point out to a disclosed contribution of the low-structure-factor pseudopotentials to ZnMgRE optical response.

Practical significance

The theoretical scheme of description of the ZnMgRE optical response, worked out in the present work, is general and well-justified for quasicrystals, the valence bands of which are determined by the sp-type electron states. We hope that the scheme can successfully synthesize optical spectra of other, not only of ZnMgRE, quasicrystals.

The model of ZnMgRE electronic subsystem, we suppose, can be extended for a description of an anomalous temperature dependence of the static electrical conductivity of quasicrystals.

Scientific statements

- The optical response of ZnMgRE quasicrystals, as of other metallic compounds, is determined by the intraband Drude-type and the interband optical transitions. The interband optical transitions occur across pseudogaps, which open at intersections of the Fermi surface with Bragg planes. The intersections lead to an essential increase of the optical mass in quasicrystals, as compared to the usual crystalline metals, and, consequently, to a reduction of the spectral weight of the Drude peak.
- The electron subsystem in ZnMgRE quasicrystals maintains the nearly free electron gas character. The energy spectrum of electrons in a vicinity of the Fermi level is determined by the Fermi surface intersections with (222100) and (311111) families of Bragg planes.
- The suggested electron spectrum model perfectly fits the experimental wide-range optical spectra of ZnMgRE quasicrystals and allows for a determination of the electron energy spectrum parameters in a vicinity of the Fermi level. The deduced set of the electron-spectrum parameters actually coincides with that previously deduced in an analysis of ZnMgRE photoemission spectra. This proves the self-consistency of the suggested ZnMgRE electron energy spectrum model – it reproduces experimental data of both the optical, and photoemission response.

Structure of the dissertation

Chapter 1 presents literature survey of basics of the quasicrystal (QC) physics – definitions and major features of QC direct and reciprocal lattices. Original material is presented in section § 1.4 only, which describes investigated samples.

Chapter 2 presents results of ZnMgRE X-ray diffraction study.

Chapter 3 describes a model of ZnMgRE electronic structure.

Chapter 4 describes the optical spectroscopy techniques used, presents a suggested anchor-window method of Kramers–Kronig analysis, describes employed optical-surface preparation techniques, and briefly presents results of XPS study of the ZnMgRE surface layers.

Chapter 5 is the main part of the dissertation. It starts with a short overview of optical properties of quasicrystals. Further, it describes the main experimental results obtained in the carried out optical ZnMgRE investigations, presents a scheme of the theoretical calculations of optical conductivity, and, finally, presents a detailed analysis of the experimental ZnMgRE optical spectra.

Dissemination of the results

The main results were presented at the 13th and 14th International Symposiums on Ultrafast Phenomena in Semiconductors (Vilnius, 2007 and 2010), the 10th International Conference on Quasicrystals (Zürich, 2008), the 5th and 6th International Conferences on Spectroscopic Ellipsometry (Albany NY, 2010 and Kyoto, 2013), the 1st Annual Conference of AnalytiX (Beijing, 2012), and the 38th–40th Lithuanian National Conferences on Physics (Vilnius, 2009–2013).

List of publications

Scientific papers

[1]* V. Karpus, G.-J. Babonas, A. Rėza, A. Suchodolskis, S. Tumėnas, W. Assmus, and S. Brühne, Optical response of fci-ZnMgHo quasicrystal, *Acta Phys. Pol. A* **113**(3), 1005–1008 (2008).

[2]* V. Karpus, G.-J. Babonas, A. Rėza, S. Tumėnas, H. Arwin, W. Assmus, and S. Brühne, Optical response of si-ZnMgHo quasicrystal, *Zietschrift für Kristallographie*, **224**(1–2), 39–41 (2009).

[3]* S. Tumėnas, I. Kašalynas, V. Karpus, and H. Arwin, Infrared reflectance Kramers–Kronig analysis by anchor-window technique, *Acta Phys. Pol. A* **119**(2), 140–142 (2011).

[4]* S. Tumėnas, V. Karpus, H. Arwin, and W. Assmus, Optical conductivity of fci-ZnMgRE quasicrystals, *Thin Solid Films* **519**(9), 2951–2954 (2011).

[5]* V. Karpus, S. Tumėnas, A. Suchodolskis, H. Arwin, and W. Assmus, Optical spectroscopy and electronic structure of the face-centered icosahedral quasicrystals Zn-Mg-R (R = Y, Ho, Er), *Phys. Rev. B* (submitted for publication).

International conferences

[6]* V. Karpus, G.-J. Babonas, A. Rėza, A. Suchodolskis, S. Tumėnas, W. Assmus, and S. Brühne, Dielectric function of i-ZnMgHo quasicrystals, *13th Int. Symposium on Ultrafast Phenomena in Semiconductors 13-UFPS (Vilnius, 2007.08.26–29). Abstracts* (Vilnius, 2007), p. 26.

[7]* V. Karpus, G.-J. Babonas, A. Rėza, S. Tumėnas, H. Arwin, W. Assmus, and S. Brühne, Optical response of si-ZnMgHo quasicrystal, *10th Int. Conf. on Quasicrystals ICQ10 (Zürich, 2008.07.06–11). Program and Abstracts* (Zürich, 2008), p. 94.

[8]* S. Tumėnas, V. Karpus, H. Arwin, and W. Assmus, Optical conductivity of fci-ZnMgRE quasicrystals, *5th Int. Conf. on Spectroscopic Ellipsometry ICSE-V (Albany NY, 2010.05.23–28). Oral and Poster Abstracts* (2010).

[9]* S. Tumėnas, I. Kašalynas, V. Karpus, and H. Arwin, Infrared reflectance Kramers–Kronig analysis by anchor-window technique, *14th Int. Symposium on Ultrafast Phenomena in Semiconductors 14-UFPS (Vilnius, 2010.08.23-25)* (2010).

[10]* F. Eriksson, S. Olsson, J. Birch, L. Hultman, V. Karpus, and S. Tumėnas, Investigations of ZnMgY quasicrystals in reciprocal space, *BIT's 1st Annual Conf. and EXPO of AnalytiX-2012 (Beijing, 2012.03.23–25). Program* (Beijing, 2012).

[11]* S. Tumėnas, V. Karpus, R. Kondrotas, and H. Arwin, Spectroscopic ellipsometry study of moncrystalline Zn, *6th Int. Conf. on Spectroscopic Ellipsometry ICSE-VI (Kyoto, 2013.05.26–31). Conference Program and Abstracts*, p. 79.

Local conferences

[12]* S. Tumėnas, V. Karpus, A. Rėza, H. Arwin, Dielektrinė paprastųjų ikosaedrinių cinkas-magnis-holmis kvazikristalų funkcija, *XII-oji jaunųjų mokslininkų konferencija "Mokslas - Lietuvos ateitis. Fizika ir fizinė kompiuterija" (Vilnius, 2009.04.02), Programa.*

[13]* S. Tumėnas, I. Kašalynas, V. Karpus, Inkaro lango metodas Kramerso–Kronigo analizėje, *XIII-oji jaunųjų mokslininkų konferencija "Mokslas - Lietuvos ateitis. Fizika ir fizinė kompiuterija" (Vilnius, 2010), Programa.*

[14]* S. Tumėnas, V. Karpus, I. Kašalynas, D. Seliuta, and L. Žigas, Optical IR response of fci-ZnMgY quasicrystals, *38th Lithuanian National Conference on Physics (Vilnius, 2009.06.08–10). Program and Abstracts*

(Vilnius, 2009), p. 79.

[15]* S. Tumėnas, V. Karpus, and F. Eriksson, X-ray θ-2θ diffraction of ZnMgY quasicrystal, *39th Lithuanian National Conference on Physics (Vilnius, 2011.06.06–08). Program and Abstracts* (Vilnius, 2011), p. 69.

[16]* S. Tumėnas, R. Juškėnas, V. Karpus, F. Eriksson, S. Olsson, J. Birch, L. Hultman, and W. Assmus, Phason strain in fci-ZnMgY quasicrystals, *40th Lithuanian National Conference on Physics (Vilnius, 2013.06.10–12). Program and Abstracts* (Vilnius, 2013), p. 149.

[17]* S. Tumėnas, V. Karpus, R. Kondrotas, and H. Arwin, Ellipsometric measurements of zinc dielectric function tensor, *40th Lithuanian National Conference on Physics (Vilnius, 2013.06.10–12). Program and Abstracts* (Vilnius, 2013), p. 148.

[18]* R. Kondrotas, R. Juškėnas, S. Tumėnas, V. Karpus, and S. Raman, XPS study of ZnMgRE quasicrystal surface layers, *40th Lithuanian National Conference on Physics (Vilnius, 2013.06.10–12). Program and Abstracts* (Vilnius, 2013), p. 98.

Technical reports

[19]* S. Tumėnas, Trijų aplinkų heterostruktūros atspindžio amplitudės, *X Lietuvos jaunųjų mokslininkų konferencijos "Mokslas – Lietuvos ateitis" (Vilnius, 2007.04.06) medžiaga* (Vilnius, 2007), p. 112–116.

Publications on spectroscopic ellipsometry of heterostructures

[20] S. Tumėnas, V. Karpus, K. Bertulis, and H. Arwin, Dielectric function and refractive index of $\mathrm{GaAs}_{1-x}\mathrm{Bi}_x$ ($x = 0.035,\ 0.052,\ 0.075$), *Phys. Status Solidi C* **9**(7), 1633–1635 (2012).

[21] V. Bukauskas, A. Šetkus, I. Šimkienė, S. Tumėnas, I. Kašalynas, A. Rėza, J. Babonas, V. Časaitė, S. Povilonienė, and R. Meškys, Solid surface dependent layering of self-arranged structures with fibril-like assemblies of alpha-synuclein, *Applied Surface Science* **258**, 4383–4390 (2012).

[22] Z. Balevicius, A. Makaraviciute, G.-J. Babonas, S. Tumenas, V. Bukauskas, A. Ramanaviciene, A. Ramanavicius, Study of optical anisotropy in thin molecular layers by total internal reflection ellipsometry, *Sensors and Actuators B* **181**, 119–124 (2013).

[23] S. Tumėnas, V. Karpus, K. Bertulis, and H. Arwin, Refractive index of GaAs$_{1-x}$Bi$_x$ ($x \approx 0.075$), *16th Semiconducting and Insulating Materials Conference SIMC XVI (Stockholm, 2011.06.19-23). Programme and Abstracts* (2011), p. Tu3-11.

[24] Z. Balevicius, A. Makareviciute, I. Baleviciute, S. Tumenas, A. Stirke, A. Ramanaviciene, and A. Ramanavicius, *In situ* study of ligand-receptor interaction by total internal reflection ellipsometry, *6th Int. Conf. on Spectroscopic Ellipsometry ICSE-VI (Kyoto, 2013.05.26–31). Conference Program and Abstracts*, p. 238.

Acknowledgments

I am greatly indebted to my supervisor Vytautas Karpus for educating, encouraging, and challenging me, for many helpful discussions, suggestions, and manifold support. I could not imagine having a better supervisor for my PhD studies.

Very special thanks to my scientific advisers Gintautas-Jurgis Babonas and Hans Arwin, for enlightening discussions, for sharing their experimental expertise. They taught, guided, and raised me as a spectroscopist.

I am very grateful to my associates from laboratories of Semiconductor Optics and Terahertz Photonics: Alfonsas (Liudvikas) Rėza, Algirdas Kindurys, Julius Kavaliauskas, Bronislovas Čechavičius, Artūras Suchodolskis, Ramūnas Nedzinskas, Irmantas Kašalynas. They created a warm working atmosphere for me.

The investigations I did were carried out in collaboration with several research groups. I was happy to meet Remigijus Juškėnas and Rokas Kondrotas at Institute of Chemistry, Viktoras Vaičikauskas and Zigmas Balevičius at Institute of Physics.

I am grateful for a sincere hospitality shown to me at the Laboratory of Applied Optics and Thin Film Physics Department of Linköping University, where I met Kenneth Järrendahl, Roger Magnusson, Fredrik Eriksson, Simon Olsson, Lars Hultman. The dissertation I wrote undoubtedly gained from the meeting.

The cooperation would not be possible without the grants I received. I am grateful to the Swedish Institute and the Lithuanian Research Council.

Finally, I would like to thank my parents and my wife Kristina for their encouragement and love during the time I worked at this dissertation.

Chapter 1

Quasicrystals

Quasicrystals (QCs) is a new solid-state phase which was discovered in a rapidly solidified $Al_{86}Mn_{14}$ compound [25]. An actual discovery of Shechtman, Blech, Gratias, and Cahn was an observation of unusual diffraction pattern (see Fig. 1.1) with sharp diffraction peaks and a rotational symmetry, incompatible with the periodic crystalline order.

This new finding, which was awarded the Nobel Prize in 2011, broke the fundamental concept of crystallography and forced a reconsideration of the traditional definition of a crystal. The usual crystals are built by a periodic repetition of a single building block, the elementary cell, and exhibit a long range translational and orientational symmetry. The orientational symmetry of crystalline solids, according to conventional laws of crystallography, can maintain only the 2-, 3-, 4-, and 6-fold rotation axes, as is evidently manifested in morphology of minerals and in diffraction patterns of crystals.

The diffraction pattern of AlMn quasicrystalline phase corresponds, however, to the point symmetry group of icosahedron which has the 5-fold axes. A local icosahedral atomic arrangement is the most densely packed and previously has been observed in short-range ordered materials only, such as liquids and amorphous solids. Since the icosahedral symmetry contradicts to the translational periodicity, it was thought that the icosahedral long-range ordered atomic arrangement is impossible. However, soon after the Shechtman's discovery, it was proved that the long-range ordered phases with orientational n-fold, $n = 5$ or $n > 6$, symmetry are feasible [26, 27, 28]. Atoms of quasicrystals arrange themselves into perfect long-range ordered, but aperiodic structures which maintain orientational symmetry, forbidden in the usual crystalline phases.

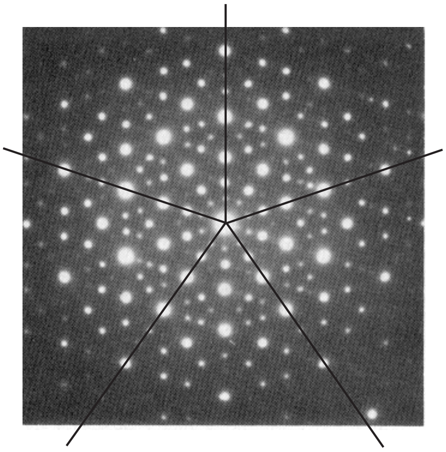

Figure 1.1: The electron diffraction pattern of AlMn quasicrystal (Shechtman et al. 1984 [25]).

1.1 Family of quasicrystals

Since the original discovery of AlMn quasicrystal in 1984, many other quasicrystalline phases have been synthesized. Moreover, natural QC minerals have been found recently [29]. Absolutely, the quasicrystals are no longer a unique form of solids. The quasicrystalline atomic arrangement exists universally in many metallic compounds.

The first quasicrystals reported were metastable, therefore, another breakthrough in a history of quasicrystals, along with the Shechtman discovery, was a discovery of the stable quasicrystalline phases AlLiCu [30], AlCuFe [31], and AlPdMn [32] in 1986–1990. Most of quasicrystals are ternary metallic compounds on aluminum basis, containing approximately 60–70 percents of Al. However, aluminum is not an obligatory component for a formation of a quasicrystalline phase – there are QCs without it. The most famous example is a family of ZnMgRE quasicrystals. The ZnMgRE group (where RE stands for Y or the rare earth element, Dy, Ho, Er, Tb, . . .) of thermodynamically stable quasicrystals was discovered in 1993 [33, 34].

The stable quasicrystalline phases are grown by the usual, "slow", crystal-growth techniques. The usual growth allows for a synthesis of single-grain quasicrystals with linear dimensions up to centimeters, large enough for any detailed physical investigation. The perfect long-range ordered atomic structure of single-grain quasicrystals is confirmed by their morphology, by their TEM (transmission electron microscopy) micrographs, and by sharp, experimental resolution limited, diffraction peaks (see Fig. 1.2).

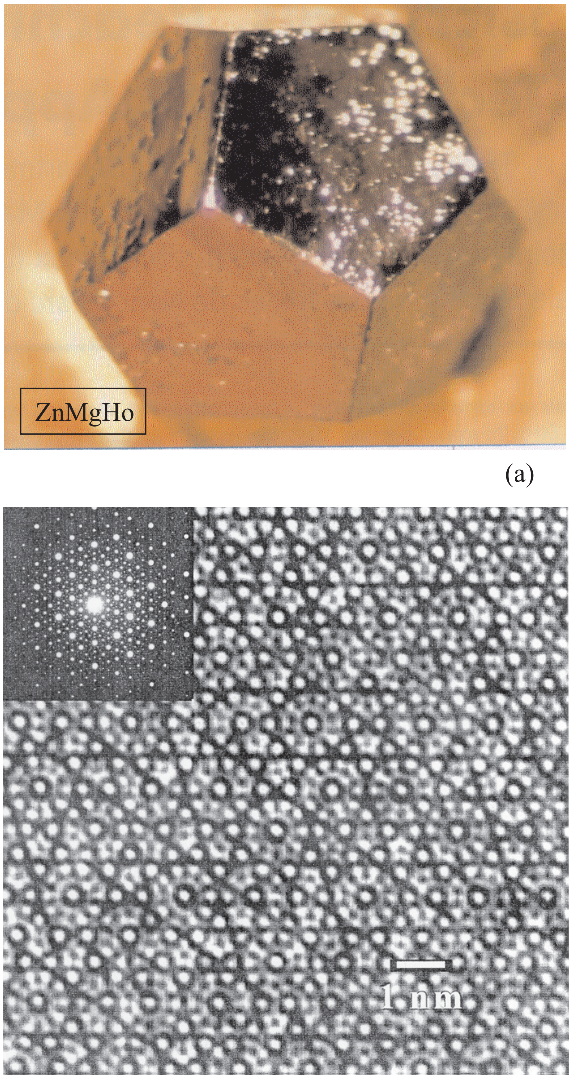

(a)

(b)

Figure 1.2: (a) The single-grain ZnMgHo quasicrystal, $L \approx 0.5$ cm, and (b) the high resolution TEM micrograph of ZnMgDy quasicrystal and its diffraction pattern (Fisher et al. 1998 [35])

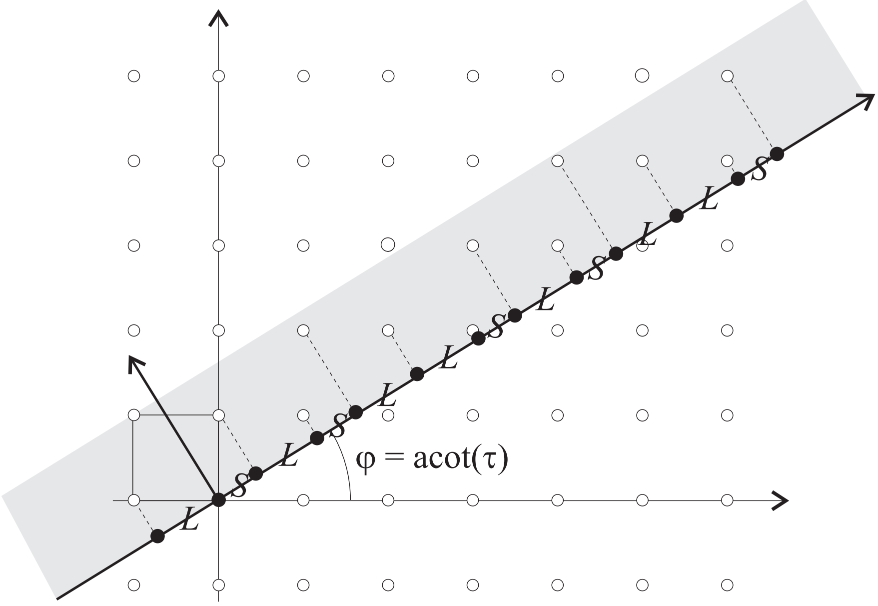

Figure 1.3: 1D quasicrystalline chain as a projection of the 2D hyperlattice.

Apart from the real, atomic, quasicrystals, artificial ones – photonic quasicrystals – are widely investigated (see e. g. [36]) because of their anticipated applications in contemporary photonics engineering. Moreover, recently a new class of quasicrystalline structures, the so-called soft quasicrystals – various composite and polymeric quasicrystalline structures – was revealed and presently is widely investigated [37].

1.2 Quasicrystalline lattice

The quasicrystalline atomic order can be maintained along a single spatial direction (one-dimensional QCs), along two directions (two-dimensional QCs), and along all three spatial directions (three-dimensional QCs).

1.2.1 1D quasicrystals. Fibonacci chain

In the one-dimensional (1D) quasicrystals (e. g. AlNiSi [38]), atomic arrangement is quasicrystalline along a single spatial direction and maintains the usual crystalline periodic order in a perpendicular plane.

The one-dimensional quasicrystalline chain (depicted in Fig. 1.3 by full dots) is comprised of two elementary cells, the short S and long L segments. Though the chain is aperiodic, it maintains a perfect long-range order and its nodes/sites are given by the formula

$$X_n = na_s + \frac{a_s}{\tau}\,\mathrm{Int}\left[\frac{n}{\tau}\right], \tag{1.1}$$

where n is an integer number, which enumerates the nodes, a_s is the length of the S-segment, τ is an irrational number, and $\mathrm{Int}[u]$ denotes an integer part of argument u.

In a general case, τ is any irrational number. However, for a construction of two- and three-dimensional quasicrystalline lattices, τ should acquire specific irrational values. The most important value of τ (which ensures the 5-fold orientational symmetry in 2D and 3D quasicrystals) corresponds to the golden mean,

$$\tau = \frac{1}{2}\left(1+\sqrt{5}\right) = 1.618034\ldots \tag{1.2}$$

When the golden mean value is used in formula (1.1), it generates the 1D quasicrystalline lattice widely known as the Fibonacci chain.

There is a simple geometrical interpretation of the QC chain generation formula (1.1). One starts with the usual crystalline two-dimensional quadratic hyperlattice[1] (open dots in Fig. 1.3) and projects its nodes onto a straight line, drawn at the inclination angle equal to the $\mathrm{acot}(\tau)$. Only the nodes which lie within the so-called projection window are projected. The projection window corresponds to a strip, indicated by a shaded area in Fig. 1.3, the width of which is determined by the primitive cell of the 2D hyperlattice. The projected points, indicated in Fig. 1.3 by full dots, correspond to nodes of the quasicrystalline chain (1.1).

1.2.2 2D quasicrystals. The Penrose tiling

The atomic arrangement of the two-dimensional (2D) QCs is quasicrystalline in a plane and periodic, crystalline, along the plane normal. There are the octagonal (8-fold orientational symmetry), decagonal (10-fold symmetry), and dodecagonal (12-fold symmetry) 2D quasicrystals. The most famous example is the decagonal AlNiCo (see, e. g., [39]).

There are several algorithms for a construction of the 2D quasicrystalline lattice. It can be formed, e. g., as a superposition of a series of interatomic planes, the distances between which follow the 1D QC chain rule (1.1).

---

[1] Here the two-dimensional lattice is called the hyperlattice, because its dimension (2D) exceeds a dimension of the considered physical quasicrystalline lattice (1D).

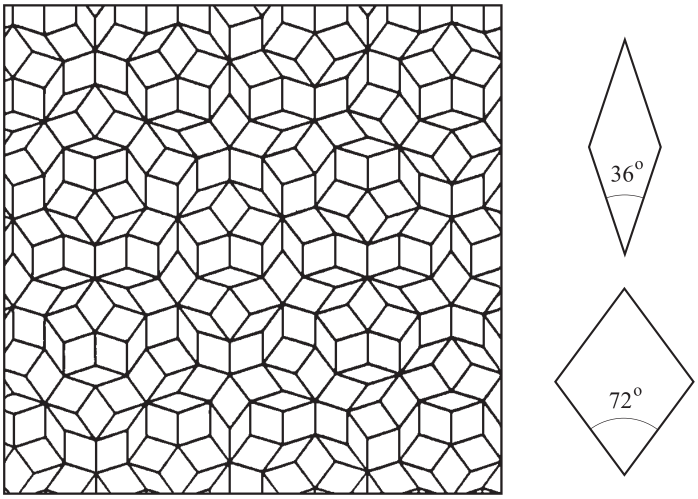

Figure 1.4: The Penrose tiling and its elementary cells. (Adapted from Janot 1994 [40].)

The most known algorithm of the 2D QC construction was suggested by Penrose in 1974 [41], ten years before the experimental discovery of quasicrystals. The two-dimensional dodecagonal Penrose tiling can be built of two different elementary cells – the prolate and oblate rhombi of 36° and 72° angles, correspondingly. As it is obviously seen from Fig. 1.4, the Penrose tiling maintains both a perfect long-range order, and the 10-fold orientational symmetry.

1.2.3 3D quasicrystals

All known three-dimensional (3D) quasicrystals are icosahedral, the orientational symmetry of their atomic arrangement corresponds to the icosahedral point group. The icosahedron (Fig. 1.5) is a regular polyhedron with twenty equilateral triangular faces. It has six fivefold, C_5, rotation symmetry axes, ten C_3 axes, and fifteen C_2 ones.

3D Penrose tiling

The Penrose algorithm can be generalized for a construction of the three-dimensional quasicrystalline lattice. In the 3D case, the two elementary cells are the prolate and oblate rhombohedrons, PR and OR, depicted in Fig. 1.6. The side length a of both rhombohedrons is the same and is called the quasilattice constant. Orientation of the PR and OR rhombohedron

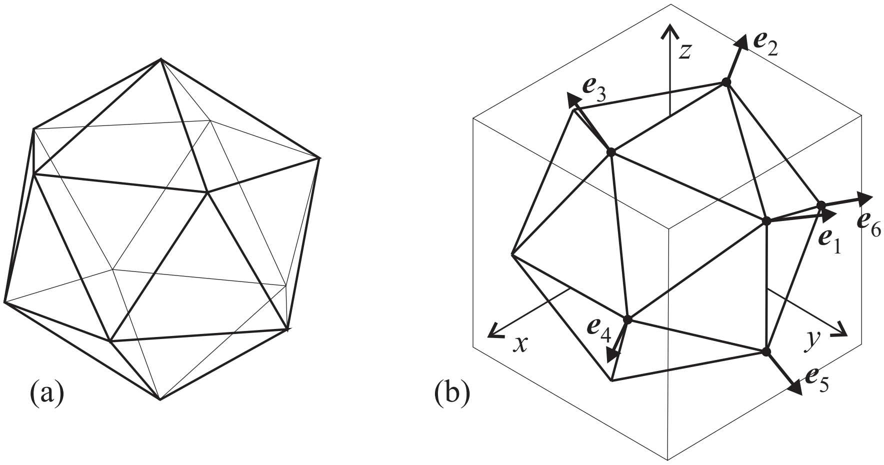

Figure 1.5: Icosahedron (a) and its unit vectors (b).

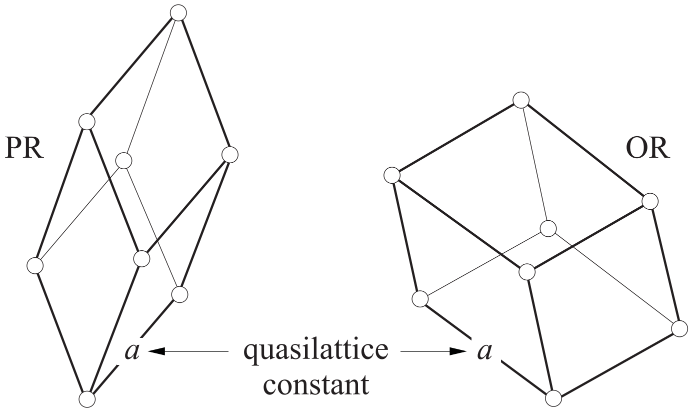

Figure 1.6: The elementary cells of the 3D quasicrystalline lattice.

edges fits the unit vectors of icosahedron $\boldsymbol{e}_i$ (Fig. 1.5(b)), which are directed along C_5 axes and are given by the formula

$$\begin{pmatrix} \boldsymbol{e}_1 \\ \boldsymbol{e}_2 \\ \boldsymbol{e}_3 \\ \boldsymbol{e}_4 \\ \boldsymbol{e}_5 \\ \boldsymbol{e}_6 \end{pmatrix} = \frac{1}{\sqrt{1+\tau^2}} \begin{pmatrix} 1 & \tau & 0 \\ -1 & \tau & 0 \\ 0 & 1 & \tau \\ \tau & 0 & 1 \\ \tau & 0 & -1 \\ 0 & 1 & -\tau \end{pmatrix} \begin{pmatrix} \hat{\boldsymbol{x}} \\ \hat{\boldsymbol{y}} \\ \hat{\boldsymbol{z}} \end{pmatrix}. \qquad (1.3)$$

Here $\hat{\boldsymbol{x}}$, $\hat{\boldsymbol{y}}$, $\hat{\boldsymbol{z}}$ are the unit Cartesian vectors and τ is the golden mean.

Projection from hyperspace

Another widely used technique, which allows to generate the 3D quasicrystalline lattice, is a projection from the hyperspace [42, 43, 44, 45]. If the 1D quasicrystalline lattice can be simulated as a projection of the two-dimensional quadratic hyperlattice onto a line, i. e. the one-dimensional physical space, the three-dimensional quasicrystalline lattice can be generated as a projection of the six-dimensional cubic hyperlattice onto the 3D physical space.

si-, fci-, and bci-QCs

The icosahedral 3D quasicrystalline lattices can be obtained by a projection of the 6D primitive, face-centred, and body-centred hypercubic lattices. Accordingly, there are simple icosahedral (si or P) and face-centred icosahedral (fci or F) quasicrystals. Though the body-centred icosahedral (bci or I) quasicrystals are feasible, so far there no indisputable reports on an observation of the bci-QC phases.

The most famous examples of the si- and fci-quasicrystals are si-AlMn, fci-AlCuFe, and fci-AlPdMn. Some of the quasicrystalline compounds, depending on their atomic composition, can be both of si-, and fci-type. For example, $Zn_{74}Mg_{15}Ho_{11}$ is the simple icosahedral quasicrystal, while $Zn_{65}Mg_{25}Ho_{10}$ is the fci-one.

Atomic decoration of QC lattice

Though the principles of quasicrystalline atomic arrangement, i. e. a structure of the quasicrystalline lattice, is rather well-known, an atomic decoration of the QC lattices so far is not unambiguously determined. There are several hypothetical models of the decoration [46, 47], which are widely used in literature.

1.3 Reciprocal QC lattice

The reciprocal lattice is an important physical concept, because it determines the main laws of interaction of waves or particles with the media under consideration. The most important examples are the diffraction of X-rays and an influence of crystalline (quasicrystalline) field on the valence electron subsystem.

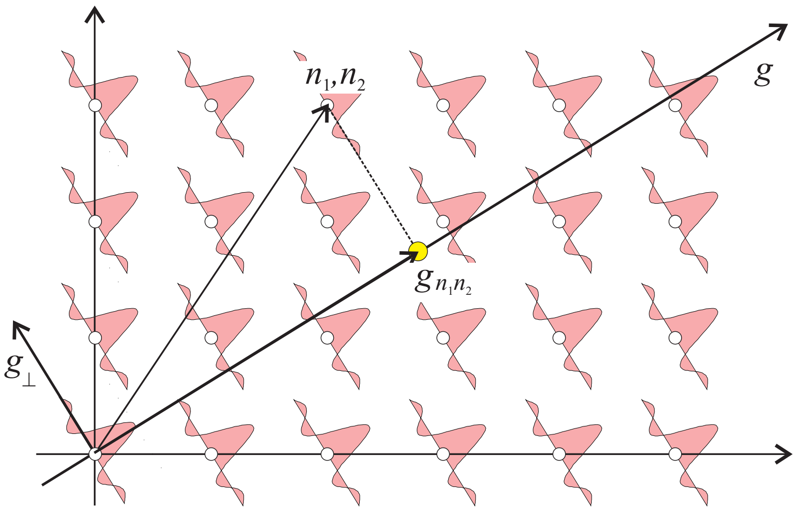

Figure 1.7: One-dimensional reciprocal QC lattice as a projection from the two-dimensional hyperspace.

The reciprocal lattice of any physical system is defined as the Fourier transform of its direct lattice. This definition is used for a determination of the quasicrystalline reciprocal lattice.

The reciprocal lattice of the one-dimensional quasicrystalline chain (1.1) can be easily calculated analytically. The reciprocal lattice vectors are given by the formula (see, e.g., [40])

$$g_{n_1 n_2} = \frac{2\pi}{a_s} \frac{1}{1+\tau^2} \left(\tau n_1 + n_2\right). \tag{1.4}$$

Both the direct, and the reciprocal lattices can be treated as projections from the 2D hyperspace. Indeed, the reciprocal lattice nodes (1.4) correspond exactly to projections of the 2D quadratic lattice onto the τ-slope line, as is illustrated in Fig. 1.7. This is why two indices, n_1 and n_2, are needed to span the one-dimensional reciprocal quasicrystalline lattice.

Although the reciprocal quasicrystalline lattice (1.4) is discrete, it fills the reciprocal space densely. Indeed, when τ is an irrational number, one can always find two integer numbers n_1 and n_2 such, that formula (1.4) will be satisfied for an arbitrarily chosen g value. However it should be kept in mind that the Fourier transform of 1D quasicrystalline chain (1.1) yields the reciprocal lattice, each node of which is modulated by its Fourier amplitude alias the structure factor S_g,

$$S_g = \frac{\sin(g_\perp \overline{a})}{g_\perp \overline{a}} \, \mathrm{e}^{-\mathrm{i}\gamma}, \tag{1.5}$$

where $g_\perp$ is the complementary, perpendicular reciprocal lattice vector (see Fig. 1.7), $\overline{a} = (a_S + a_L)/2$ is an average of the short and long segments of the Fibonacci chain, and γ is the phase factor. Thus, though the quasicrystalline reciprocal lattice is dense, only the nodes with the large structure factors, $S_g \sim 1$, are of importance. As a result, the experimental diffraction patterns of quasicrystals are not continuous, but discrete as of the usual crystals.

The reciprocal lattice vectors of the three-dimensional quasicrystals are given by the formula [48]

$$\boldsymbol{g} = \frac{\pi}{a} \sum_{i=1}^{6} n_i \boldsymbol{e}_i, \tag{1.6}$$

where a is the quasilattice constant, n_i are integer numbers, and $\boldsymbol{e}_i$ are the unit vectors of icosahedron (see (1.3) and Fig. 1.5). Note that six n_i indices are required for a determination of the reciprocal lattice vectors in the 3D case.

The structure factor of the reciprocal lattice nodes is determined by the complementary, perpendicular reciprocal lattice vector

$$\boldsymbol{g}_\perp = \frac{\pi}{a} \sum_{i=1}^{6} n_i \boldsymbol{e}_i^\perp, \tag{1.7}$$

where n_i are the same indices, which determine $\boldsymbol{g}$-vectors (1.6), and $\boldsymbol{e}_i^\perp$ are the unit vectors, which are related with the $\boldsymbol{e}_i$-vectors as

$$\boldsymbol{e}_1^\perp = -\boldsymbol{e}_1, \quad \boldsymbol{e}_2^\perp = \boldsymbol{e}_2, \quad \boldsymbol{e}_3^\perp = \boldsymbol{e}_4, \quad \boldsymbol{e}_4^\perp = \boldsymbol{e}_6, \quad \boldsymbol{e}_5^\perp = \boldsymbol{e}_3, \quad \boldsymbol{e}_6^\perp = \boldsymbol{e}_5. \tag{1.8}$$

The $g_\perp$-dependence of the structure-factor $S_{\boldsymbol{g}}$ can be calculated numerically [48]. The calculations show (see Fig. 1.8) that the dependence is close to the sinc-function

$$S_{\boldsymbol{g}} = \frac{\sin(g_\perp a)}{(g_\perp a)}. \tag{1.9}$$

1.4 ZnMgRE quasicrystals

The first evidence of an icosahedral quasicrystalline ZnMgY phase was observed at grain boundaries in commercial Mg alloys by Luo et al. in 1993 [33]. In a follow up work, a group of stable icosahedral quasicrystals ZnMgRE (RE = Y, Gd, Tb, Dy, Ho, Er) was synthesized in 1994 [34]. The first ZnMgRE quasicrystals were synthesized by melting initial alloys in an electric furnace and casting with the semicontinuous water-cooling method.

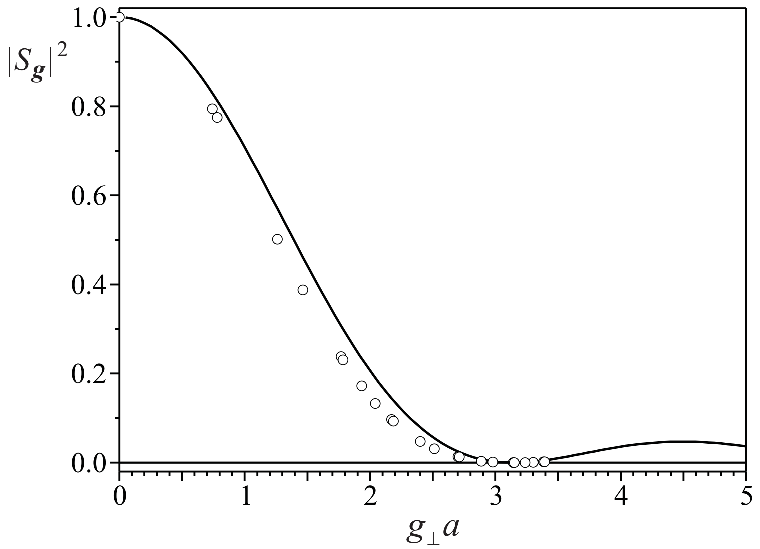

Figure 1.8: The structure factor of the 3D reciprocal quasicrystalline lattice. Dots correspond to Elser results [48]. Curve corresponds to the sinc-function given by eq. (1.9).

The obtained QCs were polycrystalline with small grains of about hundred micrometers in diameter. In 1997, Assmus group [49] optimized ZnMgRE synthesis conditions, which allowed for a growth of the large, structurally perfect single-grain ZnMgRE quasicrystals with linear dimensions up to 1 cm [50, 35] (see Fig. 1.9 and Fig. 1.2(a)).

1.4.1 Samples and material parameters

In the present work we investigated face-centred icosahedral (fci) ZnMgY, ZnMgHo, ZnMgEr and simple icosahedral (si) ZnMgHo quasicrystals, which have been grown in Prof. W. Assmus laboratory at J. W. Goethe University (Frankfurt am Main). The single-grain ZnMgRE quasicrystals were grown by the liquid-encapsulated top-seeded solution-growth technique (LE-TSSG) [50]. The QC samples with C_5, C_3, and C_2 symmetry axes perpendicular to their surfaces were separated from ingots by a spark cutting and oriented by X-ray Laue method. The sample surface areas were of about $0.1-0.5$ cm^2, while their thickness was of about 3 mm.

The structural perfection of the quasicrystals was confirmed by sharp, experimental resolution limited, Bragg peaks of their diffraction patterns (Chapter 2). The stoichiometry of the quasicrystals was determined by the wavelength dispersive X-ray analysis, which showed their atomic com-

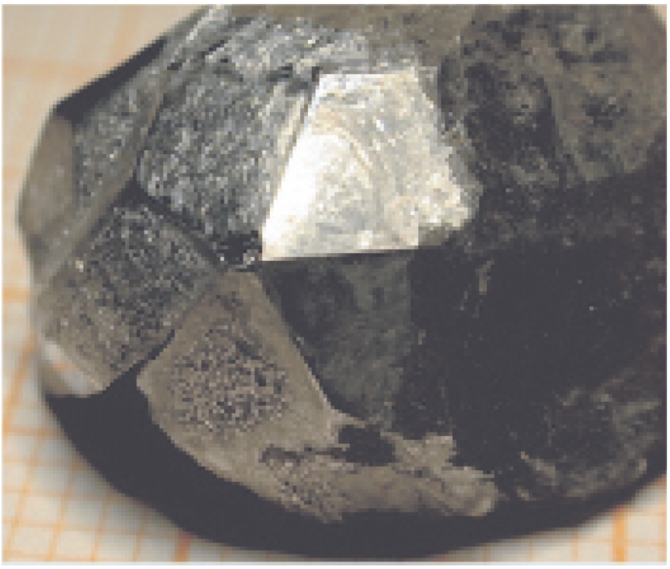

Figure 1.9: The single-grain simple-icosahedral ZnMgHo quasicrystal grown by Assmus group [51].

Table 1.1: Material parameters of ZnMgRE quasicrystals and crystalline Zn: the mass density ρ, the atomic concentration n_a, the average valence $\overline{Z}$, the valence electron concentration n, and the Fermi wave vector $k_{\mathrm{F}} = (3\pi^2 n)^{1/3}$.

	ρ (g/cm^3)	n_a (10^{22} cm^{-3})	$\overline{Z}$	n (10^{23} cm^{-3})	k_F (10^8 cm^{-1})
fci-$Zn_{62}Mg_{29}Y_9$	5.18	5.61	2.09	1.17	1.51
fci-$Zn_{65}Mg_{25}Ho_{10}$	5.82	5.39	2.10	1.13	1.50
si-$Zn_{74}Mg_{15}Ho_{11}$	6.46	5.54	2.11	1.17	1.51
fci-$Zn_{65}Mg_{24}Er_{11}$	5.87	5.30	2.11	1.12	1.49
Zn	7.14	6.58	2	1.32	1.57

position to be fci-$Zn_{62}Mg_{29}Y_9$, fci-$Zn_{65}Mg_{25}Ho_{10}$, si-$Zn_{74}Mg_{15}Ho_{11}$, and fci-$Zn_{65}Mg_{24}Er_{11}$. The mass density of ZnMgRE was measured by Micrometrics AccuPyc 1330. The recorded ρ values and the known atomic composition of QCs allow for a determination of their atomic concentration n_a, which is presented in Table 1.1.

The valence electron concentration in the quasicrystals can be calculated as $n = \overline{Z} n_a$, where $\overline{Z}$ is the average valence of atoms. Assuming that the rare earth elements contribute three electrons to the valence electron subsystem, one obtains the average valence in the quasicrystals to be $\overline{Z} = 2.09 - 2.11$. This yields the electron concentrations presented in Table 1.1.

At a given electron concentration one can evaluate the Fermi wave vector as $k_{\mathrm{F}} = (3\pi^2 n)^{1/3}$ (see Table 1.1). It should be noted, that the calculated value of the Fermi wave vector corresponds to the free electron gas and can change its value when an influence of the quasicrystalline potential on the electron subsystem is taken into account.

Since in ZnMgRE quasicrystals the zinc atoms constitute a major part of their atomic composition, 60–70 %, apart from the quasicrystals, the monocrystalline Zn samples were investigated in the present work as a convenient physical reference system. The single-grain Zn ingots were grown by Czochralski technique in Prof. R. Juškėnas laboratory at Institute of Chemistry (Vilnius) and in Surface Preparation Laboratory (Netherlands). The samples with the (001) surface were cleaved from ingots in liquid nitrogen bath, the (110) samples were separated by a diamond-saw cutting. The Zn sample surface areas were of about 1 cm^2.

Chapter 2

Atomic QC structure. XRD study

The main tool for experimental investigations of the atomic structure of quasicrystals, as of other solids, is the X-ray diffraction (XRD).

Since the diffraction reflexes are determined by the reciprocal lattice vectors $\boldsymbol{g}$ of the system under investigation,

$$\boldsymbol{k}' = \boldsymbol{k} + \boldsymbol{g}, \tag{2.1}$$

where $\boldsymbol{k}'$ and $\boldsymbol{k}$ are the wave vectors of the diffracted and incident waves, the experimental diffraction patterns actually scan the reciprocal lattice.

Although the reciprocal quasicrystalline lattice is discrete, it fills the reciprocal space densely (§ 1.3). Nevertheless, due to small structure factors of most reciprocal lattice nodes, the diffraction patterns of quasicrystals are not continuous, but discrete and usually are comprised of a comparatively small number of Bragg peaks (§ 2.1).

For detailed studies of QC atomic structure, one needs to collect a large number of diffraction peaks, what is achieved by the high-resolution powder-diffraction measurements, usually carried out with the synchrotron-radiation X-ray sources. An analysis of the ZnMgRE XRD data by the pair distribution function technique, carried out by Assmus group [52, 53, 54, 55], allowed for a reconstruction of the ZnMgRE local atomic structure in the coordination spheres with radii of about 30 Å, which comprise four–five thousands of atoms.

In the present study we succeeded to record unusually rich ZnMgRE diffraction patterns by ϑ-2ϑ XRD technique making use of the state-of-the-art diffractometers equipped, however, with the usual copper-anode X-

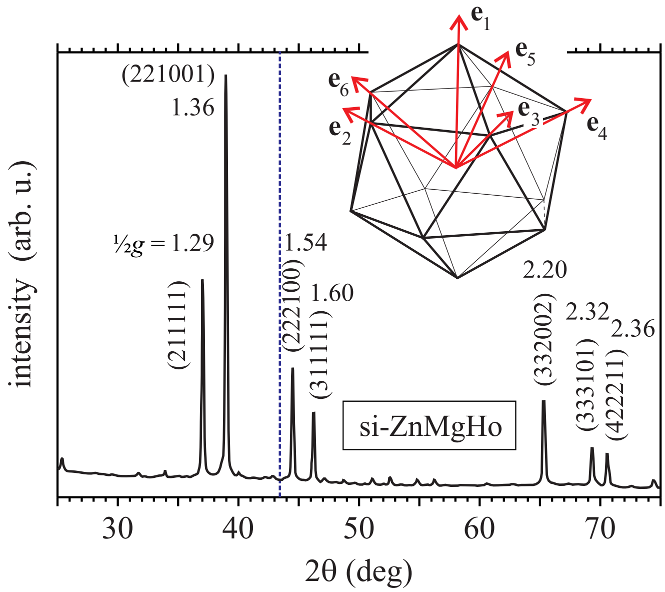

Figure 2.1: Debye–Scherrer diffractogram of the simple icosahedral ZnMgHo quasicrystal, recorded by Assmus group (private communication).

ray sources (§ 2.2). The similar results previously, to our knowledge, were obtained in the synchrotron-facilities XRD studies only. Additionally to the ϑ-2ϑ linear scans, recorded in the present study along the high-symmetry directions of ZnMgRE quasicrystals, the ultimate-large-scale planar cut of the reciprocal fci-ZnMgY lattice was disclosed (§ 2.4).

A detailed analysis of the recorded ϑ-2ϑ diffractograms revealed a phason strain in one of the investigated fci-ZnMgY samples (§ 2.3).

2.1 Debye–Scherrer diffractograms

Simple icosahedral QCs

The powder diffraction pattern of the simple icosahedral (si) ZnMgHo quasicrystal, recorded by Assmus group with the Siemens D500 diffractometer (Cu $K_{\alpha 1}$, $\lambda = 1.5406$ Å), is presented in Fig. 2.1.

The six-dimensional indices of the diffraction peaks correspond to indices of the reciprocal lattice vectors (1.6). The successful indexing allows for a determination of the si-ZnMgHo quasilattice constant to be $a = 5.144$ Å.

The Laue diffraction law (2.1), taking into account that a diffraction is the elastic scattering ($k' = k = 2\pi/\lambda$), can be rewritten in the form

$$g = \frac{4\pi}{\lambda} \sin\vartheta, \tag{2.2}$$

where ϑ is the Bragg angle, a half of the angle between the diffracted and incident beams (see Fig. 2.4). The formula (2.2) allows for a direct determination of moduli of the reciprocal lattice vectors. In Fig. 2.1, the half moduli, $\frac{1}{2}g$, are indicated (in Å^{-1} units) by numbers at diffraction peaks.

The reciprocal lattice determines both diffraction patterns, and the potential field acting on the electron subsystem (see Chapter 3 for details)

$$V(\boldsymbol{r}) = \sum_{\boldsymbol{g}} V_{\boldsymbol{g}} \exp(\mathrm{i}\boldsymbol{g}\boldsymbol{r}). \tag{2.3}$$

The $\boldsymbol{g}$-vectors, which play a decisive role in the quasicrystalline potential $V(\boldsymbol{r})$, correspond to the Bragg planes, which are in the proximity of the Fermi surface, i. e. which satisfy the condition $\frac{1}{2}g \approx k_{\mathrm{F}}$. The dashed line in Fig. 2.1 indicates the si-ZnMgHo Fermi wave vector value (Table 1.1) and allows to predict that a decisive role for the si-ZnMgHo electron subsystem should be played by the (222100) and (311111) Bragg planes.

Face-centred icosahedral QCs

The powder-diffraction patterns of the face-centred icosahedral (fci) ZnMgY, ZnMgHo, and ZnMgRE quasicrystals are presented in Figs. 2.2 – 2.3.

The diffraction peaks of the face-centred icosahedral phase should satisfy the extinction rule, which is a cognate of an extinction rule of the face-centred cubic crystals, –

$$\text{all six indices } n_i \text{ should be either even, or odd.} \tag{2.4}$$

As seen from Fig. 2.2(a), the rule is strictly followed.

The all-even diffraction peaks in fci-QCs usually are stronger than the all-odd ones, and instead of the standard indexing scheme, which is also called as ‘the extended scheme’, the so-called conventional scheme of indexing is commonly used. Within the framework of the conventional scheme, the fci lattice is treated as a superstructure on a primitive icosahedral lattice. Then, the quasilattice constant is taken to be a half of the fci one, and indices of $\boldsymbol{g}$-vectors, according to (1.6), are divided by two. Thus the all-even fci indices reduce to sets of six integers, while the all-odd indices reduce to sets of all six half-integers. The indexing in the conventional scheme

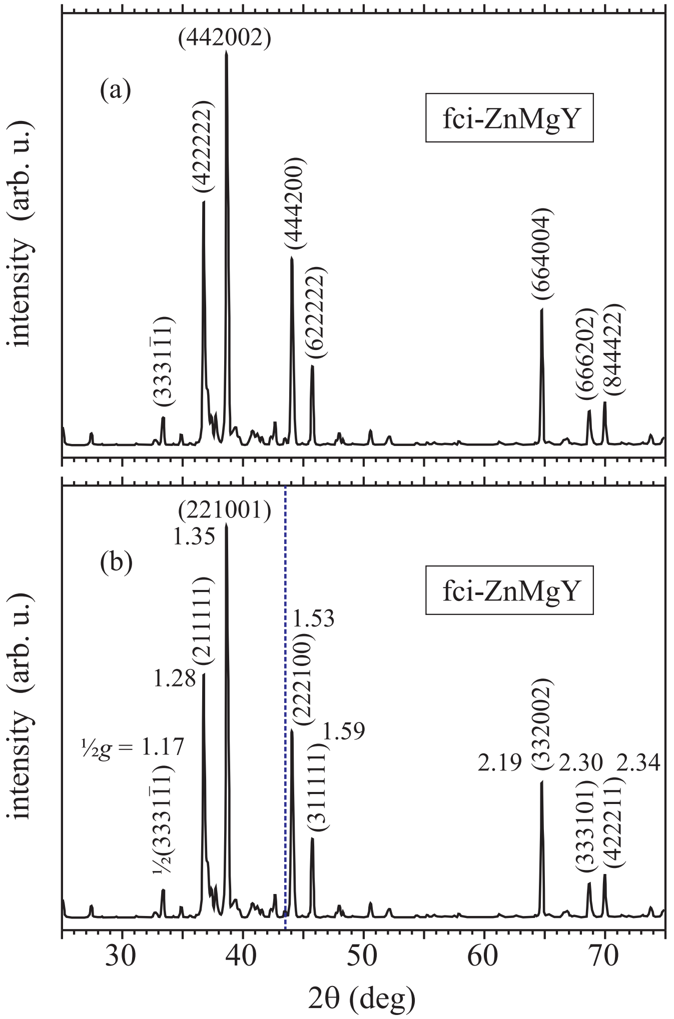

Figure 2.2: Debye–Scherrer diffractogram of the fci-ZnMgY quasicrystal, recorded by Assmus group (private communication). Diffraction peaks are indexed in the extended (a) and the conventional scheme (b).

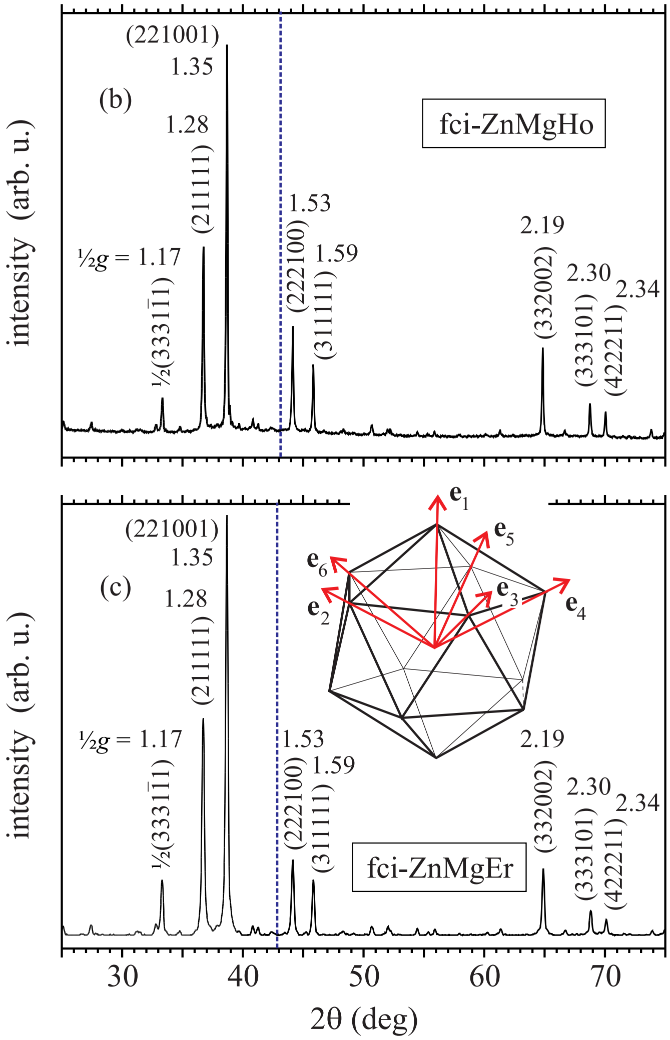

Figure 2.3: Debye–Scherrer diffractograms, recorded by Assmus group (private communication), of (a) fci-ZnMgHo and (b) fci-ZnMgEr quasicrystals.

is indicated in Fig. 2.2(b). The fci-ZnMgY quasilattice constant within the conventional scheme is $a = 5.185$ Å.[1] In the present thesis we shall follow the conventional indexing scheme (except § 2.4, where the extended scheme will be needed).

The fci-ZnMgHo and fci-ZnMgEr diffractograms, presented in Fig. 2.3, are similar to the fci-ZnMgY diffractogram, indicating a similar quasilattice constant value, $a \approx 5.18$ Å.

The dashed lines in Fig. 2.2(b) and Fig. 2.3 correspond to values of the Fermi wave vectors in the fci-ZnMgRE quasicrystals (see Table 1.1) and predict that the same (222100) and (311111) Bragg planes are expected to be of importance for the fci-ZnMgRE electronic structure problem, as was the case for si-ZnMgHo.

2.2 Theta-2theta diffraction

Due to low structure factors of most of the quasicrystalline reciprocal lattice nodes, a number of diffraction peaks, observed in the usual powder-diffractograms (Figs. 2.1 – 2.3), is comparatively small and is similar to a number of peaks in diffractograms of conventional crystals. Theoretically, with an increase of the XRD experimental resolution, one expects more and more diffraction peaks to be revealed in QC diffractograms.

We observed the effect in the ϑ-2ϑ XRD diffraction patterns.

2.2.1 ϑ-2ϑ. Experimental

The theta-2theta diffraction measurements were performed on si-ZnMgHo and fci-ZnMgRE (RE=Y, Ho) samples with various symmetry axes, C_5, C_3, and C_2, perpendicular to their surfaces. The measurements were carried out by two state-of-the-art diffractometers, both equipped with the usual copper-anode X-ray sources, – Empyrean Panalytical diffractometer at the Thin Film Physics Department (Linköping University) and SmartLab Rigaku diffractometer at the Department of Characterization of Materials Structure (SPST Institute of Chemistry). The diffraction patterns recorded

---

[1] To differentiate the fci quasilattice constant a, determined in the conventional indexing scheme, from the $a^* = 2 \times a$ constant, used in the extended scheme, the a^* quasilattice constant is called as the superstructure constant.

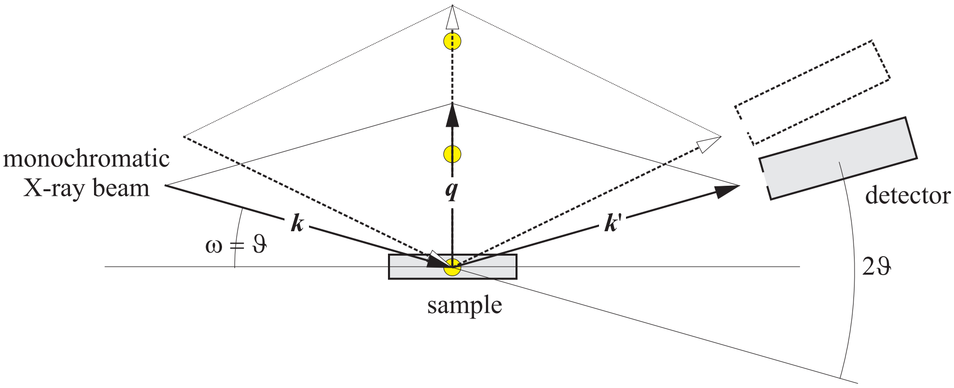

Figure 2.4: Scheme of the ϑ-2ϑ diffraction.

were well reproducible. The XRD ϑ-2ϑ scans, carried out on both diffractometers, repeated a structure of diffractograms in all details.

A scheme of the ϑ-2ϑ diffraction is presented in Fig. 2.4. An X-ray tube and a detector are positioned at the same glancing angles with respect to a sample and are synchronously rotated during measurement in such a way, that the angle between $\boldsymbol{k}'$ and $\boldsymbol{k}$ vectors 2ϑ remains to be twice the glancing angle of the incident beam $\omega = \vartheta$. Under this condition, the diffraction vector $\boldsymbol{q}$, which is defined as a difference between wave vectors of the diffracted and incident beams, $\boldsymbol{q} = \boldsymbol{k}' - \boldsymbol{k}$, maintains its direction, changing only its modulus. When, during the rotation, the $\boldsymbol{q}$ vector hits the reciprocal lattice nodes, indicated by circles in Fig. 2.4, the diffraction condition (2.1) is satisfied, and a detector records the diffraction peak.

Since the diffraction vector $\boldsymbol{q}$ does not change its orientation, the ϑ-2ϑ technique actually scans the reciprocal space along a single, chosen, direction. Thus, only a few peaks can be recorded in the ϑ-2ϑ scans of the usual single-grain crystals. This is illustrated in Fig. 2.5, which presents the ϑ-2ϑ diffractogram recorded along C_6 axis of the single-grain zinc sample.[2]

2.2.2 ZnMgRE ϑ-2ϑ diffractograms

The ϑ-2ϑ diffraction patterns recorded along ZnMgRE C_5, C_3, and C_2 symmetry axes disclose an astonishingly large number of XRD reflexes – up to about ~ 90 along C_5, ~ 50 along C_3, and ~ 30 along the C_2 axis.

---

[2] Theta-2theta, as well as Debye–Scherrer, diffractograms can be presented either as intensity versus theta, or as intensity versus diffraction vector plots, making use of the relation $q = \frac{4\pi}{\lambda}\sin\vartheta$ (see (2.2)).

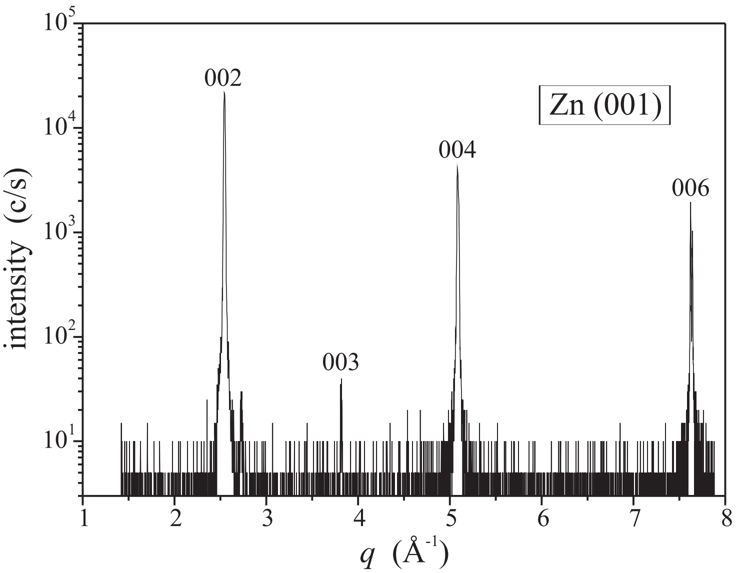

Figure 2.5: Theta-2theta diffractogram along C_6 axis of zinc.

The $\boldsymbol{q} \parallel C_5$, $\boldsymbol{q} \parallel C_3$, and $\boldsymbol{q} \parallel C_2$ scans, corresponding to the 2ϑ range of $10° – 150°$, are presented in Figs. 2.6 – 2.7. All the diffraction peaks recorded, even the smallest ones, can be successfully indexed with the 6D indices of the $\boldsymbol{g}$-vectors (1.6). The diffraction peaks obey the inflation-deflation law of the QC reciprocal lattice [48], which is very helpful in indexing of QC diffraction patterns:

> For a given reciprocal lattice vector $\boldsymbol{g}$ (the sum of indices of which is an even number), there exists another reciprocal lattice vector $\boldsymbol{g}'$, which is parallel to $\boldsymbol{g}$ and has the modulus $g' = \tau g$ (where τ is the golden mean).

The indices of the $\boldsymbol{g}'$-vector are given by the transformation matrix $\boldsymbol{M}$,

$$n'_i = \sum_j^6 M_{ij} n_j, \quad M_{ij} = \frac{1}{2} \begin{pmatrix} 1 & 1 & 1 & 1 & 1 & 1 \\ 1 & 1 & 1 & -1 & -1 & 1 \\ 1 & 1 & 1 & 1 & -1 & -1 \\ 1 & -1 & 1 & 1 & 1 & -1 \\ 1 & -1 & -1 & 1 & 1 & 1 \\ 1 & 1 & -1 & -1 & 1 & 1 \end{pmatrix}. \qquad (2.5)$$

The inflation-deflation rule predicts that, in the diffraction pattern plotted as a function of $\ln q$, the ϑ-2ϑ diffraction peaks should group into the equidistant sequences. This is really the case, as is illustrated in Fig. 2.8 for a several equidistant τ-sequences.

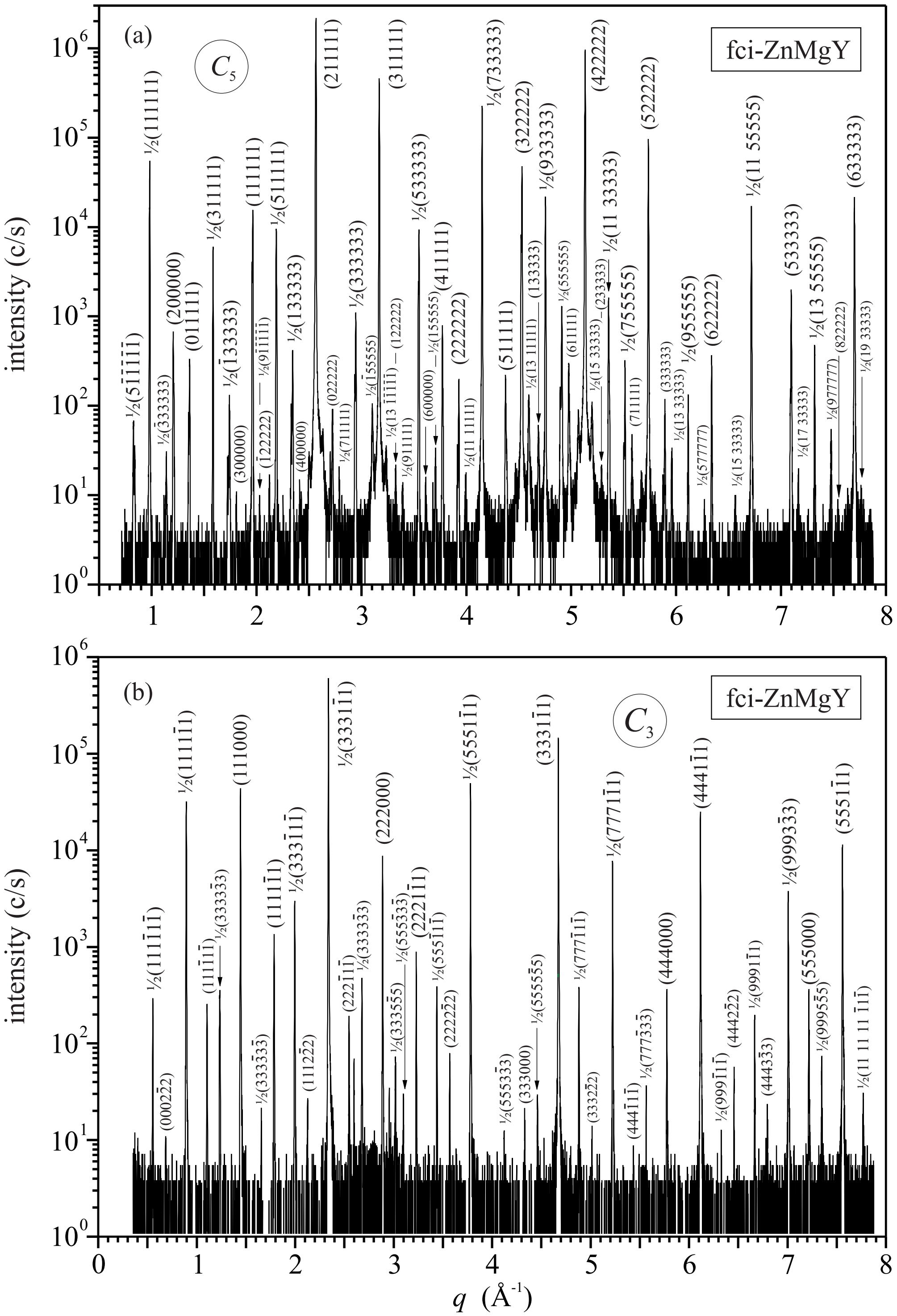

Figure 2.6: Theta-2theta diffractograms recorded along C_5 and C_3 axes of fci-ZnMgY.

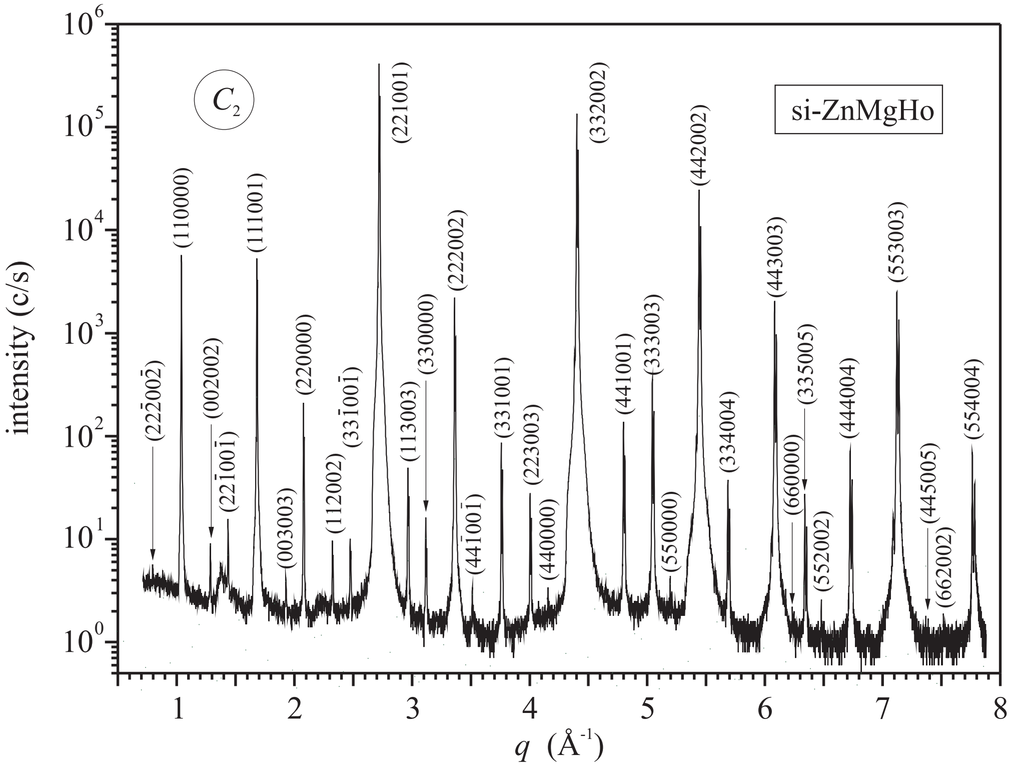

Figure 2.7: Theta-2theta diffractogram recorded along C_2 axis of si-ZnMgHo.

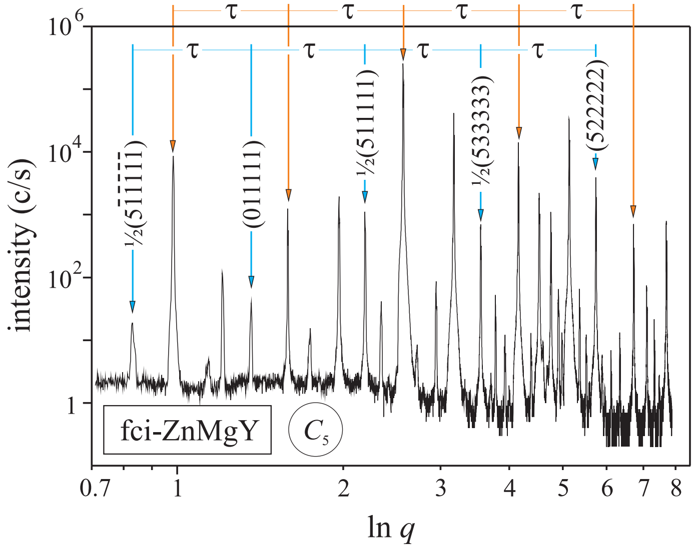

Figure 2.8: Diffraction peaks of quasicrystals group into equidistant sequences, when ϑ-2ϑ diffractogram is plotted as a function of $\ln q$.

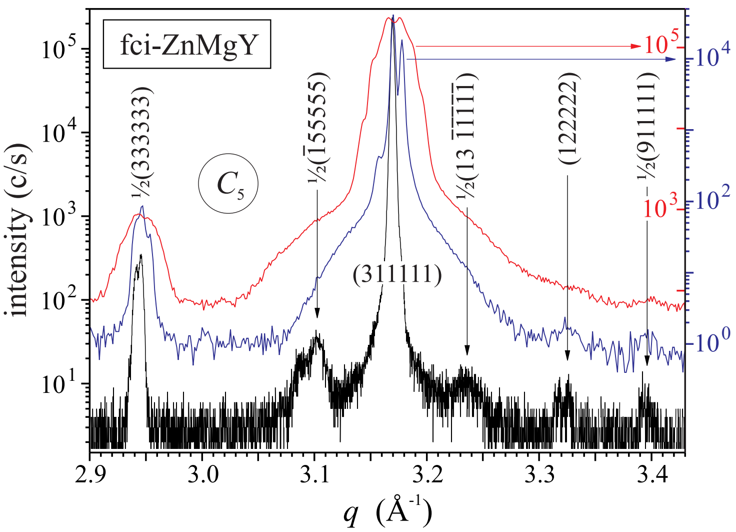

Figure 2.9: The (311111)-vicinity theta-2theta scans, recorded at various XRD instrumental resolutions.

The experimental ZnMgRE diffraction patterns, as seen from Figs. 2.6 – 2.7, exhibit a large dynamical range of the diffraction peak intensities. The reflexes with the intensity ratio below $\sim 10^{-5}$ are recorded, i. e. the ZnMgRE reciprocal lattice nods with the low structure factors, down to $S_{\boldsymbol{g}} \sim 10^{-2} – 10^{-3}$, are traced.

Upon increase of the instrumental resolution, more and more diffraction peaks are being revealed, as is illustrated in Fig. 2.9. The structure factors of the quasicrystalline reciprocal lattice are determined by the complementary reciprocal lattice vector $\boldsymbol{g}_\perp$. The structure factor quickly decreases with an increase of $g_\perp$ when $g_\perp$ exceeds the characteristic value $g_\perp \sim 1/a$ (see eq. (1.9) and Fig. 1.8). As a result, in the usual QC diffraction patterns only the reflexes with $g_\perp a < 6$ are commonly detected. The fci-ZnMgY diffraction peak $\frac{1}{2}(13\,\bar{1}\,\bar{1}\,\bar{1}\,\bar{1}\,\bar{1})$, recorded in the high-resolution ϑ-2ϑ scan (Fig. 2.9), corresponds to the unusually large complementary $\boldsymbol{g}_\perp$-vector, $g_\perp a = 23.9$.

In numerous recorded fci-ZnMgY theta-2theta C_5-scans, actually all possible diffraction peaks with $g_\perp a$ below 20 were detected, with an exception of the (722222) peak, which corresponds to the comparatively low $g_\perp a = 7.94$ value, and which, therefore, in principle should be visible even in the usual, low-resolution, diffraction patterns. This is most probably due to a specific atomic decoration of ZnMgY atomic lattice and the form factors of the (722222) reciprocal lattice nod. We expect the revealed extinction to be of importance for the ZnMgRE lattice atomic-decoration problem.

The rich structure of QC diffraction patterns is usually observed in the synchrotron-radiation facilities XRD studies. Figure 2.10 presents a comparison of our results with the fci-AlPdMn and fci-ZnMgY diffraction patterns recorded using the synchrotron-radiation sources [56, 57].

The face-centred icosahedral AlPdMn quasicrystal is commonly considered to be the most structurally perfect quasicrystalline compound, manifesting the Bragg peaks with $g_{\perp}a$ values up to $g_{\perp}a = 11.4$, as reported by Boudard et al. [56]. As seen from Fig. 2.10(a), where the Boudard et al. [56] results are compared with our data, the fci-ZnMgY quasicrystal evidently manifests Bragg peaks with the lower structure factors. (For example, the fci-ZnMgY $\frac{1}{2}(\bar{3}55555)$ peak corresponds to the complementary $g_{\perp}$-vector of $g_{\perp}a = 22.3$.) Manifestation of the low structure-factor ZnMgY Bragg peaks, which are not observable in AlPdMn, can be due to smaller perpendicular Debye–Waller factors in ZnMgY as compared to those in AlPdMn, as was pointed out by Létoublon et al. [57] and de Boissieu et al. [58].

In Fig. 2.10(b) the fci-ZnMgY diffraction patterns measured in the present study with the usual Cu K_{α} X-ray source are compared with the Létoublon et al. [57] results obtained with a synchrotron X-ray source for the fci-$Zn_{56.8}Mg_{34.6}Y_{8.7}$ single-grain samples, which manifested Bragg peaks with $g_{\perp}a = 17.3$. As seen, the peak resolution in the diffraction patterns is comparable, and in some details our data compete with recorded by the synchrotron-facilities. It does not mean that the synchrotron-facilities do not provide higher instrumental resolution. Of course they do.[3] The more relevant conclusion to be drawn from the comparison, most probably, is, that the investigated samples, grown by Assmus group, are of exceptional structural quality. The assertion will be confirmed by results of optical spectroscopy study (Chapter 5).

2.3 Phason strain

More detailed analysis of the recorded ϑ-2ϑ diffractograms shows that diffraction peaks of one of the investigated five fci-ZnMgY samples are slightly shifted from their theoretical positions, determined by eq. (1.6). The lower

---

[3] The highest $g_{\perp}a$ value, $g_{\perp}a = 35.5$, to our knowledge, was reported in the si-ZnMgSc synchrotron-XRD study [58]. It is twice larger than that of the complementary $\boldsymbol{g}_{\perp}$-vectors we resolved in si-ZnMgHo diffractogram, $g_{\perp}a = 17.3$.

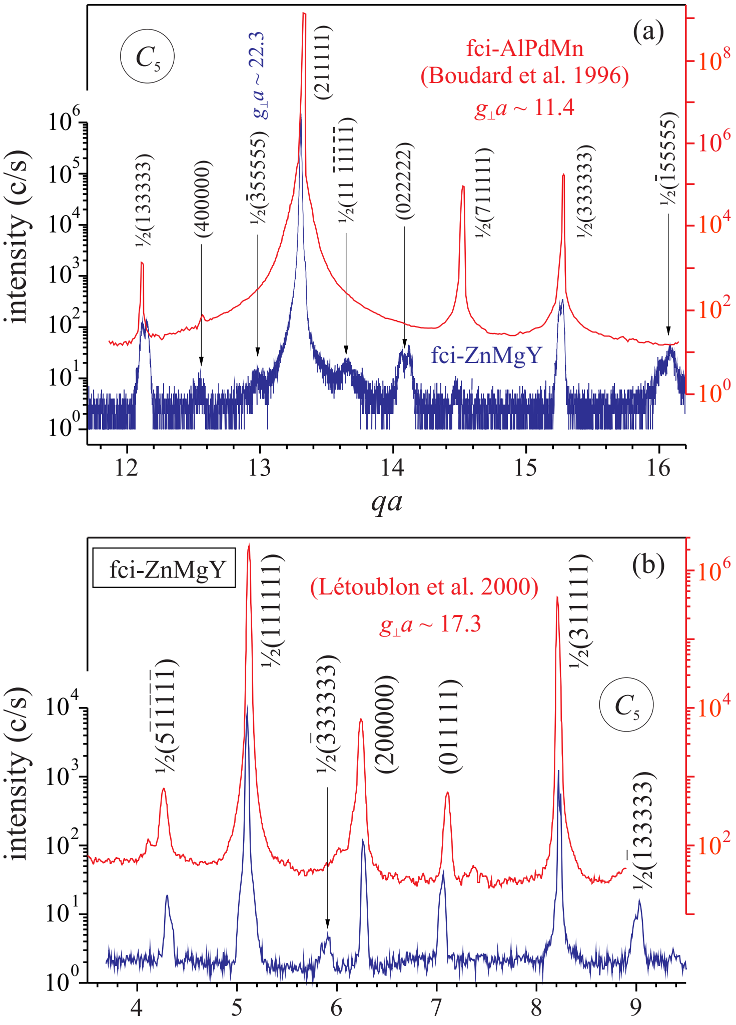

Figure 2.10: Comparison of our results (blue curves) with the fci-AlPdMn (a) and fci-ZnMgY (b) diffractograms recorded using the synchrotron-radiation sources (red curves [56, 57]).

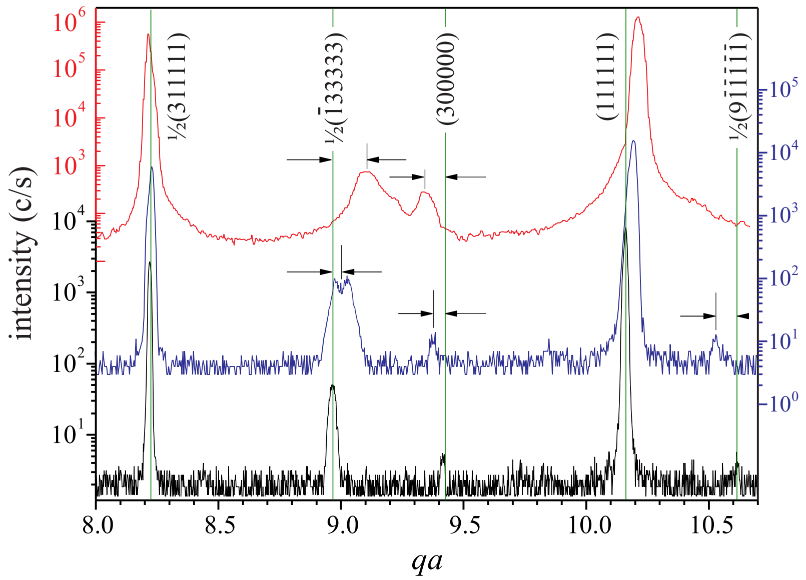

Figure 2.11: Positions of the fci-ZnMgY $\boldsymbol{q} \parallel C_5$ Bragg peaks. The lower curve corresponds to a sample with the peaks at their theoretical positions (1.6). The middle curve presents a sample with shifted Bragg peaks. The upper curve presents for a comparison Létoublon et al. results [57], [59, Fig. 4.48].

diffractogram in Fig. 2.11 corresponds to a sample with the $\boldsymbol{q} \parallel C_5$ Bragg peaks at the theoretical positions indicated by vertical lines in the figure. The middle diffractogram corresponds to a sample, the XRD peaks of which were slightly shifted from the theoretical positions. The upper diffractogram presents for a comparison Létoublon et al. results [57], [59, Fig. 4.48]. As seen, the shifts are larger for the low intensity peaks and acquire different signs.

There is a definite regular dependence of the shifts on the complementary reciprocal lattice vector $\boldsymbol{g}_\perp$. The modulus of the shifts is proportional to a modulus of the $\boldsymbol{g}_\perp$-vector, while the shift sign is determined by the $\boldsymbol{g}_\perp$ direction with respect to the unit vector $\boldsymbol{e}_1^\perp$ (see § 1.3 for $\boldsymbol{e}_1^\perp$ definition). A sign of the peak shift changes when the $\boldsymbol{g}_\perp$-vector flips its direction. The experimental dependence of the peak shifts $\delta g = g_{\mathrm{exper}} - g_{\mathrm{theor}}$ on the complementary $\boldsymbol{g}_\perp$-vector is presented in Fig. 2.12. As seen, the dependence follows the law

$$\delta g = b \left(\boldsymbol{g}_\perp \boldsymbol{e}_1^\perp \right) . \tag{2.6}$$

The law (2.6) of the Bragg peak shifts is a signature of a static linear

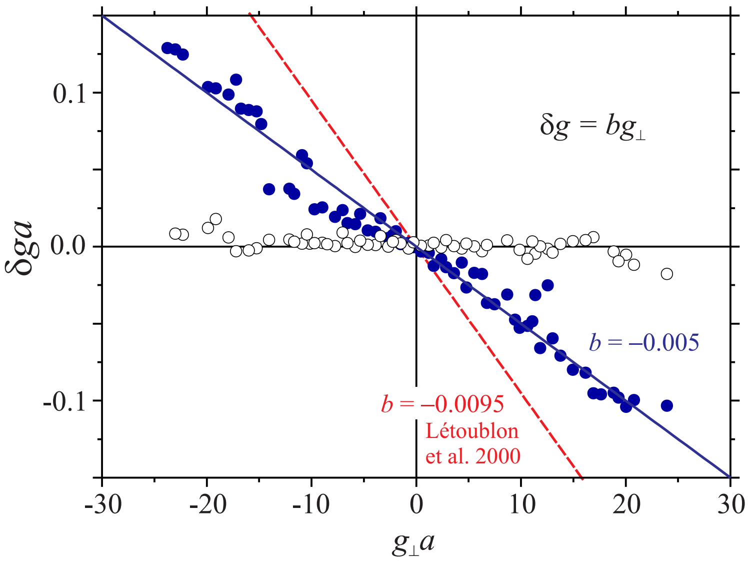

Figure 2.12: Dependence of the $\boldsymbol{q} \parallel C_5$ Bragg peak shifts from their theoretical positions on the complementary reciprocal lattice vector. Full and open dots correspond to the fci-ZnMgY samples, the diffractograms of which are presented by the middle and lower curves, respectively, in Fig. 2.11. Dashed curve presents for a comparison Létoublon et al. results [57].

phason strain [60]. The phasons is a specific subject of quasicrystals and incommensurate phases (see e. g. [40, 61]) and correspond to deformations of the 6D hyperlattice, from which the quasicrystalline lattice is projected. The phasons are in a focuss of the contemporary QC physics. Most of the experimental work so far has been carried out on the fci-AlPdMn phase. The phasons in ZnMgRE quasicrystals previously were observed by Létoublon et al. [57] in fci-ZnMgY and by de Boissieu et al. [58] in the si-ZnMgSc phase, which is closely related with the ZnMgRE family. In Fig. 2.11 – 2.12, a comparison of our results with those reported by Létoublon et al. is presented. As seen, the phason-induced peak shifts in the investigated fci-ZnMgY sample is about twice smaller than the shifts observed by Létoublon et al. [57].

2.4 Reciprocal space mapping

In the theta-2theta XRD measurements, the reciprocal lattice is scanned along a single chosen direction. As seen from Fig. 2.4, the reciprocal lattice nods, which are located away from the ϑ-2ϑ $\boldsymbol{q}$-direction, can be traced by

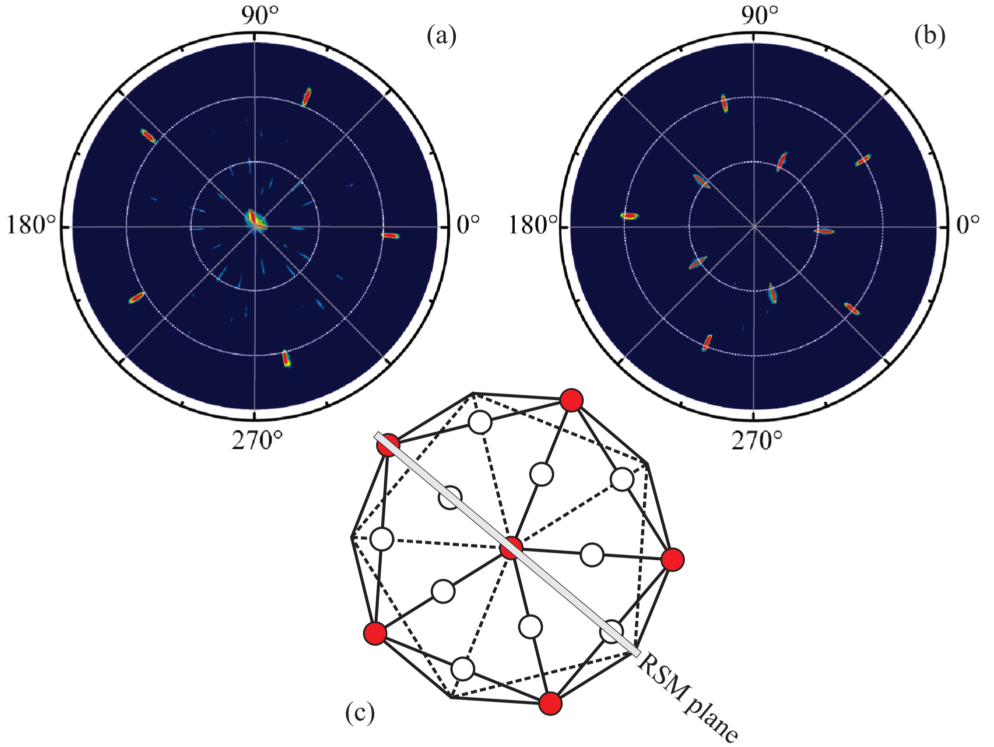

Figure 2.13: The pole figures of (a) the 5-fold 422222 peak ($2\vartheta = 36.6°$) and (b) the 2-fold 442002 peak ($2\vartheta = 38.6°$). The recorded 5-fold and 2-fold poles are indicated by full and open dots, respectively, in a schematic drawing (c), which shows as well the chosen RSM plane.

rotating a detector at a fixed glancing angle ω of the incident X-ray beam or by rotating an X-ray gun at a fixed position of a detector. This allows for measurements of a planar cut of the reciprocal lattice. The technique, known as the reciprocal space mapping (RSM), is exceptionally time consuming, and usually only small sections of the reciprocal space are mapped in the RSM measurements. In the present study, the ultimate-large-scale planar cut of the reciprocal fci-ZnMgY lattice was recorded by making use of a PIXcel area detector.

The RSM measurements were carried out on the fci-ZnMgY sample with C_5 axis perpendicular to its surface. To orient the sample for a RSM scan, the pole figures were recorded (Fig. 2.13), which evidently demonstrate the distinct perfect five-fold symmetry of the quasicrystal. The chosen RSM plane is indicated in Fig. 2.13(c).

The reciprocal space map of the investigated fci-ZnMgY quasicrystal is presented in Fig. 2.14. It corresponds to the reciprocal space plane, which

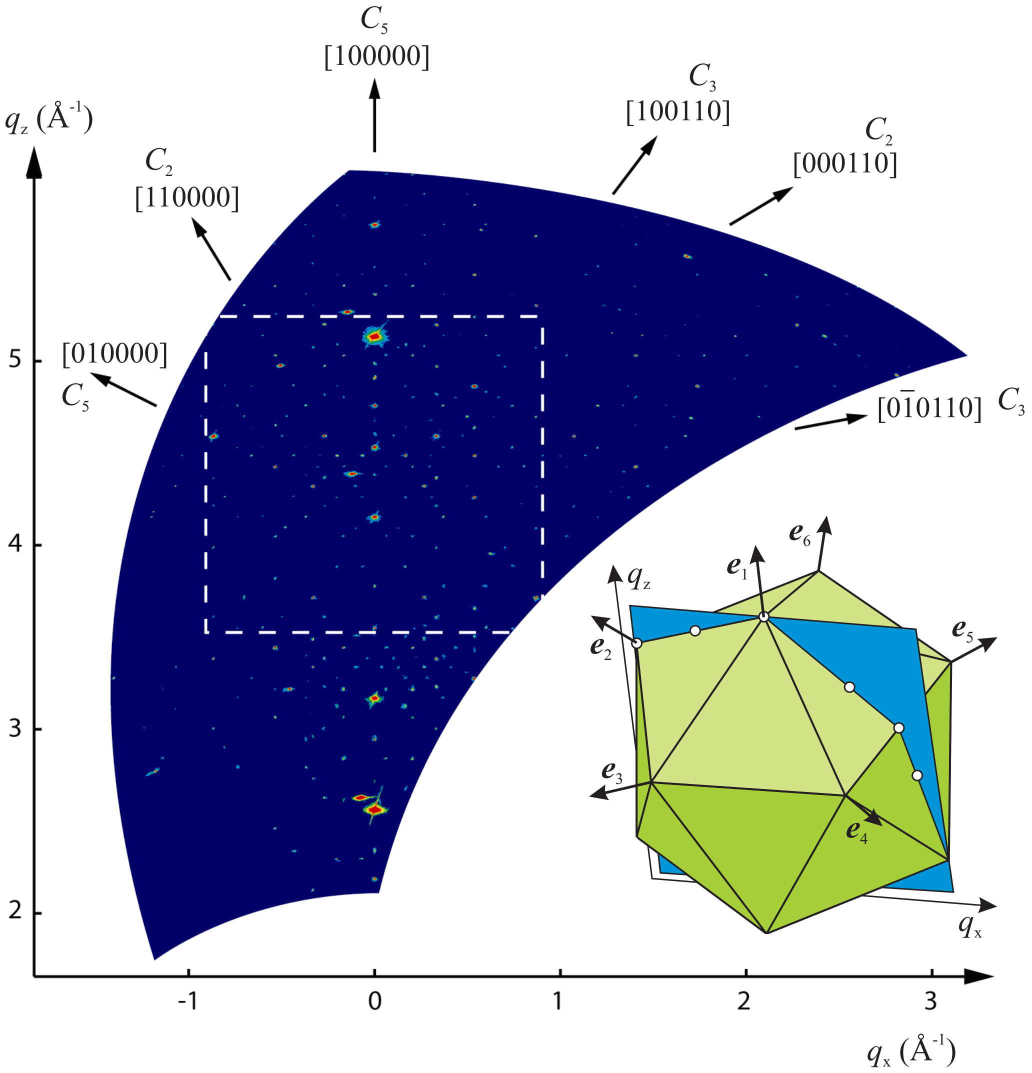

Figure 2.14: The fci-ZnMgY reciprocal space map. The inset indicates an orientation of the RSM plane with respect to an icosahedron. A section of the map, indicated by a white-dashed square, is analysed in Fig. 2.16.

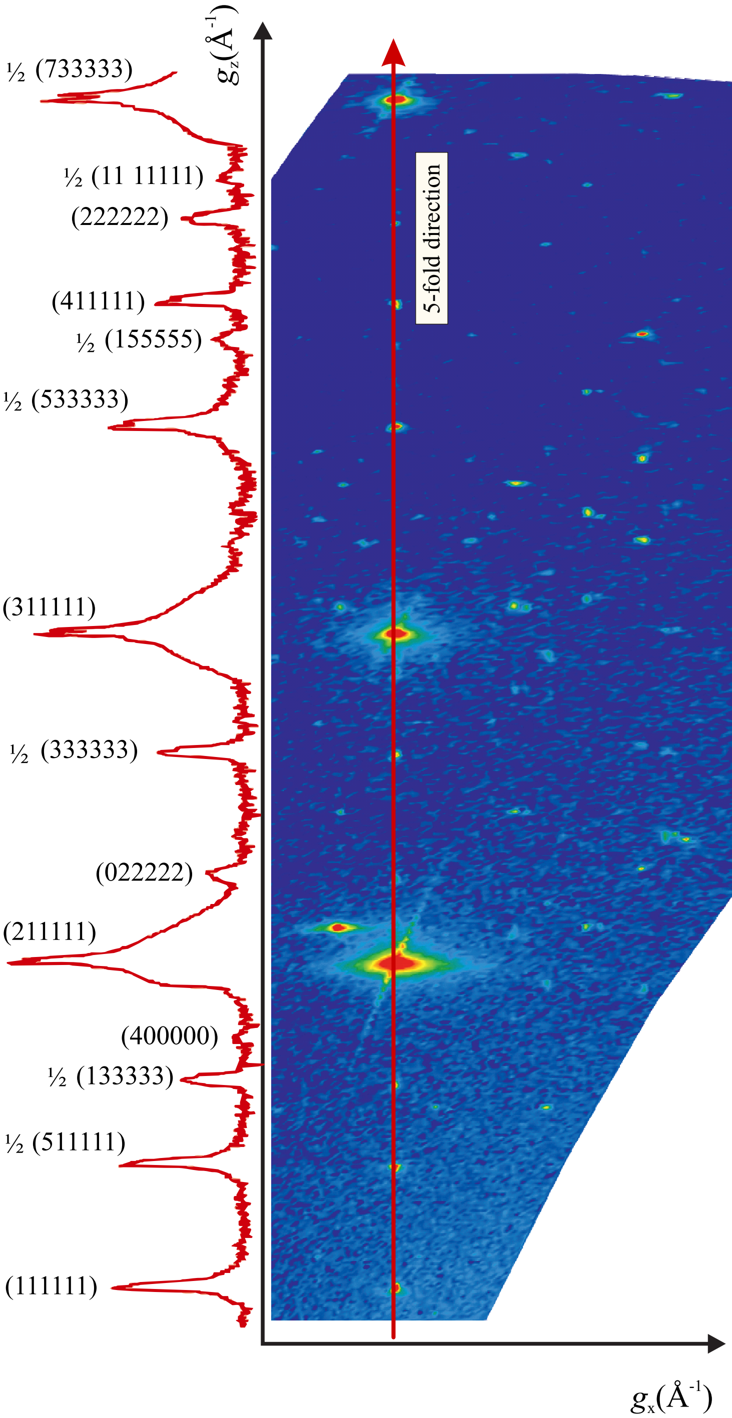

Figure 2.15: The reciprocal space map, when analyzed along definite directions, corresponds to the ϑ-2ϑ scans (§ 2.2.2).

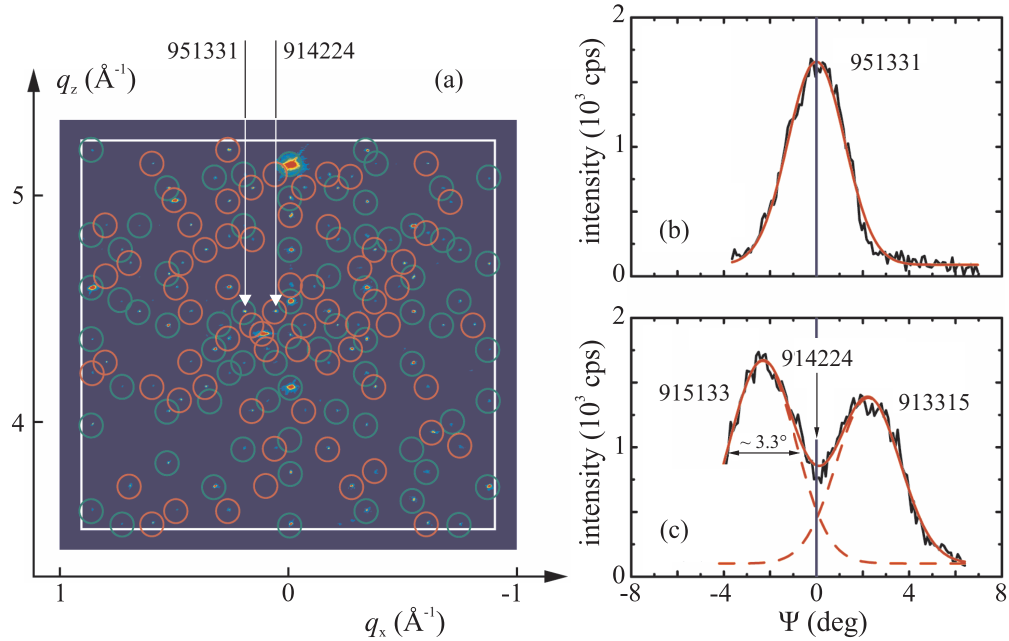

Figure 2.16: (a) A section of the reciprocal space map. Diffraction peaks circled in green and red correspond to the fci and 'bci-like' indices, respectively. Psi-scans of (b) the 951331 fci peak ($2\vartheta = 66.71°$, $\omega = 35.99°$, $q_x = -0.21$ Å^{-1}, $q_z = 4.48$ Å^{-1}) and of (c) the 914224 'bci-like' peak ($2\vartheta = 66.66°$, $\omega = 34.10°$, $q_x = -0.06$ Å^{-1}, $q_z = 4.48$ Å^{-1}).

bisects an icosahedron along its C_5-C_2-C_5-C_3-C_2-C_3 axes, as is indicated in the inset to Fig. 2.14. The map, at the chosen data acquisition time and scan step, took 72 h to record, which is rather fast as compared to the 1.9 years an ordinary point detector would require to record the map.

The map is comprised of about 320 diffraction reflexes. The reflexes along C_5, C_3, and C_2 directions make up the diffraction patterns of ϑ-2ϑ scans (§ 2.2.2), as is illustrated in Fig. 2.15. All reflexes of the map, both lying on the C_5, C_3, and C_2 directions, and away from them, correspond to the reciprocal lattice nodes determined by formula (1.6) and can be successfully identified and indexed in the extended indexing scheme with the six integers n_i at the superstructure constant $a^* = 2 \times 5.185$ Å. A sum of indices of the diffraction peaks is an even number,

$$\sum_{i=1}^{6} n_i = 2n, \tag{2.7}$$

for all peaks of the RSM map.

The requirement for a sum of indices to be an even number is a prerequisite of the body-centred icosahedral (bci) phases. The fci indices are a subset of the bci ones. Indeed, the fci indices, which satisfy the extinction rule (2.4), 'all n_i are either even, or odd', automatically fulfil the requirement (2.7). About 51 % of the recorded RSM diffraction peaks satisfy the fci rule. They are indicated by green circles in Fig. 2.16(a), which presents a section of the RSM map (Fig. 2.14). The other half, 49 %, of the diffraction reflexes (indicated by red circles in Fig. 2.16(a)) correspond to the bci indices, in a sets of which there are both even, and odd integer numbers. Consequently one can assume that the investigated ZnMgY sample is of the body-centred icosahedral phase. However, that is not the case. More detailed analysis shows that the 'bci-like' diffraction peaks are superpositions of the fci ones – each 'bci-like' diffraction peak is due to two fci reciprocal lattice nodes, which are positioned slightly out of the map plane, and which are mirror images of each other across the plane. They are traced in the RS map due to a comparatively low out-of-plane instrumental resolution. One can prove that by scanning the diffraction peak profiles in a direction perpendicular to the plane. The scans can be carried out by varying the sample tilt angle Ψ, what approximately corresponds to a parallel shift of the RSM-plane. The Ψ-scans of the two diffraction reflexes chosen, the fci one, 951331, and the bci-like one, 914224, are presented in Fig. 2.16(b) and Fig. 2.16(c). As seen, the 951331 peak is a "real" one, it really corresponds to the reciprocal lattice vector $\boldsymbol{g}_{951331}$, while the 914224 peak is "empty", the non-existing lattice vector $\boldsymbol{g}_{914224}$ is built up by two fci $\boldsymbol{g}$-vectors,

$$\boldsymbol{g}_{914224} = \tfrac{1}{2}[\boldsymbol{g}_{915133} + \boldsymbol{g}_{913315}], \qquad (9\,1\,4\,2\,2\,4)= \tfrac{1}{2}[(9\,1\,5\,1\,3\,3)+(9\,1\,3\,3\,1\,5)]. \tag{2.8}$$

Therefore, all $\sim$ 300 diffraction reflexes of the recorded reciprocal lattice map confirm the face-centred icosahedral phase of ZnMgY quasicrystal.

2.5 Resumé

Summarizing the present chapter, we conclude that the carried out XRD study of ZnMgRE quasicrystals evidently reveals the main features of the quasicrystalline reciprocal lattice and shows the perfect long-range atomic order of the quasicrystals.

The theta-2theta scans of the ZnMgRE reciprocal space along C_5, C_3, and C_2 symmetry axes are comprised of numerous diffraction peaks with the peak resolution comparable to that usually obtained with the synchrotron-radiation X-ray sources. The low structure-factor diffraction peaks, corresponding to the large complementary reciprocal lattice vectors up to $g_{\perp}a = 23.9$, were detected. This should be compared with the reported values of $g_{\perp}a = 11.4$ for AlPdMn quasicrystals [56] and $g_{\perp}a = 17.3$ for fci-ZnMgY [57], achieved in the synchrotron-facilities XRD studies.

An analysis of the recorded ϑ-2ϑ diffractograms revealed a phason strain in one of the investigated fci-ZnMgY samples.

The recorded ultimate-large-scale fci-ZnMgY reciprocal lattice map should be mentioned as a novel experimental result and should be attributed, first of all, to skilfullness of Fredrik Eriksson and Simon Olsson, our colleagues from Linköping University.

Results of the carried out ZnMgRE quasicrystals XRD study were reported in [10, 15, 16]*.

Chapter 3

Electronic structure. Electron spectrum model

Though the main principles of the atomic structure of quasicrystals are known (Chapter 2), the problem of the electronic structure of quasicrystals, despite of its importance, remains to be in principle unsolved. Since the Bloch theorem is not applicable for aperiodic systems, even the main features of electron quantum mechanical states in quasicrystals are unknown. Are the quantum states localized or extended, is the energy spectrum discrete of continuous remain to be unanswered questions. Consequently, various models of QC electronic structure, which are considered in a literature, remain to be hypothetical. The QC electronic structure is usually considered in the frameworks of two different approaches.

The first, so-called first principles approach treats the quasicrystalline potential acting on an electron subsystem as corresponding to that of the QC approximants – the complex crystalline compounds, an atomic structure of which is locally similar to that of quasicrystals. In the framework of the approach, the problem of QC electronic structure is treated as that of periodic crystals with huge unit cells, containing large numbers of atoms. Then, the relevant techniques of band-structure calculations, usually the tight-binding linear-muffin-tin-orbital (TB-LMTO) method, are used to examine the QC valence bands (see reviews of Fujiwara, Hafner, Krajčí, and Ishii [62, 63, 64]). The first principles calculations predict a distinct spiky structure of the valence band density of states (DOS) and a decrease in DOS at the Fermi level (Fig. 3.1(a)), the so-called pseudogap feature. It should be mentioned that though the DOS spikiness is considered to be a distinc-

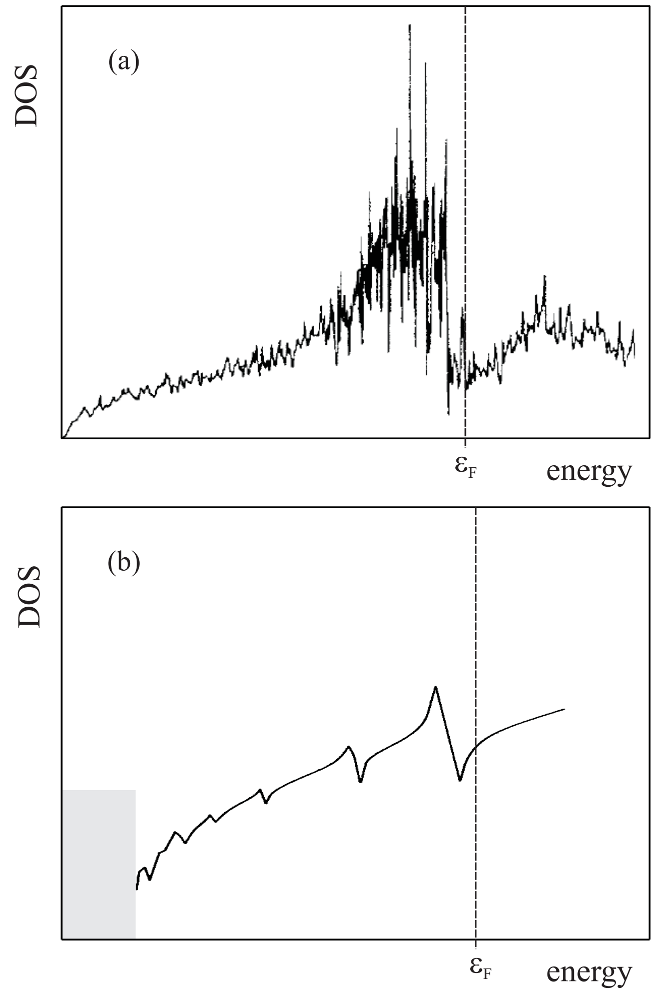

Figure 3.1: Models of QC valence bands based on (a) ‘the first principles calculations’ (adapted from Fujiwara and Yokokawa [65]) and on (b) ‘band structure hypothesis’ (adapted from Smith and Ashcroft [66]).

tive feature of quasicrystals, it was not observed experimentally. This could be due to an intrinsic broadening of electron states, which smears down the predicted spiky structure.

The alternative approach, the so-called ‘band structure hypothesis’, suggested by Smith and Ashcroft [66], treats an electronic subsystem in quasicrystals as the nearly free electron (NFE) gas, affected by a weak quasicrystalline potential

$$V(\boldsymbol{r}) = \sum_{\boldsymbol{g}} V_{\boldsymbol{g}} \exp(\mathrm{i}\boldsymbol{g}\boldsymbol{r}). \tag{3.1}$$

The approach, when only several Fourier amplitudes $V_{\boldsymbol{g}}$ of the QC potential are taken into account, predicts the DOS pseudogap feature as well, but otherwise much more smooth DOS dispersion (Fig. 3.1(b)).

The band structure hypothesis approach, which we will follow in the present thesis, is expected to be a relevant description of the QC electron subsystem, because all quasicrystals are metallic compounds. In metals, whatever their atomic structure is, the atomic lattice potential is presumably weak and the electron subsystem behaves as a nearly free electron gas.

In previous investigations of ZnMgRE quasicrystals, carried out by our group, the band structure hypothesis approach was successfully applied for an analysis of ZnMgRE valence band photoemission (PE) spectra [67, 68, 69, 70]. It was shown, that the experimental valence band spectra can be theoretically simulated assuming that the ZnMgRE electron energy spectrum is determined by the Fermi surface intersections with several families of Bragg planes. The ZnMgRE valence band density of states was calculated making use of the standard NFE approximation scheme and the calculated DOS nicely reproduced the observed PE valence band spectra. Moreover, the NFE calculations qualitatively agreed with results of the 'first principle calculations', independently carried out by the TB-LMTO technique [71, 72].

In the present study, the model of the ZnMgRE QC electron subsystem was further worked out to apply it for an analysis of the ZnMgRE optical response [5]*. Namely, the model was adapted for the extended zone presentation, which is a relevant description for aperiodic systems. Details of the electron subsystem model are presented in the following sections, § 3.1 – 3.3.

3.1 NFE approximation

In the framework of the nearly free electron approximation, the Schrödinger equation for the electron subsystem,

$$\left[-\frac{\hbar^2}{2m_0}\Delta + V(\boldsymbol{r})\right]\Psi = \varepsilon\,\Psi, \tag{3.2}$$

is being solved under an assumption that the atomic lattice potential $V(\boldsymbol{r})$ is weak. If the potential field $V(\boldsymbol{r})$ could be disregarded, the electron wavefunctions and energy spectrum would correspond to those of the free electron gas,

$$\Phi_{\boldsymbol{k}} = \frac{1}{\Omega^{1/2}}\exp(\mathrm{i}\boldsymbol{k}\boldsymbol{r}), \qquad \epsilon_{\boldsymbol{k}} = \frac{\hbar^2 k^2}{2m_0}, \tag{3.3}$$

where Ω is the normalization volume. Since the electrons are subjected to the potential field $V(\boldsymbol{r})$, their quantum states differ from the free electron ones (3.3). However, under the assumption of a weak potential field, electron quasimomentum $\boldsymbol{k}$ presumably remains to be the quantum number, i. e. the electron quantum states remain to be classified by the $\boldsymbol{k}$-vector, $\Psi = \Psi_{\boldsymbol{k}}$, $\varepsilon = \varepsilon(\boldsymbol{k})$.

Within the NFE approximation, solutions of the Schrödinger equation (3.2) are searched for in a basis of the plane waves (3.3). The wave function $\Psi_{\boldsymbol{k}}$ expansion in the $\Phi_{\boldsymbol{k}}$ basis,

$$\Psi_{\boldsymbol{k}} = \sum_{\boldsymbol{g}} C_{\boldsymbol{k}-\boldsymbol{g}} \Phi_{\boldsymbol{k}-\boldsymbol{g}}, \tag{3.4}$$

contains only those plane waves, the wave vectors of which differ from the electron quasimomentum $\boldsymbol{k}$ by the reciprocal lattice vectors $\boldsymbol{g}$, determined by the Fourier expansion (3.1) of the atomic lattice potential $V(\boldsymbol{r})$.

The coefficients of the expansion (3.4) satisfy the system of equations

$$[\epsilon_{\boldsymbol{k}-\boldsymbol{g}} - \varepsilon(\boldsymbol{k})]C_{\boldsymbol{k}-\boldsymbol{g}} + \sum_{\boldsymbol{g}'} V_{\boldsymbol{g}'-\boldsymbol{g}} C_{\boldsymbol{k}-\boldsymbol{g}'} = 0, \tag{3.5}$$

which is derived by projecting the Schrödinger equation (3.2) onto the $\Phi_{\boldsymbol{k}}$-basis vectors (see, e. g., [73]). Here $\epsilon_{\boldsymbol{k}-\boldsymbol{g}} = \hbar^2(\boldsymbol{k}-\boldsymbol{g})^2/2m_0$. The system of equations (3.5) is infinitely large. Its equations are numbered by the reciprocal lattice vectors $\boldsymbol{g}$.

Though the reciprocal lattice of quasicrystals is dense, the structure factors of most of its nodes are rather small, and only comparatively small number of $\boldsymbol{g}$-vectors are of physical importance. The $\boldsymbol{g}$-vectors, which play a decisive role in the quasicrystalline potential (3.1), correspond to the Bragg planes, which are in a close proximity to the Fermi surface. The physically important $\boldsymbol{g}$-vectors can be determined from the experimental X-ray diffraction patterns (§ 2.1).

Let us call a set of the physically important $\boldsymbol{g}$-vectors as the $\mathcal{G}$ star. In ZnMgRE quasicrystals, the $\mathcal{G}$-star is comprised of sixty $\boldsymbol{g}_{222100}$ vectors and twelve $\boldsymbol{g}_{311111}$ ones. The $\boldsymbol{g}_{311111}$ vectors are directed along C_5 axes of icosahedron. The subset of the $\boldsymbol{g}_{222100}$ vectors is constituted of twenty triads, which group around C_3 axes, as is illustrated in Fig. 3.2(a) for the $\{\boldsymbol{g}_{222100}, \boldsymbol{g}_{222001}, \boldsymbol{g}_{2220\bar{1}0}\}$ triad, grouping around $\boldsymbol{g}_{222000} \parallel C_3$.

The $\mathcal{G}$-star determines the effective Brillouin zone (Fig. 3.2(b)), the faces of which correspond to the Bragg planes bisecting the $\boldsymbol{g} \in \mathcal{G}$ vectors.

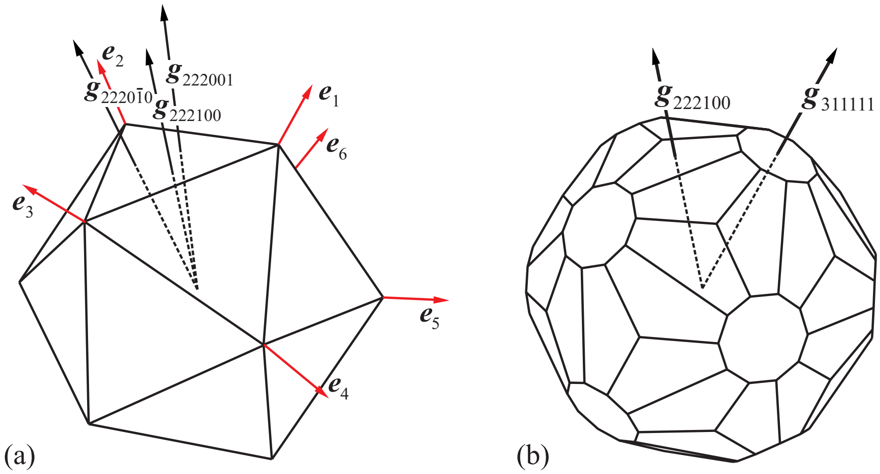

Figure 3.2: Directions of the $\boldsymbol{g}_{222100}$, $\boldsymbol{g}_{222001}$, and $\boldsymbol{g}_{2220\bar{1}0}$ vectors (a) and the effective 222100 and 311111 Brillouin zone (b).

The electron energy spectrum problem can be essentially simplified by leaving only the $\boldsymbol{g} \in \mathcal{G}$ terms in the Fourier expansion of the quasicrystalline potential (3.1),[1]

$$V(\boldsymbol{r}) = \sum_{\boldsymbol{g}\in\mathcal{G}} V_{\boldsymbol{g}} \exp(\mathrm{i}\boldsymbol{g}\boldsymbol{r}), \tag{3.6}$$

and only the corresponding plane waves in the wavefunction expansion (3.4),

$$\Psi_{\boldsymbol{k}} = C_{\boldsymbol{k}}\Phi_{\boldsymbol{k}} + \sum_{\boldsymbol{g}\in\mathcal{G}} C_{\boldsymbol{k}-\boldsymbol{g}}\Phi_{\boldsymbol{k}-\boldsymbol{g}}. \tag{3.7}$$

Then, the system of equations (3.5) reduces to the finite form

$$\left[\epsilon_{\boldsymbol{k}} - \varepsilon(\boldsymbol{k})\right] C_{\boldsymbol{k}} + \sum_{\boldsymbol{g}\in\mathcal{G}} V_{\boldsymbol{g}} C_{\boldsymbol{k}-\boldsymbol{g}} = 0, \tag{3.8}$$

$$\left[\epsilon_{\boldsymbol{k}-\boldsymbol{g}} - \varepsilon(\boldsymbol{k})\right] C_{\boldsymbol{k}-\boldsymbol{g}} + V_{-\boldsymbol{g}} C_{\boldsymbol{k}} = 0. \tag{3.9}$$

In a derivation of the latter system, it was taken into account that a sum of any $\boldsymbol{g} \in \mathcal{G}$ vectors does not belong to the $\mathcal{G}$-star.

Equation (3.9) can be trivially solved with respect to $C_{\boldsymbol{k}-\boldsymbol{g}}$ coefficient,

$$C_{\boldsymbol{k}-\boldsymbol{g}} = \frac{V_{-\boldsymbol{g}}}{\varepsilon(\boldsymbol{k}) - \epsilon_{\boldsymbol{k}-\boldsymbol{g}}} C_{\boldsymbol{k}}. \tag{3.10}$$

Inserting this formula into eq. (3.8), one obtains the algebraic dispersion equation

$$\varepsilon(\boldsymbol{k}) - \epsilon_{\boldsymbol{k}} = \sum_{\boldsymbol{g}\in\mathcal{G}} \frac{|V_{\boldsymbol{g}}|^2}{(\varepsilon(\boldsymbol{k}) - \epsilon_{\boldsymbol{k}}) - (\epsilon_{\boldsymbol{k}-\boldsymbol{g}} - \epsilon_{\boldsymbol{k}})}, \tag{3.11}$$

---

[1] In the expansion (3.6), the V_0 term was eliminated by shifting an energy reference point.

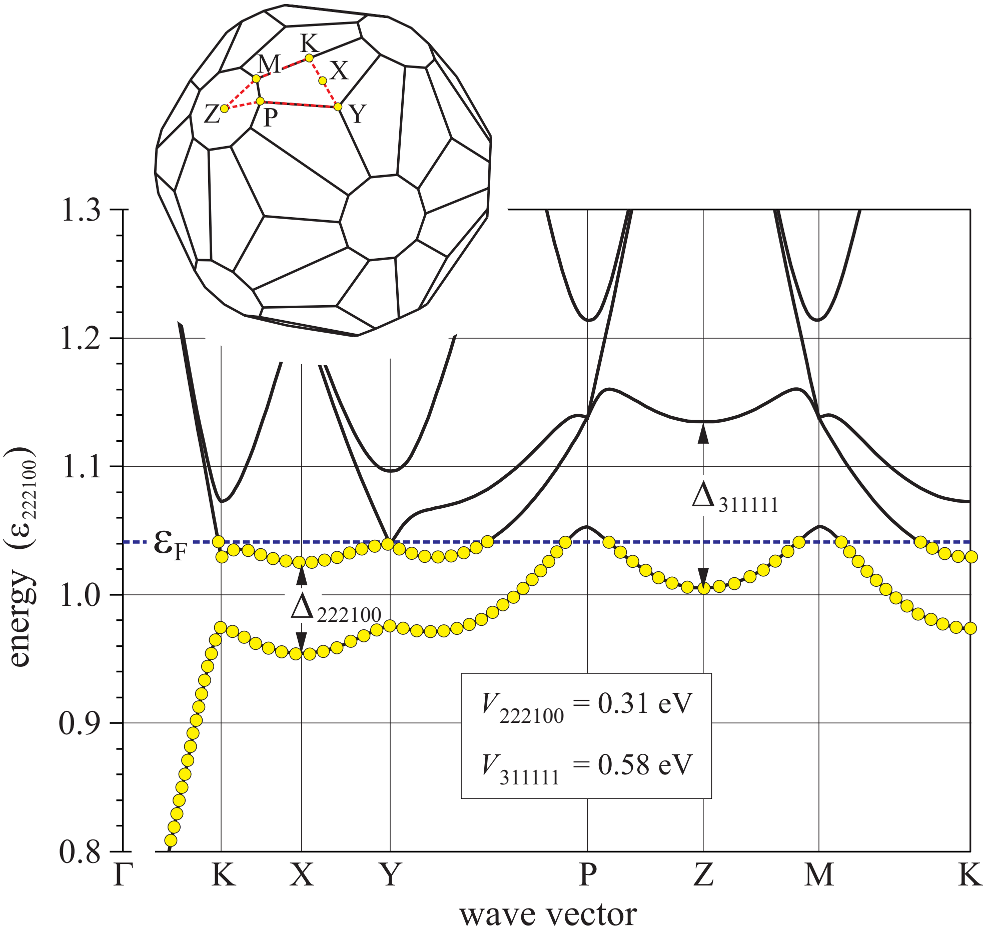

Figure 3.3: Energy spectrum of ZnMgRE quasicrystals in a vicinity of the Fermi level [74], [5]* (at the pseudopotential values of $V_{222100} = 0.31$ eV, $V_{311111} = 0.58$ eV and the Fermi energy $\varepsilon_F = 9.31$ eV determined from an analysis of the experimental fci-ZnMgY PE data [68]).

which determines the energy spectrum $\varepsilon(\boldsymbol{k})$ of the NFE electrons. The order of the equation is determined by the number of $\boldsymbol{g} \in \mathcal{G}$ vectors.

The dispersion equation (3.11) for the ZnMgRE electron energy spectrum can be solved numerically at given values of two parameters, $|V_{222100}|$ and $|V_{311111}|$. The spectrum, calculated at the $V_{222100} = 0.31$ eV and $V_{311111} = 0.58$ eV values of the pseudopotentials, which were determined in an analysis of the experimental fci-ZnMgY PE valence band spectra [68], is presented in Fig. 3.3. Since the V_{222100} and V_{311111} pseudopotentials acquire similar values in fci-ZnMgHo, si-ZnMgHo, and fci-ZnMgEr quasicrystals [68, 69, 70], the energy spectrum in Fig. 3.3 can be considered as a hypothetical band structure of all ZnMgRE quasicrystals studied. The energy spectrum is presented in the $\varepsilon_{222100} = \hbar^2(\frac{1}{2}q_{222100})^2/2m_0$ units and is depicted along the KXYPZMK path on faces of the effective Brillouin zone (see inset of Fig. 3.3). As seen from Fig. 3.3, the Fermi level, which is indicated by a dashed line, is slightly above the $\Delta_{222100} = 2|V_{222100}|$ energy gap and lies in a lower part of the $\Delta_{311111} = 2|V_{311111}|$ gap. Therefore, both energy gaps should contribute to the ZnMgRE interband optical transitions (Section 5).

The ZnMgRE optical spectra, in principle, can be numerically calculated making use of the presented hypothetical band structure scheme. However, since only definite regions of $\boldsymbol{k}$-space are of importance for optical transitions, the analytical calculations, which take into account detailed description of the energy spectrum in a vicinity of energy gaps, are much more effective.

3.2 Two-band model

The energy spectrum of the NFE gas is essentially affected by the quasicrystalline potential at intersections of the isoenergetic surface with Bragg planes. In the proximity to a chosen Bragg plane, $\epsilon_{\boldsymbol{k}} \approx \epsilon_{\boldsymbol{k}-\boldsymbol{g}}$, the denominator of the corresponding term in the right-hand side of the dispersion equation (3.11) becomes small and the term becomes dominant. Leaving only the leading term in the dispersion equation, we can rewrite it in the form

$$\delta\varepsilon_{\boldsymbol{g}}(\boldsymbol{k}) = \frac{|V_{\boldsymbol{g}}|^2}{\delta\varepsilon_{\boldsymbol{g}}(\boldsymbol{k}) - (\epsilon_{\boldsymbol{k}-\boldsymbol{g}} - \epsilon_{\boldsymbol{k}})}. \tag{3.12}$$

Here $\delta\varepsilon_{\boldsymbol{g}}(\boldsymbol{k}) = \varepsilon(\boldsymbol{k}) - \epsilon_{\boldsymbol{k}}$ is a deviation from the free electron spectrum due to an intersection with a single Bragg plane.

The dispersion equation (3.12) corresponds to the NFE two-band model, when an interaction of only two plane waves, $\Phi_{\boldsymbol{k}}$ and $\Phi_{\boldsymbol{k}-\boldsymbol{g}}$, is taken into account,

$$\Psi_{\boldsymbol{k}} = C_{\boldsymbol{k}}\Phi_{\boldsymbol{k}} + C_{\boldsymbol{k}-\boldsymbol{g}}\Phi_{\boldsymbol{k}-\boldsymbol{g}}. \tag{3.13}$$

Solutions of eq. (3.12) correspond to two well-known NFE energy spectrum branches

$$\delta\varepsilon_{\boldsymbol{g}}(\boldsymbol{k}) = \tfrac{1}{2}(\epsilon_{\boldsymbol{k}-\boldsymbol{g}} - \epsilon_{\boldsymbol{k}}) \pm \tfrac{1}{2}\sqrt{(\epsilon_{\boldsymbol{k}-\boldsymbol{g}} - \epsilon_{\boldsymbol{k}})^2 + 4|V_{\boldsymbol{g}}|^2}. \tag{3.14}$$

The energy spectrum (3.14) is graphically presented in Fig. 3.4, where it is plotted both along the $\boldsymbol{g}$-vector direction (Fig. 3.4(a)), and in a plane

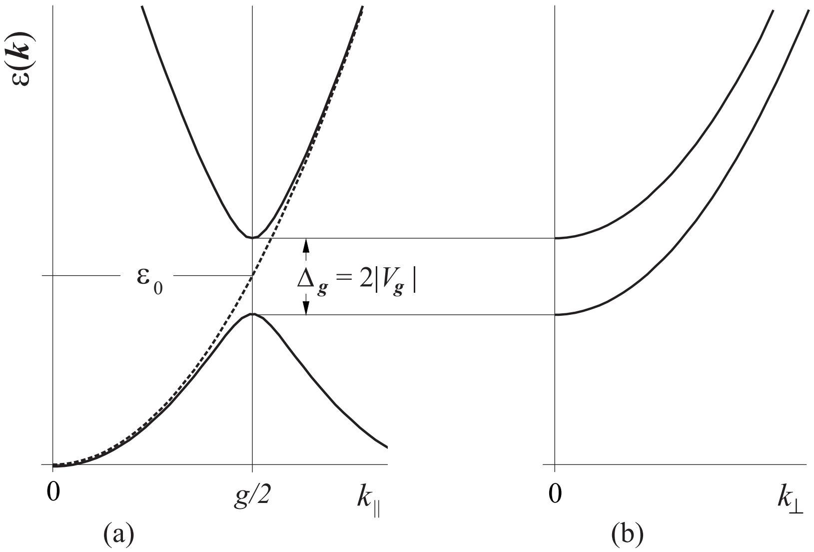

Figure 3.4: The two-band model of NFE spectrum.

perpendicular to $\boldsymbol{g}$-vector (Fig. 3.4(b)). The free electron energy spectrum $\epsilon_{\boldsymbol{k}}$, presented by dashed curve in Fig. 3.4, is distorted at its intersection with the Bragg plane, where the energy gap $\Delta_{\boldsymbol{g}} = 2|V_{\boldsymbol{g}}|$ opens. Note that the gap opens for the distinct $\boldsymbol{k}$-vectors only. Since there are electron states with energies within the gap, $\varepsilon(\boldsymbol{k}) \in [\varepsilon_0 - \frac{1}{2}\Delta_{\boldsymbol{g}}, \varepsilon_0 + \frac{1}{2}\Delta_{\boldsymbol{g}}]$, the gap in metal physics is called as the pseudogap.

The energy spectrum formula (3.14) can be rewritten in a convenient form

$$\delta\varepsilon_{\boldsymbol{g}}(\boldsymbol{k}) = \frac{\Delta_{\boldsymbol{g}}}{2}\left(\gamma \pm \sqrt{\gamma^2+1}\right), \tag{3.15}$$

where γ is a dimensionless function of the quasimomentum $\boldsymbol{k}$ component $k_\parallel$ along the $\boldsymbol{g}$-direction,

$$\gamma = \frac{\epsilon_{\boldsymbol{k}-\boldsymbol{g}} - \epsilon_{\boldsymbol{k}}}{\Delta_{\boldsymbol{g}}} = \frac{4\varepsilon_0}{\Delta_{\boldsymbol{g}}}\left(1 - \frac{k_\parallel}{\frac{1}{2}g}\right), \tag{3.16}$$

and ε_0 is the intersection energy,

$$\varepsilon_0 = \frac{\hbar^2(\frac{1}{2}g)^2}{2m_0}. \tag{3.17}$$

The two solutions of the energy spectrum (3.15) can be chosen arbitrary. In the reduced band presentation, the electron states are considered in the $k_\parallel < g/2$ region only and the band index n is being introduced, $\varepsilon_n(\boldsymbol{k})$, to indicate the lower and upper energy branches. This corresponds to a reduction of the quantum states into the Brillouin zone, which is a convenient tool for a description of the electron subsystem in crystalline solids. However, since the reduction can be strictly justified within the framework of Bloch theorem only, in quasicrystals the extended zone presentation is more relevant.

Within the extended zone presentation, electron states are considered in a whole $\boldsymbol{k}$-space and the lower-sign solution (3.14) is chosen for the $k_\parallel < \frac{1}{2}g$ region, while the upper-sign solution (3.14) is taken for $k_\parallel > \frac{1}{2}g$. Then, the energy spectrum (3.15) can be rewritten in the form

$$\delta\varepsilon_{\boldsymbol{g}}(\boldsymbol{k}) = \frac{\Delta_{\boldsymbol{g}}}{2}\left(\gamma - \frac{\gamma}{|\gamma|}\sqrt{\gamma^2+1}\right). \tag{3.18}$$

3.3 Model of independent intersections

The deviation from the free electron spectrum (3.18) corresponds to an intersection with a single Bragg plane. The total electron energy spectrum is determined by the dispersion equation (3.11), which, taking into account (3.12), can be rewritten in the form

$$\varepsilon(\boldsymbol{k}) - \epsilon_{\boldsymbol{k}} = \sum_{\boldsymbol{g}\in\mathcal{G}} \delta\varepsilon_{\boldsymbol{g}}(\boldsymbol{k})\,\frac{\delta\varepsilon_{\boldsymbol{g}}(\boldsymbol{k}) - (\epsilon_{\boldsymbol{k}-\boldsymbol{g}} - \epsilon_{\boldsymbol{k}})}{(\varepsilon(\boldsymbol{k}) - \epsilon_{\boldsymbol{k}}) - (\epsilon_{\boldsymbol{k}-\boldsymbol{g}} - \epsilon_{\boldsymbol{k}})}. \tag{3.19}$$

In the extended zone presentation, the deviations $\delta\varepsilon_{\boldsymbol{g}}(\boldsymbol{k})$ are localized in close proximity to Bragg planes, within the narrow strips of the $\Delta_{\boldsymbol{g}}/4\varepsilon_0$ width (measured in $\frac{1}{2}g$ units). Under the assumption that strips do not overlap, the electron energy spectrum, determined by equation (3.19), can be presented in the simple form

$$\varepsilon(\boldsymbol{k}) = \epsilon_{\boldsymbol{k}} + \sum_{\boldsymbol{g}\in\mathcal{G}} \delta\varepsilon_{\boldsymbol{g}}(\boldsymbol{k}), \tag{3.20}$$

which shows that a deviation of the spectrum from the free electron parabola $\epsilon_{\boldsymbol{k}}$ is a sum of partial deviations due to Bragg planes.

The assumption of non-overlapping strips corresponds to a model of independent intersections of the isoenergetic surface with Bragg planes. The wave function in the framework of the model is determined by the expansion

$$\Psi_{\boldsymbol{k}} = C_{\boldsymbol{k}}\Phi_{\boldsymbol{k}} + \sum_{\boldsymbol{g}\in\mathcal{G}} C_{\boldsymbol{k}-\boldsymbol{g}}\Phi_{\boldsymbol{k}-\boldsymbol{g}}, \tag{3.21}$$

where $C_{\boldsymbol{k}-\boldsymbol{g}}$ coefficients are found from (3.10) by replacing $\varepsilon(\boldsymbol{k}) \to \epsilon_{\boldsymbol{k}} + \delta\varepsilon_{\boldsymbol{g}}(\boldsymbol{k})$,

$$C_{\boldsymbol{k}-\boldsymbol{g}} = \frac{V_{-\boldsymbol{g}}}{|V_{\boldsymbol{g}}|}\left(\gamma - \frac{\gamma}{|\gamma|}\sqrt{\gamma^2+1}\right) C_{\boldsymbol{k}}, \tag{3.22}$$

while the $C_{\boldsymbol{k}}$ coefficient is found from the normalization condition,

$$|C_{\boldsymbol{k}}|^2 = \frac{1}{1 + \sum_{\boldsymbol{g} \in \mathcal{G}} (\gamma - \frac{\gamma}{|\gamma|}\sqrt{\gamma^2 + 1})^2}. \tag{3.23}$$

The model of independent intersections breaks down at edges and vertices of the effective Brillouin zone. Since they take a considerably smaller phase-space than the BZ faces, the model should be a relevant tool for a description of the optical transitions in quasicrystals, and we will use it in analyzing an optical response of QCs (Chapter 5). However, one should keep in mind that the model can be violated even away from the Brillouin zone edges. When angles between the $\boldsymbol{g} \in \mathcal{G}$ Bragg planes are small, an overlap of the strips, within which the deviations $\delta\varepsilon_{\boldsymbol{g}}(\boldsymbol{k})$ are localized, can become of importance, and the model of independent intersections will overestimate the partial contributions of the planes. In the $\mathcal{G}$-star of ZnMgRE QCs, this can be the case for the (222100) triads. Indeed, the angle between $\boldsymbol{g}$ vectors of the triad is comparatively small, about 19.4°. To remedy the situation, when modelling an optical response of the quasicrystals, we will treat each triad of the (222100) subset as a single Bragg plane.

3.4 Resumé

The model of ZnMgRE electron energy spectrum, based on the band structure hypothesis, was developed – a hypothetical band structure of the fci-ZnMgRE quasicrystals in a vicinity of the Fermi level was calculated and the NFE model of independent intersections was formulated in the extended zone presentation.

Chapter 4

Optical spectroscopy. Experimental

Optical spectroscopy is one of the principle experimental tools for a determination of the electronic structure of materials.

In this chapter, we will shortly survey the optical spectroscopy techniques used in the present work for the ZnMgRE electronic structure studies, namely, the spectroscopic ellipsometry (§ 4.1) and the reflectance spectroscopy (§ 4.2), which were employed to examine an optical response of the quasicrystals in the IR-UV and FIR spectral ranges, correspondingly.

In section § 4.3, the suggested anchor-window technique of the Kramers–Kronig analysis will be presented. It allowed us to obtain the reliable, high-accuracy ZnMgRE dielectric function and optical conductivity spectra in the wide spectral range of 0.01 – 6 eV.

The employed optical-surface preparation techniques will be described in section § 4.4, and, finally, in section § 4.5, a structure of the ZnMgRE surface layers will be briefly discussed.

4.1 Spectroscopic ellipsometry

The spectroscopic ellipsometry (SE) is based on measurements of the light polarization changes which occur when the incident polarized light beam is reflected by a sample (detailed description of the SE technique is given in [75, 76, 77]). The main advantage of the spectroscopic ellipsometry is a possibility of a direct determination of both the real, and imaginary parts of the dielectric function $\varepsilon(\omega)$ or the optical conductivity of a material under

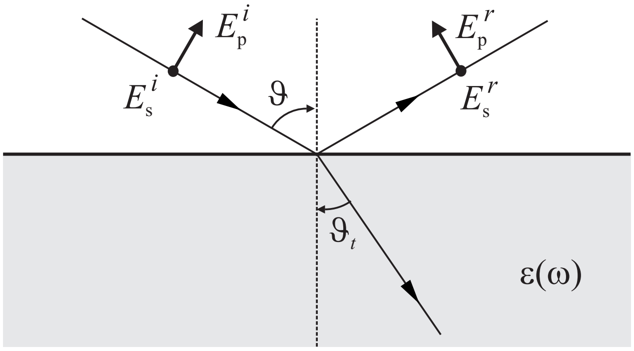

Figure 4.1: The electric field vector of a linearly polarized light can be projected into two, s and p, orthogonal polarization components.

investigation. All other methods of optical spectroscopy yield data, which correspond to spectra of some distinct combinations of optical parameters, and, therefore, either additional measurements, or an additional non-trivial analysis of the data are required. Other important SE advantages are an insensitivity to a drift of the incident light beam intensity and a sensitivity to a surface state of samples, which allows for a detection of the thin surface layers, typically of about ~ 1 nm thickness.

4.1.1 SE principles

The electric field vector $\boldsymbol{E}$ of a linearly polarized light can be projected into two, s and p, orthogonal polarization components (Fig. 4.1). The p-polarized electric field component E_p is parallel to the plane of incidence, which is defined by the incident beam and the optical-surface normal. The s-polarized component E_s is perpendicular to the plane of incidence. The complex reflection amplitudes r_p and r_s, which are the ratios of the p- and s- electric field components of the reflected and incident light waves, are determined by the Fresnel equations

$$r_\mathrm{p} = \frac{E_\mathrm{p}^r}{E_\mathrm{p}^i} = \frac{\varepsilon(\omega)\cos\vartheta - \sqrt{\varepsilon(\omega) - \sin^2\vartheta}}{\varepsilon(\omega)\cos\vartheta + \sqrt{\varepsilon(\omega) - \sin^2\vartheta}}, \tag{4.1}$$

$$r_\mathrm{s} = \frac{E_\mathrm{s}^r}{E_\mathrm{s}^i} = \frac{\cos\vartheta - \sqrt{\varepsilon(\omega) - \sin^2\vartheta}}{\cos\vartheta + \sqrt{\varepsilon(\omega) - \sin^2\vartheta}}, \tag{4.2}$$

where superscripts r and i indicate the reflected and incident beams, ϑ is the incidence angle, and $\varepsilon(\omega)$ is the dielectric function of the material under investigation.

As seen from the Fresnel equations (4.1)–(4.2), the s- and p-polarized light is differently reflected by a sample. As a result, the linearly polarized light upon reflection, in a general case, acquires an elliptical polarization, which is described by two ellipsometric parameters Ψ and Δ, defined as

$$\varrho = \frac{r_\mathrm{p}}{r_\mathrm{s}} = \tan\Psi\, \mathrm{e}^{\mathrm{i}\Delta}. \tag{4.3}$$

The ellipsometric parameters Ψ and Δ are directly recorded in SE measurements. As seen from (4.3), they correspond to a modulus of the reflection amplitude ratio and a phase difference,

$$\tan\Psi = \frac{|r_\mathrm{p}|}{|r_\mathrm{s}|}, \qquad \Delta = \delta_\mathrm{p} - \delta_\mathrm{s}. \tag{4.4}$$

Making use of the Fresnel formulas (4.1)–(4.2), the ellipsometry equation (4.3) can be solved with respect to the dielectric function,

$$\varepsilon(\omega) = \sin^2\vartheta \left[1 + \tan^2\vartheta \left(\frac{1-\varrho}{1+\varrho}\right)^2\right]. \tag{4.5}$$

The latter formula shows that the experimental spectrum of a complex ellipsometric parameter ϱ directly yields a spectrum of a complex dielectric function of the system under investigation.

For optically anisotropic systems, the dielectric function of which is a tensorial quantity, several measurements of the ellipsometric parameter ϱ spectra are required at different orientations of the incident beam with respect to crystallographic axes (generalized SE). Then, the formula (4.5) yields the so called pseudodielectric function (PDF), which depends on the principle components of the dielectric function tensor, as well as on the incidence and the crystallographic angles,

$$\varepsilon_\mathrm{PDF}(\omega) = f(\varepsilon_1(\omega), \varepsilon_2(\omega), \varepsilon_3(\omega), \vartheta, \ldots). \tag{4.6}$$

When the optical response is affected by the surface layers, the PDF-function depends on the bulk and surface dielectric functions, on the width of surface layers, and on the incidence angle,

$$\varepsilon_\mathrm{PDF}(\omega) = f(\varepsilon(\omega), \varepsilon_{\mathrm{s},1}(\omega), d_{\mathrm{s},1}, \varepsilon_{\mathrm{s},2}(\omega), d_{\mathrm{s},2}, \ldots, \vartheta). \tag{4.7}$$

The explicit formulas for the PDF-function of the double surface layer system were derived in [19]*.

4.1.2 SE data analysis

The ellipsometry data analysis, depending on the parameters of interest and a structure of the system under investigation, can be carried out in the frameworks of different approaches.

Traditionally, wavelength by wavelength best-match calculations are performed. Then, the dielectric function values are extracted from SE data at each wavelength, independently of other spectral data points. For the optically isotropic systems without surface layers, this technique is equivalent to a result of formula (4.5) and was used in the present work for a determination of the bulk dielectric function of quasicrystals.

For investigations of the ZnMgRE surface layers [78, 79], of the uniaxial monocrystalline zinc [11, 17]* and/or of heterostructured physical systems [20, 21, 22] other techniques of SE data analysis are more convenient.

Frequently employed, robust procedure is a parametric matching of the model dielectric function to experimental SE data simultaneously for all spectral data points. Parametric models prevent wavelength-by-wavelength measurement noise from becoming part of the extracted dielectric functions and greatly reduce the number of free parameters. The technique is used, when the physical origin of optical features is known or anticipated, and only the parameters of the optical features are to be determined.

An alternative way to parameterize an arbitrary dielectric function is to use a polynomial B-spline technique [80]. The technique combines the versatility of the wavelength by wavelength best-match model and the effectiveness of parametric models, avoiding postulates of the $\varepsilon(\omega)$ spectral shape.

4.1.3 Spectroscopic ellipsometers

NIR–UV ellipsometry

The spectroscopic ellipsometry measurements in the near-infrared (NIR) – ultraviolet (UV) spectral range (0.7 – 6 eV) were carried out with several different ellipsometric setups:

- The original rotating analyzer ellipsometer RAE (Semiconductor Optics Laboratory).
- Sopra GES 5 variable-angle broadband spectroscopic ellipsometer (Institute of Physics). Spectral range 210 – 900 nm (1.4 – 6 eV).

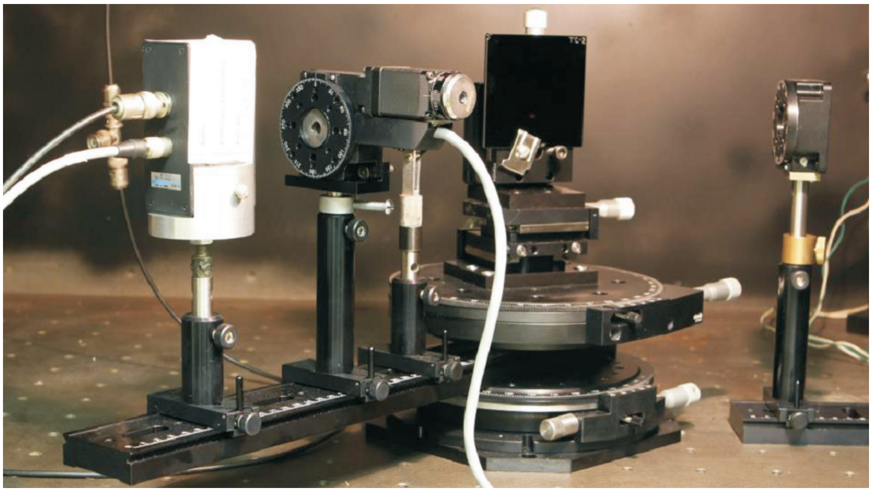

Figure 4.2: The sample stage of the rotating analyzer ellipsometer RAE.

- J. A. Woollam Co. ellipsometer VASE (Linköping University).
- J. A. Woollam Co. ellipsometer M-2000 based on rotating compensator with high-speed CCD detection (Vilnius University, Faculty of Chemistry). Spectral range 245 – 1000 nm (1.2 – 5 eV).
- J. A. Woollam Co. ellipsometer RC2 (Semiconductor Optics Laboratory).

The best results were obtained on RAE, VASE, and RC2 ellipsometers. The results were well-reproducible. The dielectric function spectra recorded on the ellipsometers coincided with each other with an accuracy of several percents.

RAE ellipsometer. The original rotating-analyzer photometric ellipsometer RAE (Fig. 4.2) is equipped with the high pressure mercury and incandescent lamps, which ensure the wide-range radiation spectra. The light beam at the exit of a dispersive monochromator is mechanically modulated by a rotating chopper. The polarizer is mounted at 45° with respect to the incidence plain. The elliptical polarization of reflected beam is scanned by rotating an analyzer with the stepping motor. The angle of incidence ϑ can be chosen in the interval of 10° – 90° and set with an accuracy of 0.01°. The spectral range of SE measurements is 0.5 – 5 eV with the spectral resolution of 0.01 eV.

Figure 4.3: J. A. Woollam RC2 ellipsometer.

VASE ellipsometer. The spectroscopic ellipsometer VASE (J. A. Woollam Co Inc.) is installed at Linköping University (Prof. H. Arwin laboratory). The VASE ellipsometer is based on rotating analyzer and is combined with patented AutoRetarder for unparalleled data accuracy. For high-precision wavelength selection the HS-190 scanning monochromator is used. The monochromator is optimized for speed, wavelength accuracy and light throughput. The incidence angle range is 15° – 90° with an accuracy of 0.01°. The spectral range is 193 – 2500 nm (0.5 – 6.4 eV).

RC2 ellipsometer. The spectral range of the dual rotating compensator multichannel ellipsometer RC2 (J. A. Woollam Co Inc.) is 0.73 – 6 eV. The polarization state generator unit (1, see Fig. 4.3) comprises a polarizer, rotating compensator, and the light source – a dual deuterium-halogen lamp. The light beam, after reflection on a sample, passes an analyzer and the second rotating compensator (the polarization state analyzer unit, 2). Then, the beam is spectrally separated by a prism and directed onto two CCD arrays. The first CCD array detects a total of 790 spectral points within the spectral range of 210 – 1000 nm (1.2 – 6 eV), whereas the second array detects another 275 spectral points in the 1000 – 1690 nm (0.73 – 1.2 eV) range.

Data of more than 1000 wavelength can be acquired at the same time. The sample tilt adjustment procedure is done with four-quadrant detector (located within unit 2). The motorized goniometer together with the vertical sample stage (unit 3) enables for automated angle-resolved measurements, where ϑ can be varied from 19° to 90°. The RC2 is equipped with a beam shutter to perform automated DC offset calculations.

IR ellipsometry

The first SE measurements of the ZnMgRE quasicrystals in the middle-IR spectral range of $0.1 - 0.5$ eV were carried out by our group in Trondheim NTNU University (Prof. U. Hunderi laboratory) with the original IR ellipsometer, equipped with the Fourier-transform infrared spectrometer. The light polarization was monitored by rotating polarizer and/or analyzer with stepping motors. The angle of incidence could be varied within the $45° - 85°$ interval.

The measurements performed on the ellipsometer allowed to obtain valuable, but only preliminary $\varepsilon(\omega)$ IR spectra (see Fig. 5.4 and Fig. 5.5), because of a low intensity of IR light sources and poor parameters of optical elements.

IR-VASE ellipsometer. The reliable, high-accuracy $\varepsilon(\omega)$ IR spectra in the spectral range $\sim 0.1 - 0.73$ eV were measured in the Linköping University (Prof. H. Arwin laboratory) on the Fourier-transform variable angle spectroscopic ellipsometer IR-VASE (J. A. Woollam Co Inc.). The system is fully automated, operating in the rotating-polarizer – sample – rotating-compensator – analyzer configuration. The IR radiation is focused by off-axis paraboloid mirrors onto the axis of high-precision theta-2theta goniometer unit with the sample mount. The diameter of the beam at a sample surface is approximately 5 mm with a beam divergence of 3°. To ensure the correct alignment of the sample tilt, the instrument is equipped with an alignment unit, which is composed of a HeNe laser and a four-quadrant detector. The spectral resolution of the ellipsometer is of 4 cm^{-1}. The angle of incidence can be varied between 35° and 90°. The ellipsometer is equipped with DTGS detector, which measures the intensity of the reflected beam at a number of discrete polarizer-compensator-analyzer positions.

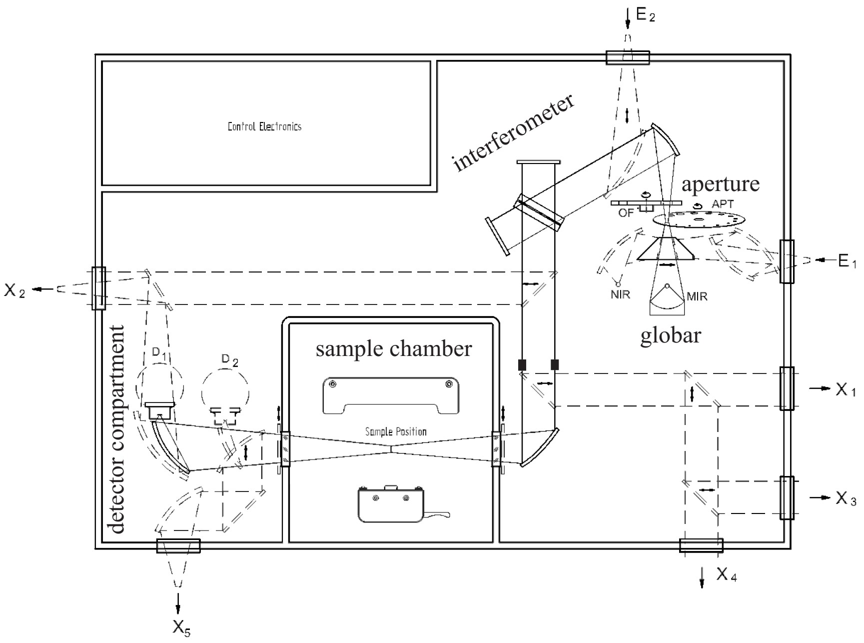

Figure 4.4: Optical layout of the Bruker Vertex 70v Fourier-transform infrared spectrometer

4.2 Reflectance spectroscopy

The optical response of ZnMgRE quasicrystals in the far infrared (FIR) region was examined by the Fourier-transform (FT) reflectance spectroscopy technique.

4.2.1 FT spectrometers

The infrared reflectance spectroscopy measurements were carried out with two different setups: Nicolet 8700 (Fisher Scientific) and Vertex 70v (Bruker Optik GmbH) Fourier-transform spectrometers. An advantage of the Vertex 70v spectrometer is its operation in vacuum ambient, which allowed for an essential reduction of the chamber-gas absorption lines and for a successful measurements of the far-infrared ZnMgRE reflectivity spectra down to about 0.01 eV.

Vertex 70v spectrometer. The optical layout of the spectrometer is shown in Figure 4.4. A globar heated to about 1100 K is used as the spectrometer light source. The light is focused on a circular aperture whose size ranges from 0.25 to 8 mm. Then the light beam is collimated into a 4 cm diameter and sent to the interferometer. The interferometer is equipped with two different beamsplitters: KBr for the middle-IR spectral range 370 – 7500 cm^{-1} (0.05 – 0.93 eV, 27 – 1.3 μm) and Si for the FIR spectral range 50 – 600 cm^{-1} (0.006 – 0.07 eV; 200 – 17 μm). After an interference of the beams at the interferometer exit, the light passes through the sample chamber and reaches the detectors compartment, equipped with two detectors: KBr/DLaTGS for the middle-IR spectral range and PE/DLaTGS for FIR region. The whole optical path is maintained in a vacuum ambient (pressure $\sim 10^{-3}$ bar).

4.3 Anchor-window technique

The normal-incidence reflectance spectroscopy allows for measurements of the reflection coefficient $R(\omega)$, which is a ratio of intensities of the reflected and incident waves, and, therefore, is equal to a squared modulus of the reflection amplitude $r(\omega)$,

$$R(\omega) = \frac{I^r}{I^i}, \quad R(\omega) = |r(\omega)|^2, \quad r(\omega) = \frac{E^r}{E^i}. \tag{4.8}$$

Since the dielectric function $\varepsilon(\omega)$ is a complex quantity, which is related to the reflection amplitude at the normal incidence as (see Fresnel formulas (4.1)–(4.2))

$$r(\omega) = \pm\frac{\varepsilon^{1/2}(\omega) - 1}{\varepsilon^{1/2}(\omega) + 1}, \tag{4.9}$$

a determination of the dielectric function requires for known spectra of both the modulus $|r(\omega)|$, and the phase factor $\delta(\omega)$ of the reflection amplitude $r(\omega) = |r(\omega)| \exp[\mathrm{i}\delta(\omega)]$.

The phase factor of the reflection amplitude can be calculated from the reflectivity spectrum making use of the Kramers–Kronig relation

$$\delta(\omega) = -\frac{\omega}{\pi} P \int_0^\infty \mathrm{d}\omega' \, \frac{\ln R(\omega')}{\omega'^2 - \omega^2}, \tag{4.10}$$

where P denotes the principal part of the integral.

The Kramers–Kronig (KK) transform (4.10) allows for a determination of the complex reflection amplitude $r(\omega)$ and, subsequently, of the dielectric function (see eq. (4.9)) at the known, experimentally measured, reflectivity spectrum $R(\omega)$. However, as seen from (4.10), the Kramers–Kronig analysis requires for the reflectivity spectrum to be defined in the infinite spectral range $\omega \in [0, \infty]$, which can not be achieved in practice.

The low- and high-frequency $R(\omega)$ asymptotic tails should be guessed and added to the experimental $R(\omega)$ spectrum for a calculation of the (4.10) integral. This introduces unavoidable errors to the Kramers–Kronig analysis and a choice of the low- and high-frequency asymptotes, $R_{\text{lf}}(\omega)$ and $R_{\text{hf}}(\omega)$, is a serious, important problem.

In metallic solids, the reflectivity asymptotes are usually approximated by the expressions

$$R_{\text{lf}}(\omega) = 1 - a\sqrt{\omega}, \qquad R_{\text{hf}}(\omega) = \frac{b}{\omega^4}. \tag{4.11}$$

Here the low-frequency asymptote $R_{\text{lf}}(\omega)$ corresponds to the Hagen–Rubens law $R(\omega) = 1 - (2\omega/\pi\sigma_{\text{dc}})^{1/2}$ (where σ_{dc} is the static electric conductivity). The high-frequency asymptote $R_{\text{hf}}(\omega)$ corresponds to a generic frequency dependence, which settles down at photon energies exceeding characteristic energies of a system under investigation, when the dielectric function of the system acquires the $\varepsilon(\omega) = 1 - \omega_{\text{p}}^2/\omega^2$ form.

Results of the Kramers–Kronig analysis of the fci-ZnMgHo reflectivity spectrum, carried out with the standard $R(\omega)$-extrapolations (4.11), are presented by dotted curves in Fig. 4.5. As seen, the Kramers–Kronig transform of the reflectivity spectrum (dots in Fig. 4.5(a)) results in the optical conductivity $\sigma(\omega)$ spectrum (red dotted curves in Fig. 4.5(b)), which essentially differs from the experimental, SE-determined $\sigma(\omega)$ spectrum (dots in Fig. 4.5(b)).

There are various techniques to improve an accuracy of the KK analysis [81]. In the present work we suggested an anchor-window technique [3]*, which is a modification of the known anchor-point method [82].

Within the framework of the suggested anchor-window technique, the high-frequency asymptote is modelled by the inverse polynomial

$$R_{\text{hf}}^{\text{AW}}(\omega) = \left[b_0 + b_1\omega + b_2\omega^2 + b_3\omega^3 + b_4\omega^4\right]^{-1}. \tag{4.12}$$

The coefficients b_i of the polynomial are determined by minimizing a deviation between the KK-deduced optical conductivity $\sigma_{\text{KK}}(\omega)$ and the experimental $\sigma_{\text{exper}}(\omega)$ values, measured a priori by SE-technique in a definite spectral range – the anchor window. The error function to be minimized is chosen in the form

$$\chi = \frac{1}{N_{\text{AW}}} \sum_{n\in\text{AW}} \left| \frac{\sigma_{\text{KK}}[n] - \sigma_{\text{exper}}[n]}{\sigma_{\text{exper}}[n]} \right|^2, \tag{4.13}$$

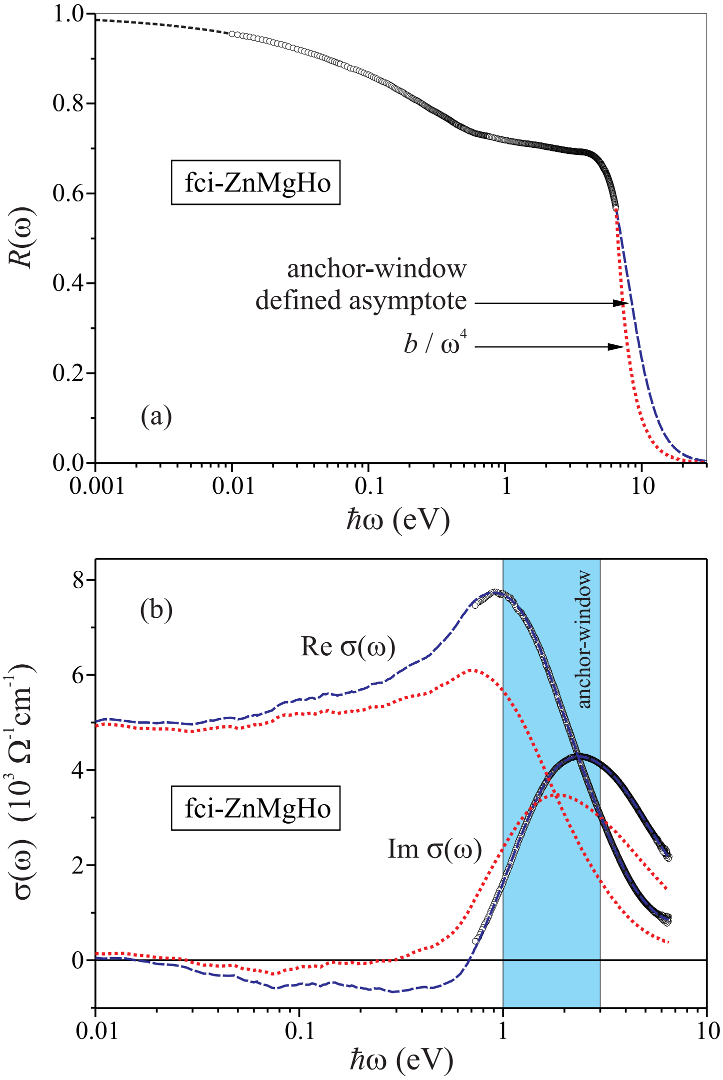

Figure 4.5:

(a) The experimental reflectivity $R(\omega)$ spectrum (dots) and its extrapolations by the standard high frequency asymptote $R_{\mathrm{hf}}(\omega) = b/\omega^4$ (red dotted curve) and by the anchor-window defined asymptote (blue dashed curve).

(b) The experimental optical conductivity $\sigma(\omega)$ spectrum, measured by the spectroscopic ellipsometry technique (dots). Curves present the $\sigma(\omega)$ spectrum determined by the Kramers–Kronig analysis making use of the standard high frequency asymptote $R_{\mathrm{hf}}(\omega) = b/\omega^4$ (red dotted curve) and using the anchor-window defined asymptote (blue dashed curve).

where $\sigma_{\mathrm{exper}}[n]$ is the experimental optical conductivity value at the spectral point n, which belongs to the anchor-window (AW), $\sigma_{\mathrm{KK}}[n]$ is the KK-deduced value, and N_{AW} is the number of spectral points within the anchor-window.

The low-frequency asymptote of the reflectivity spectrum was approximated by the relation

$$R_{\mathrm{lf}}^{\mathrm{AW}}(\omega) = 1 - a_1\sqrt{\omega} - a_2\omega. \tag{4.14}$$

The a_1 and a_2 coefficients were determined by the least-squares technique, minimizing the error function

$$\chi = \frac{1}{N}\sum_{n=1}^{N}\left|R_{\mathrm{lf}}^{\mathrm{AW}}[n] - R_{\mathrm{exper}}[n]\right|^2, \tag{4.15}$$

where $N \sim 10$ is the number of the first spectral points of an experimental reflectivity spectrum.

The high-frequency asymptote $R_{\mathrm{hf}}^{\mathrm{AW}}(\omega)$ of the experimental fci-ZnMgHo reflectivity spectrum, determined by the anchor-window technique, is presented by blue dashed curve in Fig. 4.5(a). Note that $R_{\mathrm{hf}}^{\mathrm{AW}}(\omega)$ does not essentially differ from the standard asymptote, which is determined by eq. (4.11) and is presented in Fig. 4.5(a) by red dotted curve. Nevertheless, the $R_{\mathrm{hf}}^{\mathrm{AW}}(\omega)$ asymptote essentially affects results of Kramers–Kronig analysis – the optical conductivity spectrum $\sigma_{\mathrm{KK}}(\omega)$, deduced by the anchor-window technique (blue dashed curves in Fig. 4.5(b)), actually coincides with the experimental $\sigma(\omega)$ spectrum, measured in NIR-UV range by SE-technique (dots in Fig. 4.5(b)).

The suggested anchor-window technique essentially improves an accuracy of the Kramers–Kronig analysis.

A reliability of the technique was checked [3]* by a comparison of the KK-deduced optical conductivity in the 0.1 – 0.7 eV range with the experimental $\sigma(\omega)$ which was directly measured by the IR spectroscopic ellipsometry technique. The KK-deduced optical conductivity $\sigma_{\mathrm{KK}}(\omega)$ fitted with the experimental spectrum with an accuracy of about 5 %.

4.4 Optical-surface preparation techniques

The zinc-based metallic compounds manifest a high chemical activity with respect to oxygen cohesion, and a preparation of the optical surfaces of both

ZnMgRE quasicrystals, and even the usual crystalline zinc remains to be an unsolved problem.

Freshly prepared optical-surfaces do not show essential changes in optical response of ZnMgRE and/or Zn for approximately 24 hours. Thus, prior to actually each optical measurement, the optical surface should be prepared anew. In the present study several optical-surface preparation techniques have been employed, namely, the mechanical polishing, the chemical etching/polishing, and the plasma etching.

4.4.1 Mechanical polishing

The sample surfaces were mechanically grind and polished with a polycrystalline Struers diamond paste of 10 μm, 6 μm, 1 μm, 0.25 μm, and an alumina suspension of 0.02 μm. The polishing was carried out on the Buehler MiniMet 1000 and the original grinder-polisher. Both allowed to choose the pad rotation velocity and the applied pressure. The motion of the polisher pads was random to prevent a preferential grinding. After the polishing, samples were cleaned in an ethylene ultrasound bath.

The careful, time consuming polishing procedure allowed for an essential increase of the ZnMgRE optical-surface quality. The dielectric function and optical conductivity spectra manifested sharp, essentially increased NIR-UV optical features as compared to results of previous, preliminary optical measurements of our group [83, 69]. The effect is illustrated in Fig. 5.4 and Fig. 5.5 for the fci-ZnMgY spectra.

Nevertheless, the polishing procedure results in a formation of a thin polycrystalline surface layer. This was proved by the SE study of single-grain crystalline Zn samples [11, 17]*. Two samples, with optical surfaces (001) and (110), were prepared. The Zn (001) optical surface was disclosed by a cleavage in a liquid nitrogen bath. The sample with the (110) optical surface was prepared by a diamond saw cutting from an ingot and the mechanical polishing. The multi-angle SE measurements were carried out: SE spectra were recorded at numerous incident $\vartheta \in [25°, 75°]$ and azimuthal $\varphi \in [0°, 360°]$ angles in steps of 10°. The ordinary component $\varepsilon_{\mathrm{o}}(\omega)$ of the Zn dielectric function tensor was determined by the SE analysis of the (001) data. The extraordinary Zn component $\varepsilon_{\mathrm{e}}(\omega)$ and the dielectric function of the surface layer $\varepsilon_{\mathrm{s}}(\omega)$ were determined from the SE data, recorded from the (110) sample. An analysis of the SE data shows that the surface dielectric

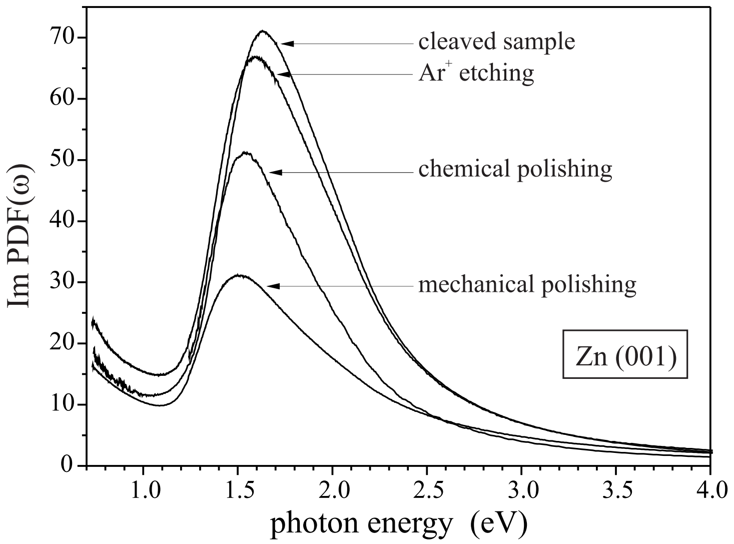

Figure 4.6: Influence of surface preparation on the imaginary part of pseudodielectric function, recorded from Zn (001) surface.

function is close to that of the polycrystalline Zn, $\varepsilon_{\mathrm{s}}(\omega) \sim \frac{2}{3}\varepsilon_{\mathrm{o}}(\omega) + \frac{1}{3}\varepsilon_{\mathrm{e}}(\omega)$.

Independently, a formation of the polycrystalline layer on the polished optical-surface was indirectly proved by polishing a cleaved Zn (001) sample. This resulted in an essential decrease of the Zn optical feature positioned at about 1.7 eV (see Fig. 4.6). Since the 1.7 eV absorption peak is due to the interband transitions across the (101) pseudogap and its spectral weight theoretically is twice lower in the extraordinary component $\varepsilon_{\mathrm{e}}(\omega)$ spectrum as compared to spectrum of the ordinary component [84, 85], the reduction of the 1.7 eV peak indicates to a formation of the polycrystalline layer on the mechanically polished surface.

4.4.2 Chemical etching/polishing

To remove the mechanical polishing induced polycrystalline surface layer various chemical/electrochemical etching/polishing techniques have been tested. The best results were obtained by the following chemical polishing procedure:

- 1 – 2 min exposition in the polishing solution $\mathrm{CrO_3 : Na_2SO_4 : HNO_3 : H_2O}$ (60 : 8 : 10 : 30),
- rinsing in distilled water,
- rinsing (3 s) in the nitrogen acid $\mathrm{HNO_3 : H_2O_2 : H_2O}$ (1 : 1 : 1),

- rinsing (20 s) in the diluted acid $HNO_3 : H_2O$ (1 : 20),
- rinsing in methanol,
- drying in a nitrogen gas ambient.

The chemical polishing procedure allowed for an increase of the interband absorption peak up to 70 % of the initial peak intensity, observed from the cleaved surface (Fig. 4.6).

However, although the chemical polishing is effective, it introduces a grid of small etching pits on the sample, which was visible in an ordinary optical micrographs.

4.4.3 Plasma etching

The most effective final optical-surface preparation technique proved to be the plasma etching of the surface in an UHV chamber. It resulted in the Zn (001) optical surface, the quality of which was close to that of the cleaved sample (see Fig. 4.6). The interband absorption peak intensity was below that of the cleaved surface by only 5 – 6 %.

The Ar^+ ion $E = 1$ keV sputtering was carried out in the UHV chamber of the XPS spectrometer VG Scientific ESCALAB MK II, the vacuum level in which can be maintained at the 10^{-9} mbar level. During the etching, the exposition time of which was ≈ 40 min and the pressure of Ar gas was about 10^{-6} mbar, the sample was rotated to avoid a preferential etching of its surface.

The same plasma etching procedure was applied for a final optical-surface preparation of ZnMgRE quasicrystals. It allowed us to increase the ZnMgRE optical features by about 10 %. This is illustrated in Fig. 4.7 for the fci-ZnMgHo quasicrystal. In quasicrystals, the relative increase in the spectral weight of the interband absorption is smaller as compared to that for the monocrystalline zinc, because the icosahedral quasicrystals are optically isotropic. A difference in optical response of the poly-quasicrystalline and single-grain QC samples most probably is due to a difference of relaxation times or broadening parameters of electronic subsystem.

4.5 Surface oxide layers

Surface oxide layers of fci-ZnMgRE (RE = Y, Er) quasicrystals in the present work were examined by the X-ray photoemission spectroscopy (XPS)

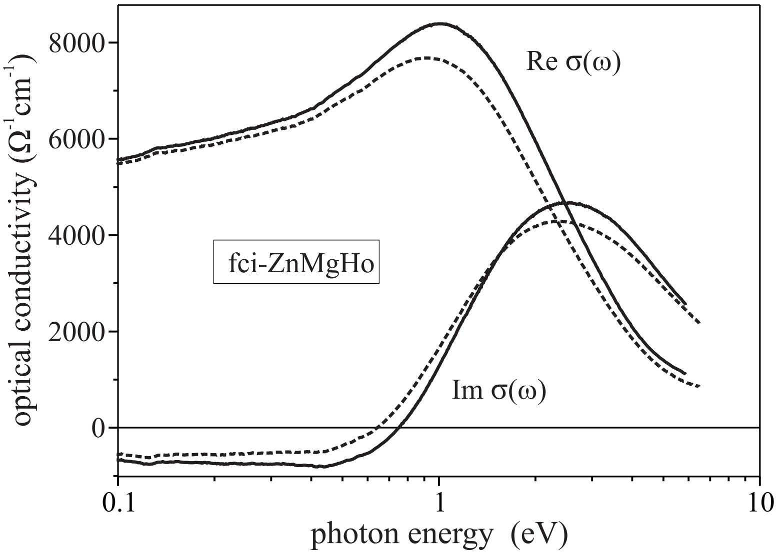

Figure 4.7: Influence of the Ar^+-etching on the fci-ZnMgHo optical conductivity spectrum. Full and dashed curves present data recorded after and before the sputtering, respectively.

technique. The measurements were carried out by PHI VersaProbe II spectrometer (Physical Electronics, Chanhassen MN) equipped with Al K_α (1.487 eV) X-ray source.

The fci-ZnMgY and fci-ZnMgEr photoemission spectra were recorded while sputtering the samples with 1 keV Ar^+ ion beam. This allowed for a determination of the depth profiles of atomic composition in surface layers (Fig. 4.8). The relative atomic concentrations were determined by analyzing the intensity ratios of PE lines of the O 1s, C 1s, Zn $2p_{3/2}$, Mg 1s, and Y 3d (Er 4d) core-levels. The section depth z was determined by calibrating the etching rate with respect to the reference SiO_2 etching-rate (4 mm/min).

The determined widthes of the surface layers on ZnMgY and ZnMgEr samples, which were exposed to atmospheric ambient for, respectively, ~ 2 and ~ 1 years, are of 240 nm and 60 nm. The 240 nm estimate of the ZnMgY surface-layer width is confirmed by results of EDX measurements (Institute of Chemistry), which yielded $d = 200 \pm 20$ nm. The high values of ZnMgRE surface-layer thicknesses distinguish the ZnMgRE quasicrystals from the Al-based ones. An oxidation of Al-based quasicrystals results in a formation of a thin, passivating aluminum oxide layer of the order of 1 – 10 nm, which subsequently gives rise to a high oxidation resistance of a material, as determined for AlCuFe and AlPdMn QCs, the surface layers of

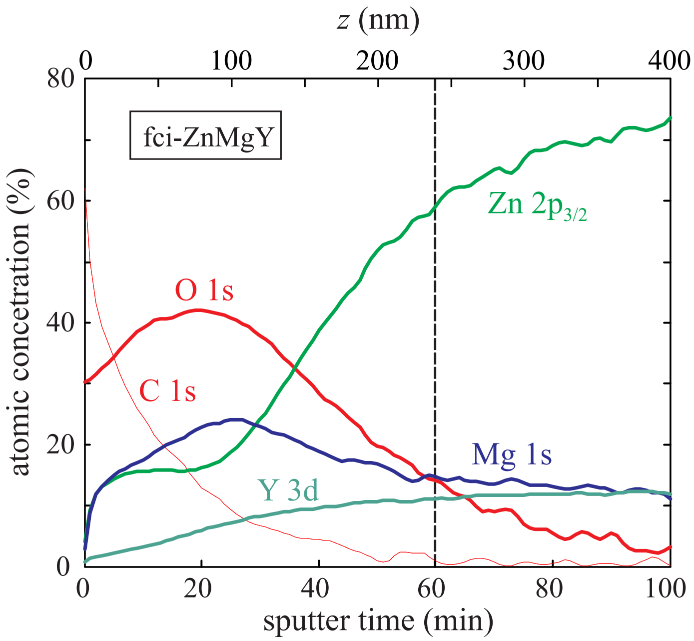

Figure 4.8: The depth profiles of atomic composition in the fci-ZnMgY surface layer.

which are most widely investigated (see, e. g., [86, 87, 88] for reviews). In ZnMgRE quasicrystals exposed to an atmospheric ambient, the passivating layers do not form and the ZnMgRE oxide layers continually grow up to ~ 100 nm.[1]

The depth profiles of atomic composition show that the ZnMgRE surface layers are not uniform (Fig. 4.8). They start with the outer oxide layer, the relative concentration of oxygen in which is of about 50 %. In the inner part of the surface layer, the oxygen concentration gradually decreases.

An analysis of the chemical shifts of atomic core-levels allows for a determination of an oxidation type. Figure 4.9 shows a variation of the O 1s photoemission line in the fci-ZnMgY surface layer. As seen, in the outer part of the layer an oxygen is bind preferentially with zinc, while in the inner part a cohesion of oxygen with magnesium and yttrium is dominating.

---

[1] The determined estimate of the ZnMgRE surface layer thickness of ~ 100 nm is in accord with results of previous SE studies of fci-ZnMgY and fci-ZnMgHo surface layers [78, 79].

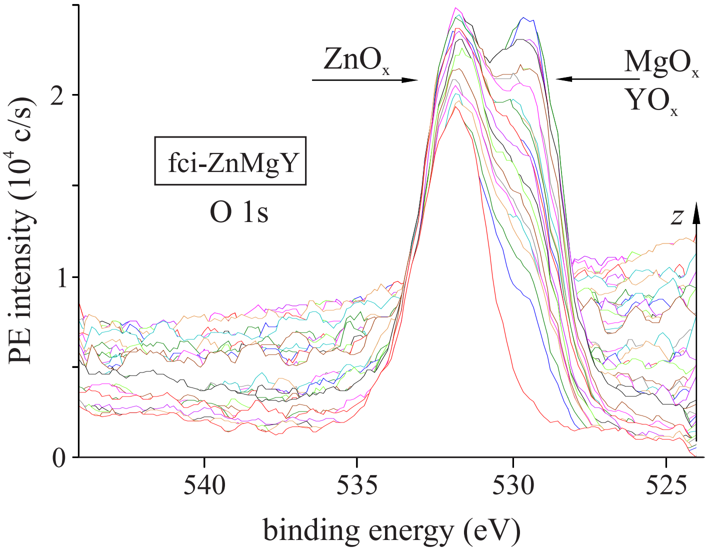

Figure 4.9: Photoemission spectra of the O 1s core-level in the fci-ZnMgY surface layer.

4.6 Resumé

The wide spectral range optical studies of ZnMgRE quasicrystals were carried out by a combined spectroscopic ellipsometry and reflectance spectroscopy technique.

The anchor-window method of the reflectivity spectra analysis was suggested, which essentially improves an accuracy of the dielectric function and/or optical conductivity determination by the Kramers–Kronig transform.

The combined mechanical polishing and plasma-etching technique of the ZnMgRE optical-surface preparation was worked out.

The surface oxide layers on the ZnMgRE quasicrystals continually grow in atmospheric ambient reaching the thicknesses of the order of 100 nm. The surface layers are not homogeneous, in their inner part prevails an oxygen cohesion with Mg, while in the outer part of the layers the oxygen atoms are bind mostly to zinc.

Chapter 5

ZnMgRE optical response

The optical response of quasicrystals, as of other metallic compounds, is determined by the intraband, Drude-type, and the interband optical transitions. However, if in the usual metals the Drude contribution is dominating and optical features due to the interband optical transitions are comparatively small (see, e. g., the optical conductivity spectrum of zinc in Fig. 5.1), in quasicrystals the ratio of the contributions is reversed.

Optical studies of icosahedral AlMn [89], AlCuFe [90], AlCuFeB [91], AlPdMn [92, 93, 91], AlPdRe [94, 95, 96], and AlMnSi [97] quasicrystals revealed the main features of their optical spectra to be the broad absorption peak at about 1–2 eV and a strong suppression of the Drude-type optical transitions (Fig. 5.2(a)). Investigations of decagonal quasicrystalline AlCoCu [98], AlCoCuSi [98], and AlNiCo [39] phases show an essential reduction of the Drude-type response in the plane of quasicrystalline atomic arrangement as compared to an optical response in the periodic, crystalline, direction.

The preliminary spectroscopic ellipsometry studies of i-ZnMgRE quasicrystals, carried out by our group [83, 99], [1]*, as well as Chernikov et al. reflectance spectroscopy study [100] of ZnMgY and ZnMgTb, indicated comparable contributions of the intraband, Drude-type, and interband optical transitions (Fig. 5.2(b)). This was later confirmed by our detailed ZnMgRE optical studies [2, 4, 5]*.

The distinctive feature of the ZnMgRE quasicrystals with respect to most other quasicrystalline compounds is the fact that the ZnMgRE valence bands are predominantly due to the sp-type electron states, as was revealed by photoemission spectra measurements [68, 69, 70]. The valence bands

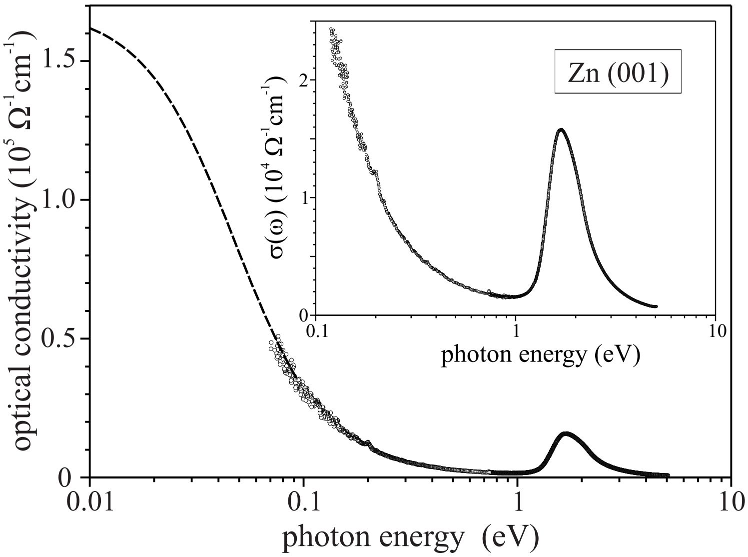

Figure 5.1: Optical conductivity spectrum of monocrystalline zinc. Dashed curve presents the Drude contribution, inset shows a scaled intraband absorption peak.

of Al-based quasicrystals are dominated by d-electrons of transition metals (e. g., of copper and iron in AlCuFe, and of palladium and manganese in AlPdMn). In this respect, the ZnMgRE quasicrystals are closer to the simple, sp-type, metals, while most other QCs are cognates of transition metals. This can be one of the reasons of a comparatively higher Drude contribution in ZnMgRE.

Theoretical description of an optical response of quasicrystals requires for a choice of the QC electronic structure model (Chapter 3). When calculations of the optical response are carried out within the framework of the first principles approach, the theory predicts the spiky optical spectra [101], as is illustrated in Fig. 5.3(a). The experimental optical studies of quasicrystals and calculations based on the band structure hypothesis do not show the predicted spikiness (Fig. 5.2 and Fig. 5.3).

Although the band structure hypothesis predicts the optical response of quasicrystals, which seems to be much closer to experimental data, than that predicted by the first principles approach, one should keep in mind that, strictly speaking, experimentally one can not distinguish a relevance of the two electronic structure models. Indeed, as has been shown by Fujiwara et al. [101], an intrinsic broadening of the electron states by the broadening parameter $\Gamma = 0.7$ eV should completely wash out a spikiness of optical

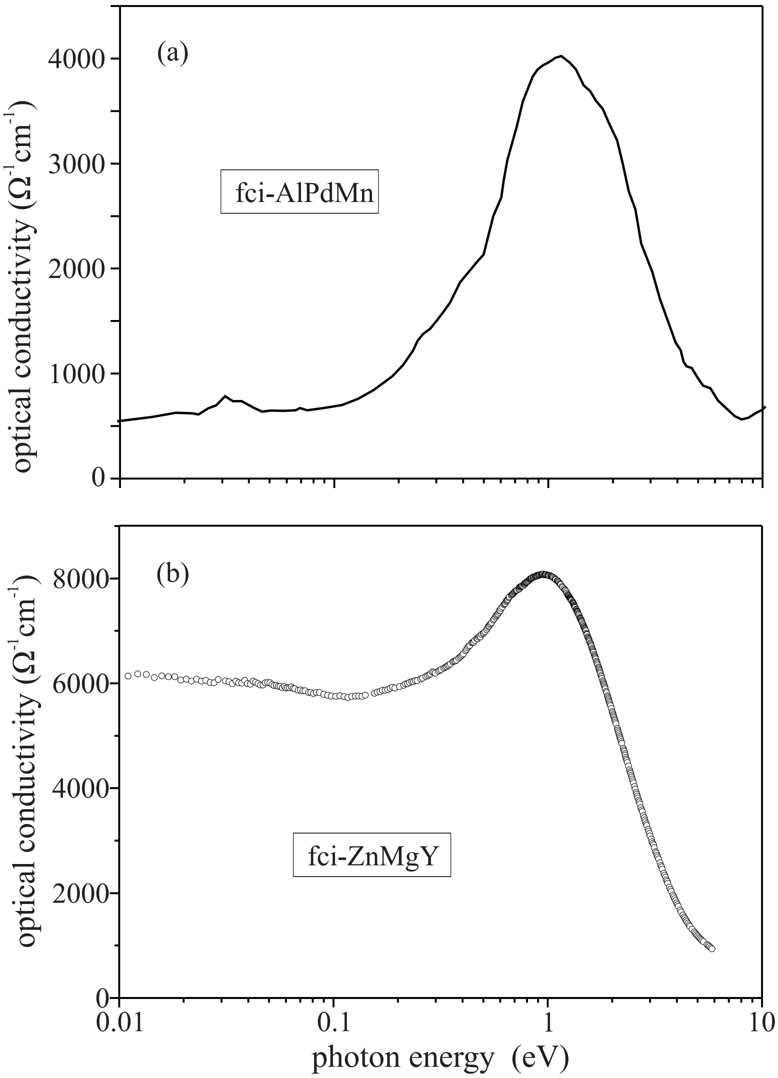

Figure 5.2: Optical conductivity spectra of (a) AlPdMn [93] and (b) ZnMgY [5]* quasicrystals.

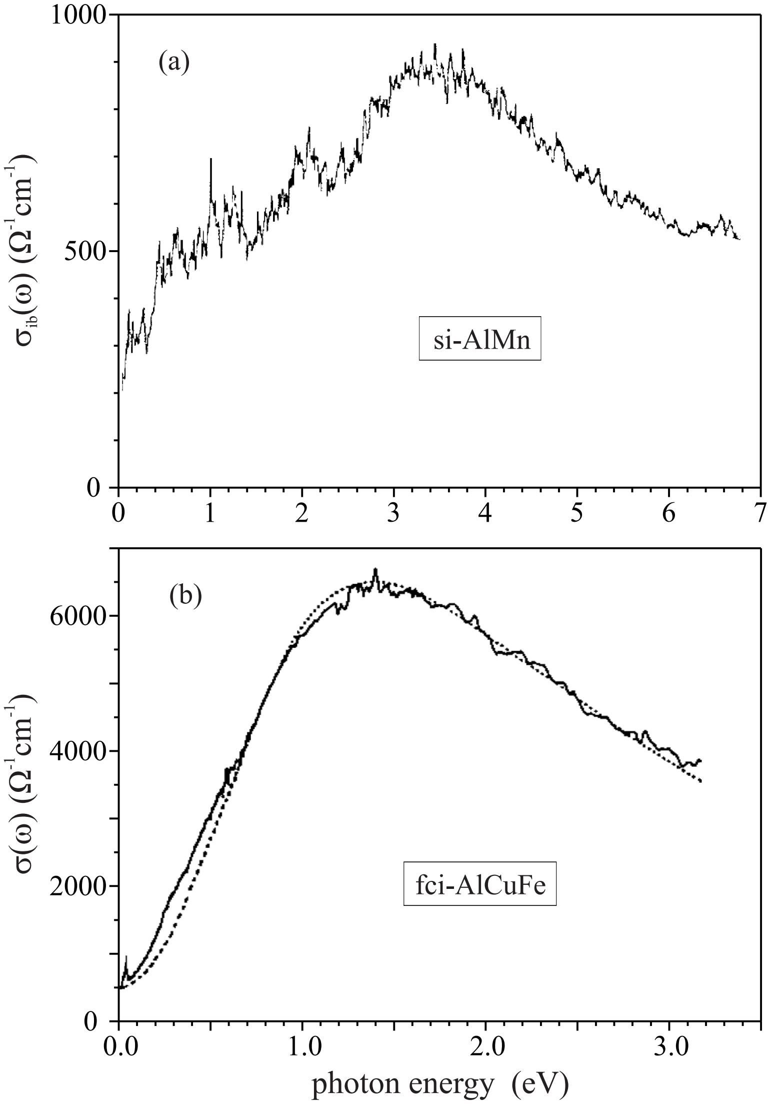

Figure 5.3: (a) Theoretical interband optical conductivity of AlMn, calculated by Fujiwara et al. (adapted from [101]) within the first principles approach. (b) The experimental AlCuFe optical conductivity spectrum (full curve, Homes et al. [90]) and its theoretical description (dotted curve, Burkov et al. [102]) within the band structure hypothesis approach.

spectra. Since the relaxation times in all known quasicrystals are short and correspond to $\Gamma = \hbar/\tau \sim 0.1-1$ eV, the spikiness can be hidden by the finite broadening parameters.

Hereafter in this chapter we will present a short overview of the experimental ZnMgRE optical spectra (§ 5.1), which constitute a basis of the dissertation. In section § 5.2, a scheme of theoretical optical conductivity calculations will be developed. Finally, in section § 5.3, we will present detailed analysis of the experimental ZnMgRE optical spectra based on the developed theoretical scheme.

5.1 ZnMgRE optical spectra

The first optical investigations of the ZnMgRE optical response were carried out by our group on the single-grain and poly-quasicrystalline fci-ZnMgY samples by the rotating-analyzer ellipsometer RAE in the spectral NIR-UV range $1-4.7$ eV [103], which was later expanded to the $0.6-4.7$ eV window [104, 83]. The middle-infrared optical response in the $0.1-0.5$ eV spectral range was examined by the original Fourier-transform ellipsometer (at Trondheim NTNU University) first on the poly-QC [104, 83], then on the single-grain fci-ZnMgY samples [69]. Later the measurements were repeated for the fci-ZnMgEr [69, 99] and fci-ZnMgHo samples [1]*. The recorded optical spectra indicated both the Drude-intraband, and interband optical features, however their detailed analysis was impossible due to an essential scatter of the middle-IR data and its poor overlap with the NIR-UV spectra.

In the first optical studies of fci-ZnMgY, an optical anisotropy of the single-grain sample was detected [103]. However, soon it was understood that the anisotropy is induced by the surface oxide layers, which essentially affect optical spectra of ZnMgRE quasicrystals [78, 79].

Optical response of the ZnMgRE quasicrystals, after a careful mechanical preparation of their optical surfaces (§ 4.4), does not depend on an orientation with respect to icosahedral axes. No changes in ZnMgRE optical spectra are observed, when the spectra are recorded from the C_5, C_3, or C_2 surfaces. The quasicrystals are optically isotropic, as it is predicted by their point symmetry group.

An essential breakthrough in ZnMgRE optical studies was achieved in the present work by the IR spectroscopic ellipsometry measurements car-

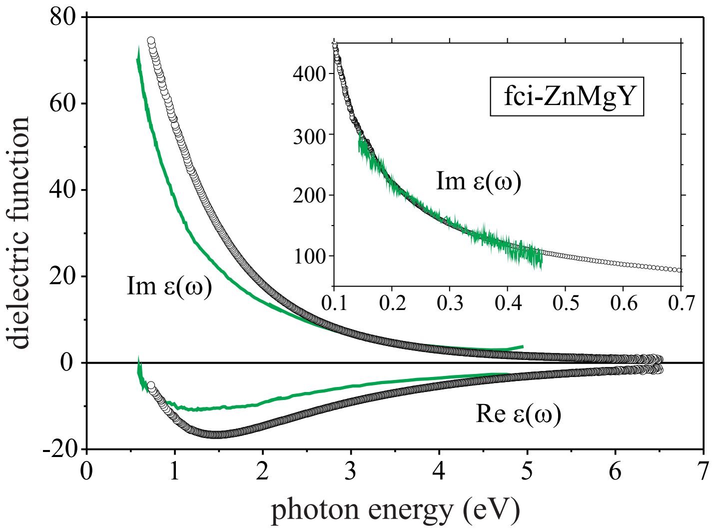

Figure 5.4: Experimental spectra of the fci-ZnMgY dielectric function in the NIR-UV and IR (inset) spectral regions. Dots correspond to [4]* data. Full curves present old results [83, 69].

ried out with the Fourier-transform IR-VASE ellipsometer (J. A. Woolam Co, Inc.). The measurements, combined with those by a conventional spectroscopic ellipsometry IR-UV technique, allowed to record the reliable, well-reproducible optical spectra in the spectral range of 0.15 – 6.5 eV. The dielectric function $\varepsilon(\omega)$ spectra of si-ZnMgHo [2]* and fci-ZnMgRE (RE = Y, Ho, Er) [4]* quasicrystals were recorded. The optical spectra of all four investigated quasicrystals are similar, as one can expect keeping in mind that the atomic concentrations of Zn and Mg are similar in the QCs, while the atomic concentration of the rare earth element is comparatively low, ~ 10 % (see Table 1.1).

A comparison of the measured fci-ZnMgY dielectric function with the old data is presented in Fig. 5.4. The dielectric function $\varepsilon(\omega)$ of metallic solids infinitely increases in the low-frequency limit, and their optical response is convenient to analyse in terms of the optical conductivity $\sigma(\omega)$, related to the dielectric function as

$$\varepsilon(\omega) = 1 + \mathrm{i}\frac{4\pi}{\omega}\,\sigma(\omega). \tag{5.1}$$

The optical conductivity spectrum of fci-ZnMgY is presented in Fig. 5.5, where, for a comparison, the results of old measurements [83, 69] are presented as well. An increase of the optical feature at about 1 eV was achieved by a careful mechanical optical-surface preparation procedure. As seen from

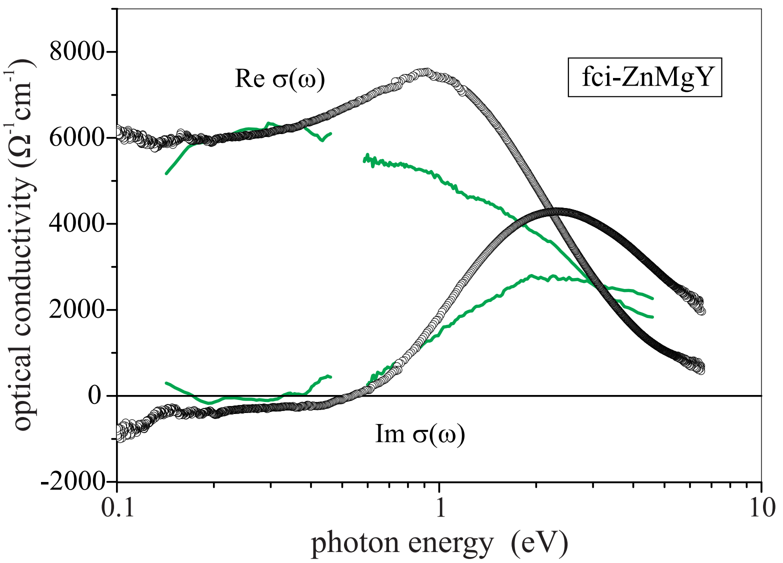

Figure 5.5: Optical conductivity spectra of the fci-ZnMgY quasicrystal. Dots correspond to [4]* data. Full curves present old results [83, 69].

Figs. 5.4 – 5.5, the optical conductivity spectrum distinctly shows the optical feature at about 1 eV, related with the interband optical transitions, while in the $\varepsilon(\omega)$ spectrum, due to a steep increase of the imaginary part of $\varepsilon(\omega)$ at low frequencies, the feature can be only indirectly traced in the real part of $\varepsilon(\omega)$ spectrum.

The next important step in collecting ZnMgRE optical data was done by employing the Fourier-transform FIR reflectance spectroscopy (§ 4.2) and the suggested anchor-window technique of the FIR data analysis (§ 4.3), which allowed for an expansion of the $\varepsilon(\omega)$ and $\sigma(\omega)$ spectral window to the 0.01 – 6 eV range [5]*. Additionally, the optical features in the recorded IR-UV SE spectra were increased by using the new optical-surface-preparation plasma-etching technique (§ 4.4). The recorded wide-range fci-ZnMgY dielectric function spectrum is presented in Fig. 5.6.

The optical response of ZnMgRE quasicrystals was investigated, apart from our group, by Chernikov et al. group of Zürich and Iowa Universities [100], who measured the fci-ZnMgY and fci-ZnMgTb reflectivity spectra $R(\omega)$ in the wide, 0.001 – 10 eV, spectral range. A comparison of our $R(\omega)$ spectrum with that of Chernikov et al. is presented in Fig. 5.7. As seen, the spectra are similar in the FIR region, however, our measurements show a higher reflectance in the VIS-UV range. The discrepancy, most probably, is due either to different optical-surface-preparation techniques used, or to

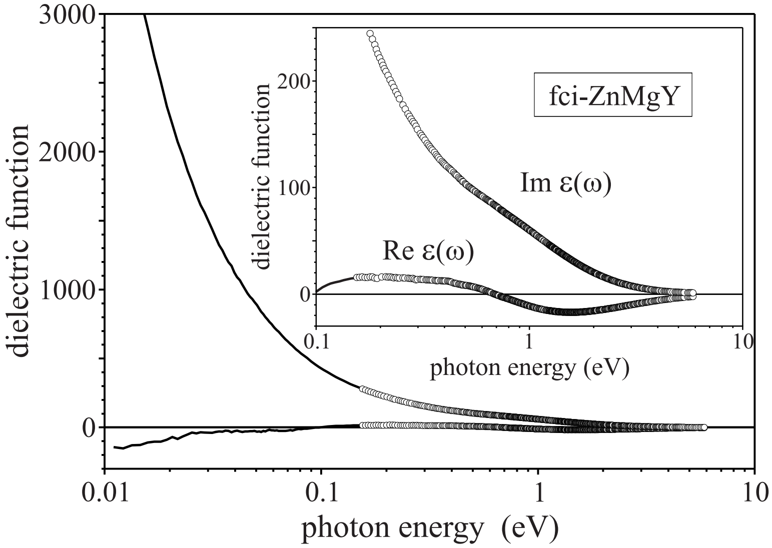

Figure 5.6: The wide spectral range dielectric function of fci-ZnMgY quasicrystal [5]*. (Dots present the spectroscopic ellipsometry data, curves correspond to $\varepsilon(\omega)$ deduced from the FIR reflectance spectroscopy data.)

different structural qualities of the investigated samples. The first assumption is supported by the fact that Chernikov et al. $R(\omega)$ spectrum is close to the old $R(\omega)$ data of our group [83], recorded on samples with lower quality optical-surface. The second assumption stems from XRD studies – the fci-ZnMgY quasicrystals, grown in Frankfurt am Main (Assmus group), manifest Bragg peaks with very large, $g_{\perp}a = 23.9$, complementary reciprocal lattice vectors (§ 2.2.2), while the fci-ZnMgY quasicrystals, grown in Iowa University (Canfield group), manifest $g_{\perp}a = 17.3$ peaks [57].

In Fig. 5.8, the fci-ZnMgRE optical conductivity spectrum, which corresponds to the dielectric function presented in Fig. 5.6, is compared with Chernikov et al. $\mathrm{Re}\,\sigma(\omega)$ spectrum, which was determined from $R(\omega)$ data by the Kramers–Kronig (KK) transform. Again, a difference in spectra is more pronounced in the VIS-UV region, what now can be additionally due to unavoidable errors of the KK procedure. Reliability of our data in the $0.1-6$ eV range is justified by the used SE measurement technique, which allows for a direct determination of the $\varepsilon(\omega)$ and $\sigma(\omega)$ spectra in the IR-UV range.

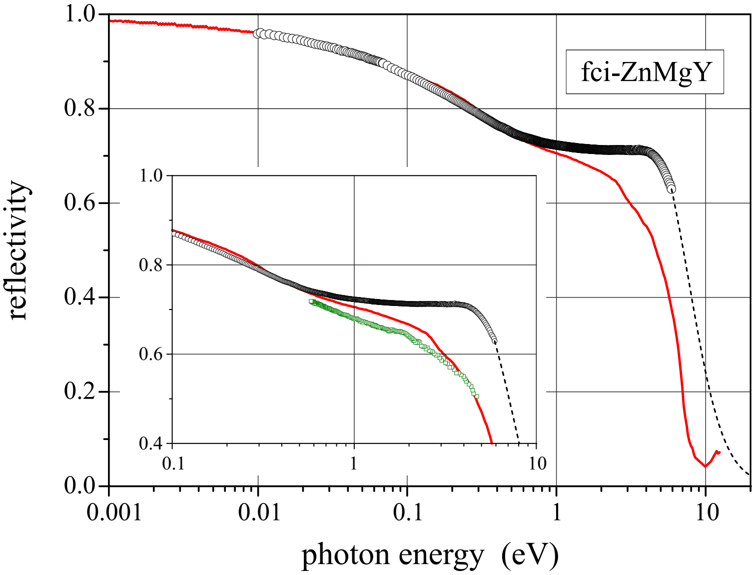

Figure 5.7: Reflectivity spectrum of fci-ZnMgY quasicrystal. Circular dots present our data [5]*, squared dots (in inset) correspond to old data of our group [83], full curve presents Chernikov et al. results [100], and dashed curve corresponds to the high-frequency asymptote used in Kramers–Kronig analysis.

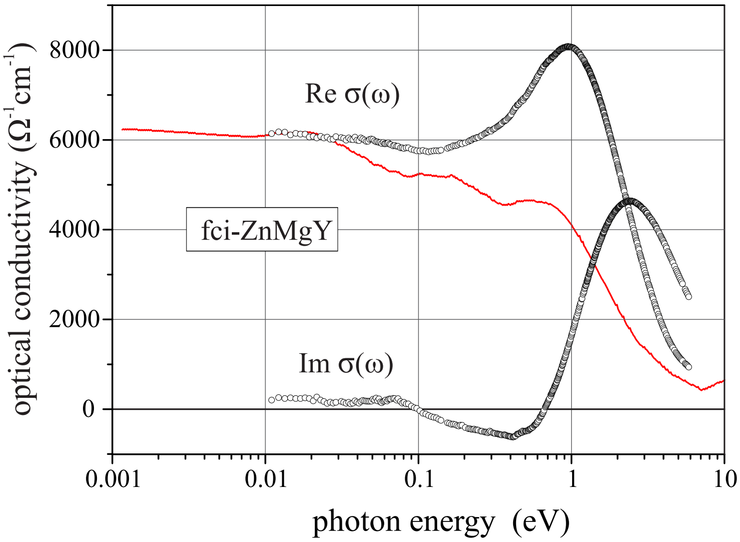

Figure 5.8: Comparison of the fci-ZnMgY optical conductivity spectrum ([5]*, dots) with the Re $\sigma(\omega)$ spectrum deduced by Chernikov et al. [100] (curve).

5.2 Optical conductivity. Theory

The optical conductivity of metallic solids is determined by the intraband, Drude type, and the interband transitions of the valence electrons. Both terms of the optical conductivity, $\sigma_{\mathrm{Drude}}(\omega)$ and $\sigma_{\mathrm{ib}}(\omega)$, can be calculated following the Ashcroft and Sturm algorithm [105], which was worked out for the usual crystalline metals, and later was successfully applied for an analysis of the fci-AlCuFe optical response [102]. The Ashcroft and Sturm calculations were carried out in the reduced zone presentation. Since the reduction of electron states to the Brillouin zone is based on the Bloch theorem and, therefore, can not be strictly justified for quasicrystals, we repeated the optical conductivity calculations in the extended zone scheme. The main difference in the reduced- and extended-zone presentations is the selection rule for optical transitions. Within the reduced zone scheme, the transitions are vertical, $\boldsymbol{k}' = \boldsymbol{k}$, while within the extended zone presentation the transitions are indirect – the final quasimomentum is shifted by the reciprocal lattice vector, $\boldsymbol{k}' = \boldsymbol{k} - \boldsymbol{g}$. Nevertheless, as can be expected, calculations in both presentations lead to the same final results for $\sigma(\omega)$.

The Ashcroft and Sturm $\sigma(\omega)$ formulas were derived for polyvalent metals, the Fermi level in which is positioned above a pseudogap. In the present section (§ 5.2.1 – § 5.2.2) we will develop the Ashcroft and Sturm theoretical scheme of $\sigma(\omega)$ calculations by deriving formulas appropriate to the cases, when the Fermi level is positioned within a pseudogap and below it.

5.2.1 Drude optical conductivity

The intraband polarization of electrons in metals leads to the optical conductivity of the Drude form

$$\sigma_{\mathrm{Drude}}(\omega) = \frac{\sigma_{\mathrm{dc}}}{1 - \mathrm{i}\omega\tau}, \tag{5.2}$$

where σ_{dc} is the static electric conductivity and τ is the relaxation time. For the free electron gas, the static conductivity is given by the well known formula $\sigma_{\mathrm{dc}} = e^2 n\tau/m_0$, where n is the electron concentration and m_0 is the free electron mass. When electron gas is affected by the atomic-lattice potential field, the σ_{dc} formula should be modified – the m_0 mass should be replaced by the optical mass m_{opt} [106]. Indeed, in the framework of the

Drude kinetic model, the static conductivity is defined as (see, e. g., [73])

$$\sigma_{\mathrm{dc}} = \frac{e^2\tau}{4\pi^3}\int \mathrm{d}^3k\,\boldsymbol{v}_{\boldsymbol{k}}^2\left(-\frac{\partial f_{\boldsymbol{k}}}{\partial\varepsilon(\boldsymbol{k})}\right), \tag{5.3}$$

where $f_{\boldsymbol{k}}$ is the Fermi distribution, $\boldsymbol{v}_{\boldsymbol{k}} = \hbar^{-1}\nabla_{\boldsymbol{k}}\varepsilon(\boldsymbol{k})$ is the electron group velocity, and $\nabla_{\boldsymbol{k}}$ is the gradient over $\boldsymbol{k}$ operator, $\nabla_{\boldsymbol{k}} = \partial/\partial\boldsymbol{k}$. Taking the integral (5.3) in parts, one obtains the following formulas for σ_{dc} and the optical mass:

$$\sigma_{\mathrm{dc}} = \frac{e^2 n\tau}{m_{\mathrm{opt}}}, \qquad \frac{1}{m_{\mathrm{opt}}} = \frac{1}{4\pi^3 n}\int \mathrm{d}^3k\, f_{\boldsymbol{k}}\,\frac{1}{3\hbar^2}\nabla_{\boldsymbol{k}}^2\varepsilon(\boldsymbol{k}), \tag{5.4}$$

In the reduced zone presentation, the optical mass formula takes the form

$$\frac{1}{m_{\mathrm{opt}}} = \frac{1}{4\pi^3 n}\sum_n \int_{(\mathrm{BZ})} \mathrm{d}^3k\, f_{n\boldsymbol{k}}\,\frac{1}{3\hbar^2}\nabla_{\boldsymbol{k}}^2\varepsilon_n(\boldsymbol{k}). \tag{5.5}$$

In the extended zone presentation, to find the optical mass (5.4) we use the energy spectrum formula (3.20). Straightforward calculations of the $\nabla_{\boldsymbol{k}}^2$ action on $\varepsilon(\boldsymbol{k})$ result in the following expression:

$$\frac{1}{3\hbar^2}\nabla_{\boldsymbol{k}}^2\varepsilon(\boldsymbol{k}) = \frac{1}{m_0} - \frac{1}{3m_0}\sum_{\boldsymbol{g}\in\mathcal{G}}\frac{\gamma}{|\gamma|}\frac{4\varepsilon_0}{\Delta_{\boldsymbol{g}}}\frac{1}{(\gamma^2+1)^{3/2}}. \tag{5.6}$$

When this intermediate result is inserted into an inverse optical mass formula (5.4), an integration over $\boldsymbol{k}$-space of the first (5.6) term yields an inverse free-electron mass m_0^{-1}. The second term corresponds to the m_0^{-1} corrections, which are due to distortions of the free electron energy spectrum by intersections with the $\boldsymbol{g}\in\mathcal{G}$ Bragg planes. An integration over $\boldsymbol{k}$ for each separate distortion can be conveniently carried out in a cylindric coordinate system, $\mathrm{d}^3k = \mathrm{d}\varphi\,\mathrm{d}k_{\|}\,k_{\perp}\mathrm{d}k_{\perp}$, with the polar axis directed along $\boldsymbol{g}$-vector. Since the partial distortions depend on $k_{\|}$ only, an integration over $k_{\perp}$ involves the Fermi distribution function only and can be carried out separately. The integral can be presented as the dimensionless function

$$S(k_{\|}) = \frac{\gamma}{|\gamma|}\frac{\hbar^2}{m_0}\int_0^{\infty}\mathrm{d}k_{\perp}k_{\perp}\, f_{\boldsymbol{k}}, \tag{5.7}$$

which depends on $k_{\|}$. Then, the inverse optical mass formula (5.4) can be presented in the following final form:

$$\frac{1}{m_{\mathrm{opt}}} = \frac{1}{m_0}\left[1 - \sum_{\boldsymbol{g}\in\mathcal{G}}\frac{m_0 g\Delta_{\boldsymbol{g}}}{24\pi n\hbar^2}\,C\right], \tag{5.8}$$

$$C = \frac{2}{\pi}\int_1^{x_1} \frac{\mathrm{d}x\, S(x)}{x^2\sqrt{x^2-1}}. \tag{5.9}$$

Here the integration variable $k_{\|}$ was replaced by $x = \sqrt{\gamma^2+1}$. The upper limit of x-integration, x_1, is determined by the S-function (5.7).

The S-function can be calculated analytically. It acquires different expressions depending on a relative position of the Fermi level with respect to a pseudogap:

(i) The Fermi level below a pseudogap, $\varepsilon_\mathrm{F} < \varepsilon_0 - \frac{1}{2}\Delta_{\boldsymbol{g}}$,

$$S(x) = \begin{cases} 0, & 1 < x < x_0, \\ \dfrac{(x-x_0)(x_1-x)}{2(x_0+x_1)}, & x_0 < x < x_1. \end{cases} \tag{5.10}$$

(ii) The Fermi level within a pseudogap, $\varepsilon_0 - \frac{1}{2}\Delta_{\boldsymbol{g}} < \varepsilon_\mathrm{F} < \varepsilon_0 + \frac{1}{2}\Delta_{\boldsymbol{g}}$,

$$S(x) = \frac{(x-x_0)(x_1-x)}{2(x_0+x_1)}, \qquad 1 < x < x_1. \tag{5.11}$$

(iii) The Fermi level above a pseudogap, $\varepsilon_\mathrm{F} > \varepsilon_0 + \frac{1}{2}\Delta_{\boldsymbol{g}}$,

$$S(x) = \begin{cases} x, & 1 < x < |x_0|, \\ \dfrac{(x-x_0)(x_1-x)}{2(x_0+x_1)}, & |x_0| < x < x_1. \end{cases} \tag{5.12}$$

The x_0 and x_1 parameters in formulas (5.10)–(5.12) are defined by the expressions

$$x_0 = \frac{4\varepsilon_0}{\Delta_{\boldsymbol{g}}}\left[1 - \sqrt{\frac{\varepsilon_\mathrm{F}}{\varepsilon_0} + \left(\frac{\Delta_{\boldsymbol{g}}}{4\varepsilon_0}\right)^2}\,\right], \tag{5.13}$$

$$x_1 = \frac{4\varepsilon_0}{\Delta_{\boldsymbol{g}}}\left[1 + \sqrt{\frac{\varepsilon_\mathrm{F}}{\varepsilon_0} + \left(\frac{\Delta_{\boldsymbol{g}}}{4\varepsilon_0}\right)^2}\,\right], \tag{5.14}$$

where ε_F is the Fermi energy, $\varepsilon_0 = \hbar^2(\frac{1}{2}g)^2/2m_0$ is the intersection energy with the Bragg $\boldsymbol{g}$-plane, and $\Delta_{\boldsymbol{g}}$ is the pseudogap width.

Making use of the S-function expressions (5.10)–(5.12), one can perform straightforward calculations of the C-coefficient (5.9). Figure 5.9 presents a dependence of the coefficient on a position of a pseudogap with respect to the Fermi level at several given pseudogap values, $\Delta_{\boldsymbol{g}}/\varepsilon_\mathrm{F} = 0.2$, 0.1, and 0.05. (Dashed curves in the figure present the dependence of $\sqrt{\varepsilon_0/\varepsilon_\mathrm{F}}\,C$ on $\varepsilon_0/\varepsilon_\mathrm{F}$, which takes into account a variation of the g parameter in the

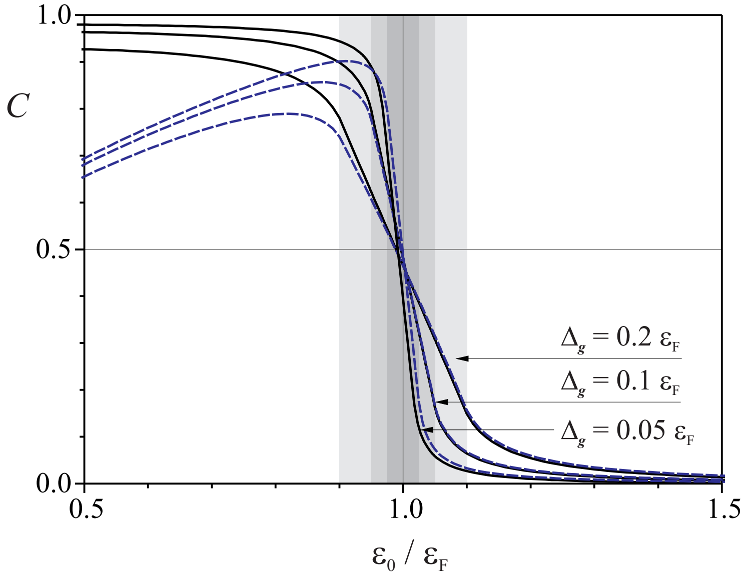

Figure 5.9: Dependence of the C-coefficient on a position of pseudogap with respect to the Fermi level (full curves). Dashed curves present the dependence of $\sqrt{\varepsilon_0/\varepsilon_\mathrm{F}}\,C$ on $\varepsilon_0/\varepsilon_\mathrm{F}$.

optical mass formula (5.8).) As seen, C-coefficient quickly drops down, when a pseudogap shifts above the Fermi level, in accord with the general assertion that a decisive role in the electron energy spectrum problem is played by the Bragg planes in a vicinity of the Fermi surface.

In the usual crystalline metals, the optical mass m_opt is close to the free electron one, m_0. The prove that, one can rewrite the m_opt formula (5.8) in an approximate form

$$\frac{1}{m_\mathrm{opt}} \sim \frac{1}{m_0}\left[1 - M\frac{\pi}{8}\frac{\Delta_{\boldsymbol{g}}}{\varepsilon_\mathrm{F}}\sqrt{\frac{\varepsilon_0}{\varepsilon_\mathrm{F}}}\,C\right], \qquad (5.15)$$

where M is the multiplicity of Bragg planes. In derivation of (5.15), an approximate relation between the electron concentration and the Fermi energy $n = (3\pi^2)^{-1}(2m_0\varepsilon_\mathrm{F}/\hbar^2)^{3/2}$, which is strictly valid for the free electron gas only, was used. As seen from (5.15), a correction to the inverse optical mass is proportional to a ratio of the pseudogap $\Delta_{\boldsymbol{g}}$ to the Fermi energy, which is a small parameter, $\Delta_{\boldsymbol{g}}/\varepsilon_\mathrm{F} \ll 1$. As a result, the optical mass in the usual metals is close to m_0, e. g., $m_\mathrm{opt} \approx 1.5\ m_0$ in aluminium [107]. However in quasicrystals, due to their icosahedral symmetry and, consequently, to a large multiplicity of the Bragg planes, the optical mass can essentially differ from the free-electron mass. This can be one of the reasons why the static conductivities of quasicrystals are much lower than those of the crystalline metals.

The optical mass reduces both the static conductivity, and the spectral weight of the intraband optical transitions. The final formula for the intraband Drude optical conductivity can be presented in the form

$$\sigma_{\mathrm{Drude}}(\omega) = \frac{\sigma_{\mathrm{dc}}}{1 - \mathrm{i}\omega\tau}, \quad \sigma_{\mathrm{dc}} = \frac{e^2 n\tau}{m_0} - \sum_{\boldsymbol{g}\in\mathcal{G}} \frac{e^2 g}{24\pi\hbar} \frac{\Delta_{\boldsymbol{g}}\tau}{\hbar} C. \tag{5.16}$$

The spectral weight of the intraband transitions, which is defined as an integral of the real part of optical conductivity, is

$$W_{\mathrm{Drude}} = \int_0^\infty \mathrm{d}\omega \, \mathrm{Re}\, \sigma_{\mathrm{Drude}}(\omega) = \frac{\omega_{\mathrm{p}}^2}{8} - \sum_{\boldsymbol{g}\in\mathcal{G}} \frac{e^2 g \Delta_{\boldsymbol{g}}}{48\hbar^2} C, \tag{5.17}$$

where ω_{p} is the plasma frequency of the free electron gas, $\omega_{\mathrm{p}} = \sqrt{4\pi e^2 n/m_0}$.

The Drude optical conductivity formula (5.16), derived here in the extended zone presentation, corresponds to results obtained in the reduced zone presentation [105]. Both presentations lead to the same physical results for the intraband optical response of the NFE gas.

5.2.2 Interband optical conductivity

The general formula for the interband optical conductivity of the electron subsystem of any optically isotropic medium is given by the formula

$$\sigma_{\mathrm{ib}}(\omega) = \frac{e^2\hbar}{\mathrm{i}3m_0\Omega} \hbar\omega \sum_{\alpha\neq\beta} \frac{f_\alpha f_{\beta\alpha}}{(\varepsilon_\beta - \varepsilon_\alpha)^2 - (\hbar\omega + \mathrm{i}\Gamma)^2}, \tag{5.18}$$

where Ω is the system volume, α and β are the quantum numbers of the initial and final electron states with the energy levels ε_α and ε_β, respectively, Γ is the broadening parameter, f_α is the Fermi distribution function, and $f_{\beta\alpha}$ is the oscillator strength

$$f_{\beta\alpha} = \frac{2}{m_0(\varepsilon_\beta - \varepsilon_\alpha)} \left|\langle\beta|\boldsymbol{p}|\alpha\rangle\right|^2. \tag{5.19}$$

Formula (5.18) corresponds to Ehrenreich and Cohen results [108] and is widely used for a description of the interband optical transitions in the usual crystalline metals [109, 107, 105].

In the reduced zone presentation, the selection rule for the interband transitions requires $\boldsymbol{k}' = \boldsymbol{k}$, and (5.18) reduces to the form

$$\sigma_{\mathrm{ib}}(\omega) = \frac{e^2\hbar}{\mathrm{i}12\pi^3 m_0}\hbar\omega \sum_{n\neq n'} \int_{(\mathrm{BZ})} \frac{f_{n\boldsymbol{k}} f_{n'n}}{[\varepsilon_{n'}(\boldsymbol{k}) - \varepsilon_n(\boldsymbol{k})]^2 - (\hbar\omega + \mathrm{i}\Gamma)^2}. \tag{5.20}$$

In the extended zone presentation, formula (5.18) acquires the form

$$\sigma_{\mathrm{ib}}(\omega) = \frac{2e^2\hbar}{\mathrm{i}3m_0\Omega}\hbar\omega \sum_{\boldsymbol{k}\neq\boldsymbol{k}'} \frac{f_{\boldsymbol{k}} f_{\boldsymbol{k}'\boldsymbol{k}}}{[\varepsilon(\boldsymbol{k}') - \varepsilon(\boldsymbol{k})]^2 - (\hbar\omega + \mathrm{i}\Gamma)^2} \tag{5.21}$$

with the oscillator strength

$$f_{\boldsymbol{k}'\boldsymbol{k}} = \frac{2}{m_0[\varepsilon(\boldsymbol{k}') - \varepsilon(\boldsymbol{k})]} \left|\langle \boldsymbol{k}'|\boldsymbol{p}|\boldsymbol{k}\rangle\right|^2. \tag{5.22}$$

To find the oscillator strength, the matrix element $\langle \boldsymbol{k}'|\boldsymbol{p}|\boldsymbol{k}\rangle$ should be calculated. Within the model of independent intersections (§ 3.3), making use of the wavefunctions (3.21), one finds the matrix element

$$\langle \boldsymbol{k}'|\boldsymbol{p}|\boldsymbol{k}\rangle = \sum_{\boldsymbol{g}\in\mathcal{G}} \frac{\hbar\boldsymbol{g}}{2} \frac{V_{\boldsymbol{g}}}{|V_{\boldsymbol{g}}|} \frac{\gamma}{|\gamma|} \frac{1}{\sqrt{\gamma^2+1}} \delta_{\boldsymbol{k}',\boldsymbol{k}-\boldsymbol{g}} \tag{5.23}$$

and, subsequently, the oscillator strength

$$f_{\boldsymbol{k}'\boldsymbol{k}} = \sum_{\boldsymbol{g}\in\mathcal{G}} \frac{4\varepsilon_0}{\Delta_{\boldsymbol{g}}} \frac{\gamma}{|\gamma|} \frac{1}{(\gamma^2+1)^{3/2}} \delta_{\boldsymbol{k}',\boldsymbol{k}-\boldsymbol{g}}. \tag{5.24}$$

As seen from (5.23) – (5.24), in the extended zone presentation, the interband optical transitions are indirect. They occur from the initial electron state $\boldsymbol{k}$ to the final one, the electron quasimomentum in which differs from $\boldsymbol{k}$ by the reciprocal lattice vector, $\boldsymbol{k}' = \boldsymbol{k} - \boldsymbol{g}$. A scheme of the indirect optical transitions is presented in Fig. 5.10. Note that the transitions are indirect with respect to a projection of the electron quasimomentum onto the reciprocal lattice vector, the $k_{\parallel}$ component. With respect to a perpendicular component, $k_{\perp}$, they are vertical.

The selection rule of the interband optical transitions allows for a trivial summation over the final states $\boldsymbol{k}'$ in the $\sigma_{\mathrm{ib}}(\omega)$ formula (5.21). Replacing the sum over the initial states $\boldsymbol{k}$ by an integral, one obtains the intermediate expression

$$\sigma_{\mathrm{ib}}(\omega) = \sum_{\boldsymbol{g}\in\mathcal{G}} \frac{e^2\hbar\,\hbar\omega}{\mathrm{i}12\pi^3 m_0} \int \mathrm{d}^3k \, \frac{\frac{4\varepsilon_0}{\Delta_{\boldsymbol{g}}} \frac{\gamma}{|\gamma|}}{(\gamma^2+1)^{3/2}} \frac{f_{\boldsymbol{k}}}{[\varepsilon(\boldsymbol{k}-\boldsymbol{g}) - \varepsilon(\boldsymbol{k})]^2 - (\hbar\omega + \mathrm{i}\Gamma)^2}, \tag{5.25}$$

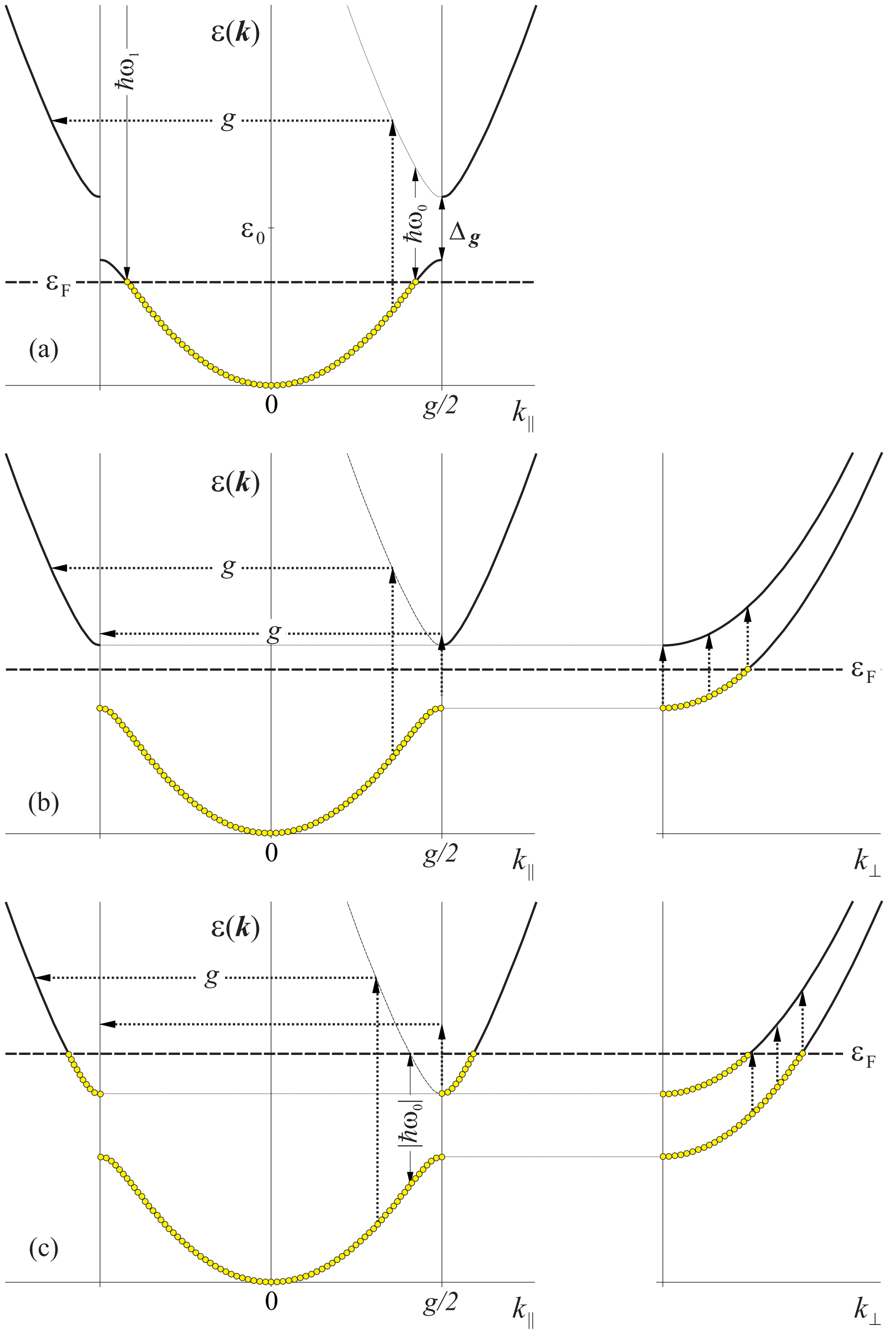

Figure 5.10: Schemes of the interband optical transitions, when the Fermi level is (a) below, (b) within, and (c) above a pseudogap.

which shows that the interband optical conductivity is a sum of partial contributions of the $\boldsymbol{g} \in \mathcal{G}$ Bragg planes. Each term of the sum is determined by a narrow $\boldsymbol{k}$-space strip in a vicinity of the corresponding Bragg plane. Therefore, the energies of the initial and final states, which enter formula (5.25), can be replaced by $\varepsilon(\boldsymbol{k}) = \epsilon_{\boldsymbol{k}} + \delta\varepsilon_{\boldsymbol{g}}(\boldsymbol{k})$, $\varepsilon(\boldsymbol{k}-\boldsymbol{g}) = \epsilon_{\boldsymbol{k}-\boldsymbol{g}} + \delta\varepsilon_{-\boldsymbol{g}}(\boldsymbol{k}-\boldsymbol{g})$, where $\delta\varepsilon_{\boldsymbol{g}}(\boldsymbol{k})$ is the deviation of electron energy from the free electron parabola due to a single Bragg plane, (3.18). As a result, the energy difference $\varepsilon(\boldsymbol{k}-\boldsymbol{g}) - \varepsilon(\boldsymbol{k}) = \Delta_{\boldsymbol{g}} \frac{\gamma}{|\gamma|}\sqrt{\gamma^2+1}$ depends on $k_{\|}$ component only and an integration over $\boldsymbol{k}$ for each term of the $\boldsymbol{g}$-sum in (5.25) can be conveniently carried out in a cylindric coordinate system, $\mathrm{d}^3k = \mathrm{d}\varphi\, \mathrm{d}k_{\|}\, k_{\perp}\mathrm{d}k_{\perp}$, with the polar axis directed along $\boldsymbol{g}$-vector.

An integration over $k_{\perp}$, which involves only the Fermi distribution function, $f_{\boldsymbol{k}} = f(\varepsilon(\boldsymbol{k})) \to f(\epsilon_{\boldsymbol{k}} + \delta\varepsilon_{\boldsymbol{g}}(\boldsymbol{k}))$, results in the same S-function (5.7), which enters formulas of the intraband optical conductivity. The remaining integral over $k_{\|}$ can be reduced to an integral over $x = \sqrt{\gamma^2+1}$, and the final formula for the interband optical conductivity can be presented in the following form:

$$\sigma_{\mathrm{ib}}(\omega) = \sum_{\boldsymbol{g}\in\mathcal{G}} \frac{e^2 g}{24\pi\hbar} \int_1^{x_1} \frac{\mathrm{d}x\, S(x)}{x^3\sqrt{x^2-1}}\, K(x,z,b), \tag{5.26}$$

where the upper limit of integration x_1 and the $S(x)$ function are determined by (5.14) and (5.10)–(5.12), while the kernel $K(x,z,b)$ of the x-integral in (5.26) is defined as

$$K(x,z,b) = \frac{z}{\mathrm{i}\pi}\left[\frac{1}{x-(z+\mathrm{i}b)} + \frac{1}{x+(z+\mathrm{i}b)}\right]. \tag{5.27}$$

Here $z \equiv \hbar\omega/\Delta_{\boldsymbol{g}}$ and $b \equiv \Gamma/\Delta_{\boldsymbol{g}}$ are the dimensionless photon energy and broadening parameter.

Exactly the same expression of the interband optical conductivity (5.26) can be derived in the reduced zone presentation, when formula (5.20) is used as a starting point for $\sigma_{\mathrm{ib}}(\omega)$ calculations. Although the selection rules for optical transitions are different in the extended and reduced presentations, $\boldsymbol{k}' = \boldsymbol{k} - \boldsymbol{g}$ and $\boldsymbol{k}' = \boldsymbol{k}$, both schemes lead to the same physical results.

The spectral weight of the interband optical transitions, as can be proved by the z-integration of the K-kernel (5.27), is given by the formula

$$W_{\mathrm{ib}} = \int_0^{\infty} \mathrm{d}\omega\, \mathrm{Re}\,\sigma_{\mathrm{ib}}(\omega) = \sum_{\boldsymbol{g}\in\mathcal{G}} \frac{e^2 g\Delta_{\boldsymbol{g}}}{48\hbar^2}\, C. \tag{5.28}$$

As seen, the intensity of the interband absorption is proportional to the pseudogap width $\Delta_{\boldsymbol{g}}$ and to the same C-coefficient, which enters Drude optical conductivity formula (5.16).

As seen from a comparison of formulas (5.28) and (5.17), the spectral weight of the interband absorption is compensated by a reduction of the Drude peak exactly by the same amount. This ensures the total spectral weight of optical conductivity to satisfy the oscillator sum rule,

$$W = \int_0^\infty \mathrm{d}\omega \, \mathrm{Re}\, \sigma(\omega) = \frac{\omega_{\mathrm{p}}^2}{8}. \tag{5.29}$$

We presented final formulas for the interband and intraband conductivities in the form of simple x-integrals: (5.26) for $\sigma_{\mathrm{ib}}(\omega)$ and (5.9) for the C-coefficient. The x-integration in the formulas can be carried out analytically. However, the resulting algebraic expressions are lengthy and complicated, they do not shed light on the physical aspects of $\sigma_{\mathrm{ib}}(\omega)$ and $\sigma_{\mathrm{Drude}}(\omega)$ conductivities, and we will not present them here.

The transparent formulas for the interband conductivity can be obtained in the limiting cases of weak and strong scattering.

5.2.3 Weak scattering limit

In the limit of weak scattering, when $\Gamma \ll \Delta_{\boldsymbol{g}}$, the K-kernel (5.27) reduces to the form

$$K(x, z, b) = \frac{z}{\mathrm{i}\pi} \left[\frac{1}{x - z} + \mathrm{i}\pi\delta(x - z) + \frac{1}{x + z} + \mathrm{i}\pi\delta(x + z) \right]. \tag{5.30}$$

Now the real part of the optical conductivity is easy to find due to a simple x-integration with the Dirac δ-function. The final formulas are presented in the following subsections.

Fermi level below pseudogap

When the Fermi level is positioned below the pseudogap, $\varepsilon_{\mathrm{F}} < \varepsilon_0 - \frac{1}{2}\Delta_{\boldsymbol{g}}$, the interband optical conductivity due to a single Bragg plane is given by the formula

$$\mathrm{Re}\, \sigma_{\mathrm{ib}}(\omega) = \frac{e^2 g}{24\pi\hbar} \left(\frac{\Delta_{\boldsymbol{g}}}{\hbar\omega} \right)^2 \frac{(\hbar\omega - \hbar\omega_0)(\hbar\omega_1 - \hbar\omega)}{16\varepsilon_0 \sqrt{(\hbar\omega)^2 - \Delta_{\boldsymbol{g}}^2}}, \tag{5.31}$$

which corresponds to the well-known Butcher result [110], widely used in an analysis of the optical response of alkali metals.

Formula (5.31) predicts an absorption band in the $\hbar\omega_0 < \hbar\omega < \hbar\omega_1$ spectral range, where the absorption edge $\hbar\omega_0 = x_0\Delta_{\boldsymbol{g}}$ and the cut-off energy $\hbar\omega_1 = x_1\Delta_{\boldsymbol{g}}$ are determined by formulas (5.13)–(5.14). The physical meaning of $\hbar\omega_0$ and $\hbar\omega_1$ energies is clarified in Fig. 5.10(a).[1] The absorption band starts at the $\hbar\omega_0$ energy with a linear increase, $\mathrm{Re}\,\sigma_{\mathrm{ib}}(\omega) \propto (\hbar\omega - \hbar\omega_0)$, and later drops down as $\mathrm{Re}\,\sigma_{\mathrm{ib}}(\omega) \propto 1/(\hbar\omega)^2$ in the high frequency limit. The dispersion of the band is presented graphically in Fig. 5.11(a) by a full curve. Dashed curves in the figure present the band calculated by formula (5.26) at several finite values of the broadening parameter Γ.

Fermi level within pseudogap

When the Fermi level is within the pseudogap, $\varepsilon_0 - \frac{1}{2}\Delta_{\boldsymbol{g}} < \varepsilon_{\mathrm{F}} < \varepsilon_0 + \frac{1}{2}\Delta_{\boldsymbol{g}}$, the interband optical conductivity due to a single Bragg plane is given by the formula

$$\mathrm{Re}\,\sigma_{\mathrm{ib}}(\omega) = \frac{e^2 g}{24\pi\hbar}\left(\frac{\Delta_{\boldsymbol{g}}}{\hbar\omega}\right)^2 \frac{(\hbar\omega - \hbar\omega_0)(\hbar\omega_1 - \hbar\omega)}{16\varepsilon_0\sqrt{(\hbar\omega)^2 - \Delta_{\boldsymbol{g}}^2}}. \tag{5.32}$$

Though formally this is the same expression as (5.31), it corresponds to another line-shape of the absorption band.

The absorption edge now is determined by the pseudogap energy $\Delta_{\boldsymbol{g}}$. When the Fermi level is positioned within the pseudogap, the $\hbar\omega_0 = x_0\Delta_{\boldsymbol{g}}$ energy has no direct physical meaning. It acquires both positive, and negative values in the interval $\hbar\omega_0 \in [-\Delta_{\boldsymbol{g}}, \Delta_{\boldsymbol{g}}]$, changing from $\hbar\omega_0 = \Delta_{\boldsymbol{g}}$, when the Fermi level is at the lower edge of the pseudogap, to $\hbar\omega_0 = -\Delta_{\boldsymbol{g}}$, when the Fermi level is at the upper edge of the pseudogap.

The absorption onset now has the $\mathrm{Re}\,\sigma_{\mathrm{ib}}(\omega) \propto 1/\sqrt{\hbar\omega - \Delta_{\boldsymbol{g}}}$ singularity, which, as seen from Fig. 5.11(b), is smeared down at finite values of the broadening parameter.

---

[1] It should be noted that the cut-off energy $\hbar\omega_1$, as seen form Fig. 5.10(a), is determined by the $k_{\|}$ value, which is far-away from the Bragg plane, and, therefore, is not well-justified within the used NFE model of independent intersections. Nevertheless, since the $x_1 = \hbar\omega_1/\Delta_{\boldsymbol{g}}$ parameter is very large, $x_1 \gg 1$, its definite value in practice does not influence optical spectra, and, in principle, all formulas for the interband and intraband optical conductivities can be simplified by taking the limit $x_1 \to \infty$. Here we keep x_1 in the final formulas to facilitate their comparison with the literature results.

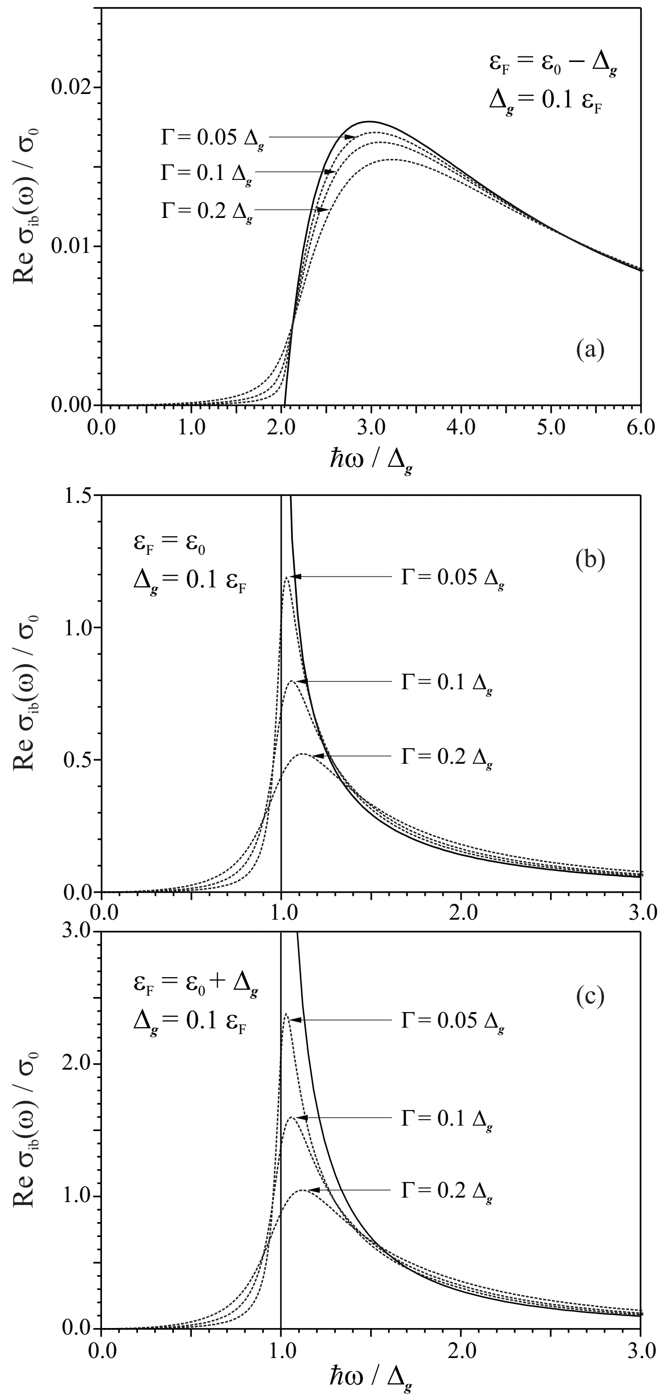

Figure 5.11: Interband absorption bands (in $\sigma_0 = e^2 g/24\pi\hbar$ units) at various positions of the Fermi level with respect to a pseudogap.

Note as well that the absorption band essentially increases in magnitude when the Fermi level enters the pseudogap. This is seen from scales of the absorption bands presented in Fig. 5.11(a) and Fig. 5.11(b). When the Fermi level is raised within the pseudogap, the intensity of the absorption band increases, following the dependence of the C-coefficient on the Fermi level position with respect to the pseudogap (see Fig. 5.9).

Fermi level above pseudogap

When the Fermi level is positioned above the pseudogap, $\varepsilon_{\mathrm{F}} > \varepsilon_0 + \frac{1}{2}\Delta_{\boldsymbol{g}}$, the interband optical conductivity is given by the formula

$$\begin{aligned}\operatorname{Re}\sigma_{\mathrm{ib}}(\omega) &= \frac{e^2 g}{24\pi\hbar}\left(\frac{\Delta_{\boldsymbol{g}}}{\hbar\omega}\right)^2 \\ &\times \begin{cases} \dfrac{\hbar\omega}{\sqrt{(\hbar\omega)^2-\Delta_{\boldsymbol{g}}^2}}, & \Delta_{\boldsymbol{g}} < \hbar\omega < |\hbar\omega_0|, \\ \dfrac{(\hbar\omega+|\hbar\omega_0|)(\hbar\omega_1-\hbar\omega)}{16\varepsilon_0\sqrt{(\hbar\omega)^2-\Delta_{\boldsymbol{g}}^2}}, & |\hbar\omega_0| < \hbar\omega < \hbar\omega_1, \end{cases}\end{aligned} \tag{5.33}$$

which previously was derived in the reduced zone presentation by Ashcroft and Sturm [105] and corresponds to the results of Harrison [111] and Golovashkin et al. [112].

The $\hbar\omega_0 = x_0\Delta_{\boldsymbol{g}}$ energy, which is defined by formula (5.13), in the present case is negative, its modulus corresponds to the energy gap at the Fermi level, as indicated in Fig. 5.10(c). However, the absorption edge is still determined by the pseudogap energy $\Delta_{\boldsymbol{g}}$ due to the optical transitions on faces of the effective Brillouin zone (Fig. 5.10(c)). The absorption band, as in the previous case of ε_{F} within a pseudogap, starts with a singularity, which is smeared down by the scattering parameter (Fig. 5.11(c)).

5.2.4 Strong scattering limit

In the limit of strong scattering (considered by Burkov et al. [102]), when the broadening parameter is much larger than the pseudogap value, $\Gamma \gg \Delta_{\boldsymbol{g}}$, the K-kernel (5.27) reduces to the form

$$K(x,z,b) = \frac{\mathrm{i}2xz}{\pi(z+\mathrm{i}b)^2}. \tag{5.34}$$

Inserting (5.34) into $\sigma_{\mathrm{ib}}(\omega)$ formula (5.26) and carrying out an integration over x, which yields the C coefficient (5.9), one obtains the following

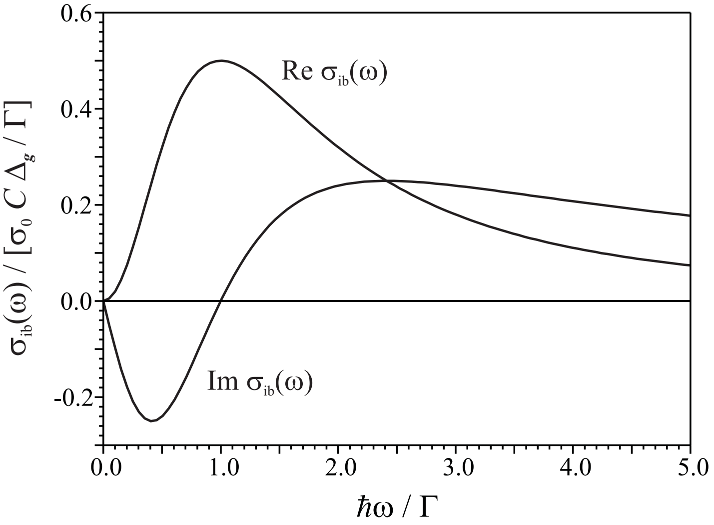

Figure 5.12: Interband optical conductivity spectrum in the strong scattering limit, $\Gamma \gg \Delta_{\boldsymbol{g}}$.

expression for the interband optical conductivity due to a single Bragg plane:

$$\sigma_{\mathrm{ib}}(\omega) = \frac{e^2 g}{24\pi\hbar} \frac{\Delta_{\boldsymbol{g}}}{\Gamma} C \frac{\mathrm{i}\Gamma\hbar\omega}{(\hbar\omega + \mathrm{i}\Gamma)^2}. \tag{5.35}$$

The real and imaginary parts of the interband optical conductivity (5.35) are presented graphically in Fig. 5.12. Note that a position of the absorption band in a present case is determined not by the pseudogap value $\Delta_{\boldsymbol{g}}$, but by the broadening parameter Γ.

The strong scattering limit, $\Gamma \gg \Delta_{\boldsymbol{g}}$, is relevant for very narrow pseudogaps, which correspond to the reciprocal lattice nodes with low structure factors $S_{\boldsymbol{g}}$. Therefore, when modelling optical conductivity spectra of fci-ZnMgRE quasicrystals, we will use formula (5.35) to account for a possible contribution of the low-$S_{\boldsymbol{g}}$ pseudopotentials. Another anticipated effect of the low-$S_{\boldsymbol{g}}$ pseudopotentials on optical spectra, which was not dealt with in the present study, is a broadening of the main, $\mathcal{G}$-induced, optical features by the low-$S_{\boldsymbol{g}}$ scattering.

5.2.5 High frequency limit

In a limiting case of the high frequencies, $\hbar\omega \gg (\Gamma, \Delta_{\boldsymbol{g}})$, the K-kernel (5.27) reduces to

$$K(x, z, b) = \frac{\mathrm{i}2x}{\pi z}. \tag{5.36}$$

Inserting the expression into $\sigma_{\mathrm{ib}}(\omega)$ formula (5.26) and taking an integral over x, which yields the C coefficient (5.9), one obtains the following answer for the interband optical conductivity:

$$\sigma_{\mathrm{ib}}(\omega) = \mathrm{i} \sum_{\boldsymbol{g} \in \mathcal{G}} \frac{e^2 g}{24\pi\hbar} \frac{\Delta_{\boldsymbol{g}}}{\hbar\omega} C \ . \tag{5.37}$$

The intraband optical conductivity in the high frequency limit $\hbar\omega \gg \hbar/\tau$, as seen from (5.16), reduces to the form

$$\sigma_{\mathrm{Drude}}(\omega) = \mathrm{i}\frac{\omega_{\mathrm{p}}^2}{4\pi\omega} - \mathrm{i} \sum_{\boldsymbol{g} \in \mathcal{G}} \frac{e^2 g}{24\pi\hbar} \frac{\Delta_{\boldsymbol{g}}}{\hbar\omega} C, \tag{5.38}$$

where $\omega_{\mathrm{p}} = \sqrt{4\pi e^2 n/m_0}$ is the plasma frequency.

As seen from (5.37) and (5.38), a contribution of the pseudogaps exactly cancels from the total optical conductivity $\sigma(\omega) = \sigma_{\mathrm{Drude}}(\omega) + \sigma_{\mathrm{ib}}(\omega)$, which takes the form $\sigma(\omega) = \mathrm{i}\omega_{\mathrm{p}}^2/(4\pi\omega)$. As a result, the dielectric function $\varepsilon(\omega) = 1 + \mathrm{i}4\pi\sigma(\omega)/\omega$ acquires the form

$$\varepsilon(\omega) = 1 - \frac{\omega_{\mathrm{p}}^2}{\omega^2}, \tag{5.39}$$

which shows the self-consistency of the used description scheme. In the high-frequency limit, the electron subsystem in quasicrystals behaves like the free electron gas, as it should be for any self-consistent physical system.

5.3 Analysis of ZnMgRE optical spectra

The experimental optical conductivity $\sigma(\omega)$ spectra of investigated face-centred icosahedral ZnMgRE quasicrystals are presented by dots in Fig. 5.13. All three, ZnMgY, ZnMgHo, and ZnMgEr, quasicrystals manifest a similar dispersion – spectra are comprised of a distinct optical feature at about 1 eV, which is obviously due to the interband transitions, and the intraband Drude-type contribution at low frequencies. A small kink in the ZnMgHo and ZnMgEr spectra at about 0.13 eV, most probably, is an artefact, – it corresponds to a division line between data recorded by FIR reflectance spectroscopy and IR spectroscopic ellipsometry techniques.

Though the dominant role in an optical response of ZnMgRE, as of other metals, is played by the valence electrons, one can expect a small possible contribution of the bound Zn 3d core electrons. Since the Zn 3d level is at

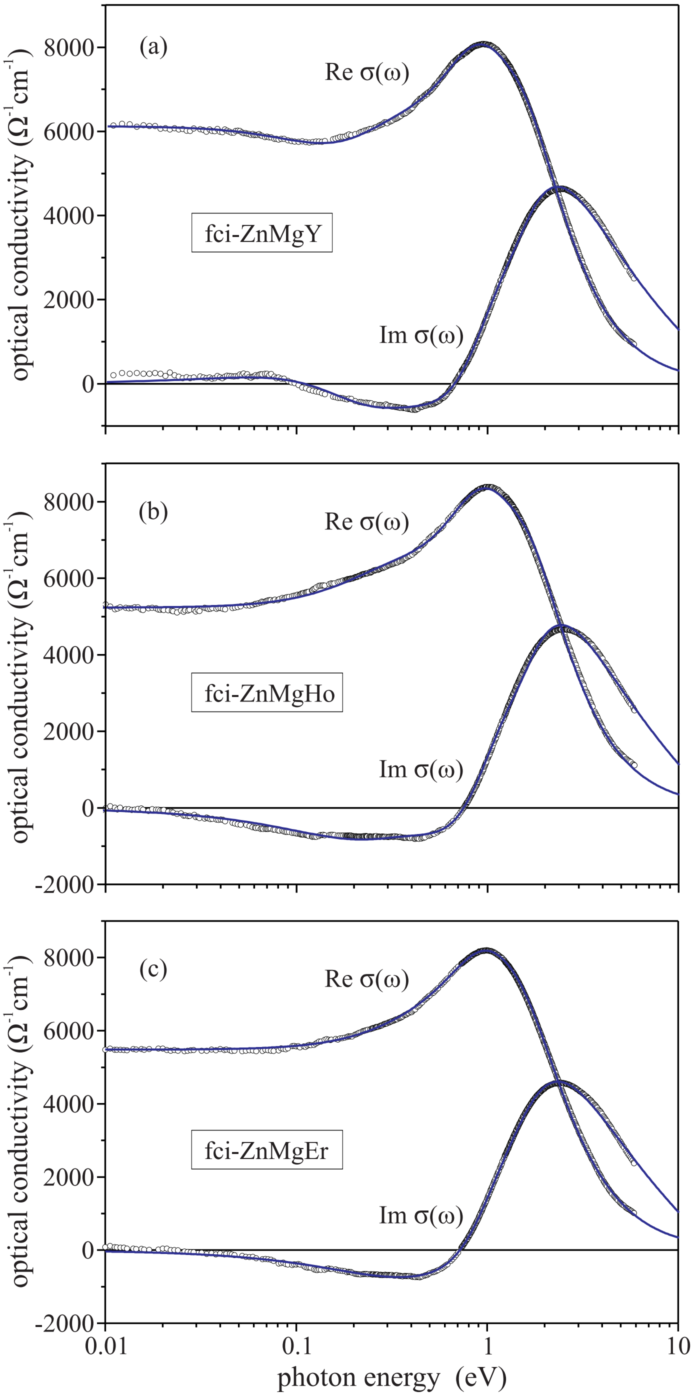

Figure 5.13: The optical conductivity spectra of (a) fci-ZnMgY, (b) fci-ZnMgHo, and (c) fci-ZnMgEr quasicrystals [5]*. Dots present experimental data. Curves correspond to theoretical calculations.

Table 5.1: Parameters of the fci-ZnMgRE intraband optical conductivity.

	fci-ZnMgY	fci-ZnMgHo	fci-ZnMgEr
ω_{p} (eV)	11.5	11.9	11.7
σ_{dc} ($\Omega^{-1}\mathrm{cm}^{-1}$)	6100	5200	5500
$\hbar/\tau$ (eV)	0.18	0.45	0.47
w_{Drude}	0.06	0.12	0.14
m_{opt} (m_0)	16	8.1	7.2

a bottom of the valence band, approximately 10 eV below the Fermi level, [68, 69, 70] a feasible Zn 3d polarization was accounted for by introducing the high frequency dielectric constant into the dielectric function of the quasicrystals,

$$\varepsilon(\omega) = \varepsilon_\infty + \mathrm{i}\frac{4\pi}{\omega}\left[\sigma_{\mathrm{Drude}}(\omega) + \sigma_{\mathrm{ib}}(\omega)\right]. \tag{5.40}$$

In the present study, the high frequency dielectric constant ε_∞ was treated as an empirical parameter. The theoretical simulations of the optical conductivity spectra were carried out on a basis on formulas derived in the previous section. The calculations require for given values of the Fermi energy ε_{F}, the pseudogap widthes Δ_{222100} and Δ_{311111}, and the broadening constants Γ, which were treated as adjustable parameters. The reciprocal lattice vectors of the $\mathcal{G}$-star and the corresponding intersection energies $\varepsilon_0 = \hbar^2(\frac{1}{2}g)^2/2m_0$ were fixed by their values, determined in the XRD-study (Chapter 2).

Results of the fci-ZnMgRE optical conductivity calculations are presented by curves in Fig. 5.13. As seen, they perfectly reproduce the experimental data.

The high-frequency dielectric constant, as expected, is close to unity, $\varepsilon_\infty = 1.35$, 1.56, and 1.58 for ZnMgY, ZnMgHo, and ZnMgEr, respectively, and does not essentially influence an optical response of the quasicrystals.

The plasma frequency ω_{p} values, which determine the total spectral weight of $\mathrm{Re}\,\sigma(\omega)$ spectra (eq. (5.29)), are of about 11.5 – 11.9 (Table 5.1) and are close to the theoretical values $\omega_{\mathrm{p}}^{\mathrm{ZnMgY}} = 12.7$ eV, $\omega_{\mathrm{p}}^{\mathrm{ZnMgHo}} = 12.5$ eV, and $\omega_{\mathrm{p}}^{\mathrm{ZnMgEr}} = 12.4$ eV, predicted by the formula $\omega_{\mathrm{p}} = \sqrt{4\pi e^2 n/m_0}$ at the valence electron concentrations n, which were determined from the known mass densities ρ and average valences $\overline{Z}$ (Table 1.1).

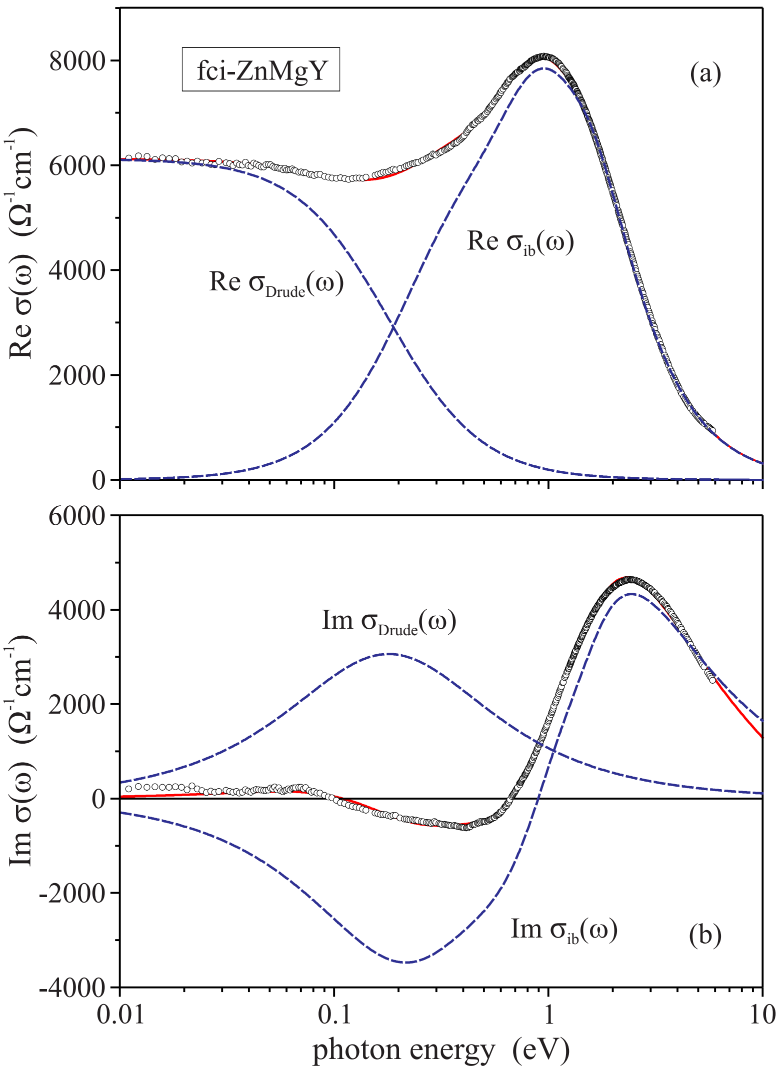

Figure 5.14: The partial intraband and interband contributions to the fci-ZnMgY optical conductivity spectrum [5]*.

5.3.1 Drude optical conductivity

Figure 5.14 shows the partial intraband and interband contributions to the fci-ZnMgY total optical conductivity spectrum. The relative spectral weight of the intraband Drude conductivity, $w_{\text{Drude}} = W_{\text{Drude}}/W$, with respect to the total $\sigma(\omega)$ spectral weight W, is of about 10 % (see Table 5.1).

The relative spectral weight w_{Drude}, as can be easily checked from formulas (5.8) and (5.17), unambiguously determines the optical mass, $m_{\text{opt}} = m_0/w_{\text{Drude}}$. Therefore, the optical mass in the fci-ZnMgRE quasicrystals is of about 10 m_0 (see Table 5.1), what reduces the static conductivity of the QC's by ca. ten times with respect to σ_{dc} of the usual crystalline metals.

The parameters of the intraband optical conductivity, the static conductivity and the relaxation time, are presented in Table 5.1. The determined static conductivity values $\sigma_{\mathrm{dc}} \sim 5000-6000\ \Omega^{-1}\mathrm{cm}^{-1}$ roughly correspond to the Fisher et al. results of the electric resistivity measurements [35, 113]: $\sigma_{\mathrm{dc}} \approx 6620$, 5410, and 5880 $\Omega^{-1}\mathrm{cm}^{-1}$ for ZnMgY, ZnMgHo, and ZnMgEr, respectively. The relaxation times $\tau \sim 0.14-0.4\ 10^{-14}$ s determined are longer than the τ values we obtained from the $\sigma(\omega)$ analysis in a narrower spectral range of $0.1-6$ eV [2, 4]*, but closer to the ZnMgY and ZnMgTb relaxation times reported by Chernikov et al. [100], $\tau \sim 0.5\ 10^{-14}$ s, determined in the wide-range, $0.001-10$ eV, reflectance-spectroscopy study.

The wide spectral range measurements are essential for a reliable determination of the Drude contribution. Indeed, the analysis of the si-ZnMgHo [2]* and fci-ZnMgRE (RE = Y, Ho, Er) [4]* $\sigma(\omega)$ spectra, recorded in the $0.1-6$ eV range, yielded about ten times shorter relaxation times, namely $0.04\ 10^{-14}$ s for si-ZnMgHo [2]* and $0.03-0.04\ 10^{-14}$ s for fci-ZnMgRE [4]*. Though the short τ values are in accord with those reported for some other quasicrystals, e. g. $\tau \sim 0.047\ 10^{-14}$ s for fci-AlPdMn [102], the ZnMgRE relaxations times $\tau \sim 0.14-0.4\ 10^{-14}$ s determined from the wide-range optical spectra analysis are more reliable.

5.3.2 Interband optical conductivity

The fci-ZnMgRE interband optical conductivity $\sigma_{\mathrm{ib}}(\omega)$ spectra, which were obtained by a subtraction of the determined Drude contribution $\sigma_{\mathrm{Drude}}(\omega)$ from the total optical conductivity, are presented in Fig. 5.15, where dots and curves correspond to the experimental data and theoretical calculations, respectively.

The interband optical conductivity is due to the optical transitions across the 222100 and 311111 pseudogaps and due to a contribution of the $\boldsymbol{g} \notin \mathcal{G}$ pseudopotentials with low structure factors. The relative spectral weights of $\mathrm{Re}\,\sigma_{\mathrm{ib},222100}(\omega)$, $\mathrm{Re}\,\sigma_{\mathrm{ib},311111}(\omega)$, and $\mathrm{Re}\,\sigma_{\mathrm{ib},g\notin\mathcal{G}}(\omega)$ interband conductivities (with respect to the total spectral weight W) are of about 0.5, 0.3, and 0.1, correspondingly (see Table 5.2). Decomposition of the fci-ZnMgY interband optical conductivity spectrum to the partial contributions is shown in Fig. 5.16.

The parameters of the electron energy spectrum, the Fermi energy ε_{F}, the pseudogap widthes Δ_{222100} and Δ_{311111}, and the broadening parame-

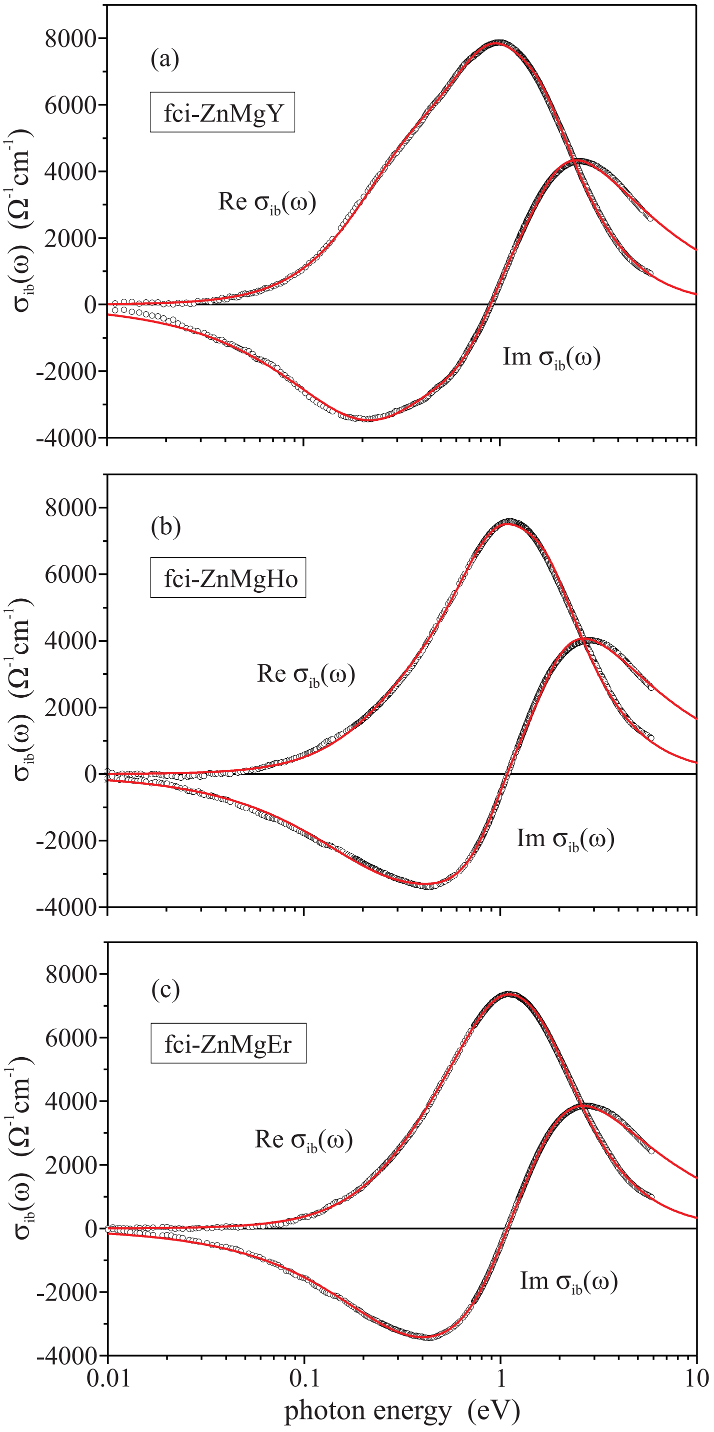

Figure 5.15: Interband optical conductivity of (a) fci-ZnMgY, (b) fci-ZnMgHo, and (c) fci-ZnMgEr quasicrystals [5]*.

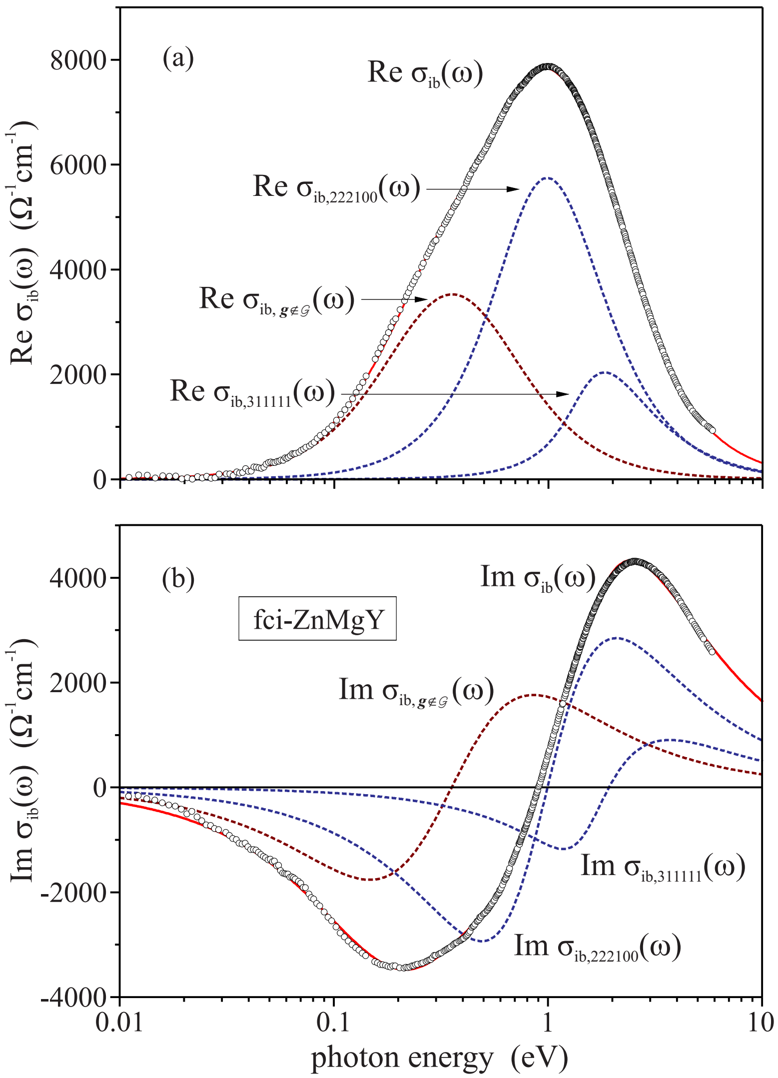

Figure 5.16: The partial interband contributions $\sigma_{\mathrm{ib},222100}(\omega)$, $\sigma_{\mathrm{ib},311111}(\omega)$, and $\sigma_{\mathrm{ib},g\notin\mathcal{G}}(\omega)$ to the fci-ZnMgY total interband optical conductivity spectrum [5]*.

Table 5.2: The relative spectral weights of the interband transitions across the 222100 and 311111 pseudogaps and of the transitions induced by the low $S_{\boldsymbol{g}}$-factor pseudopotentials.

	fci-ZnMgY	fci-ZnMgHo	fci-ZnMgEr
w_{222100}	0.51	0.50	0.49
w_{311111}	0.29	0.29	0.25
$w_{g\notin\mathcal{G}}$	0.14	0.08	0.12

Table 5.3: Parameters of fci-ZnMgRE electron energy spectrum: the Fermi energy ε_{F}, the pseudogaps Δ_{222100} and Δ_{311111}, and the broadening parameters $\Gamma_{222100} = \Gamma_{311111} \equiv \Gamma_{\mathcal{G}}$ and $\Gamma_{g \notin \mathcal{G}}$. The values of the parameters, deduced from an analysis of the photoemission data [68, 69], are presented in parenthesis.

	fci-ZnMgY	fci-ZnMgHo	fci-ZnMgEr
ε_{F} (eV)	9.25 (9.31)	9.25 (9.32)	9.20 (9.32)
Δ_{222100} (eV)	0.55 (0.63)	0.60 (0.61)	0.61 (0.64)
Δ_{311111} (eV)	1.36 (1.16)	1.45 (0.98)	1.34 (1.25)
$\Gamma_{\mathcal{G}}$ (eV)	0.62 (0.23)	0.63 (0.22)	0.68 (0.24)
$\Delta_{g \notin \mathcal{G}}$ (eV)	$\ll \Gamma_{g \notin \mathcal{G}}$	$\ll \Gamma_{g \notin \mathcal{G}}$	$\ll \Gamma_{g \notin \mathcal{G}}$
$\Gamma_{g \notin \mathcal{G}}$ (eV)	0.35	0.41	0.55

ters, which were determined by the standard least-squares technique, are presented in Table 5.3. The Fermi energy $\varepsilon_{\mathrm{F}} = 9.20 - 9.25$ eV and the pseudogap $\Delta_{222100} = 0.55 - 0.61$ eV and $\Delta_{311111} = 1.34 - 1.45$ eV values are very close to those, deduced from an analysis of the fci-ZnMgRE valence band photoemission (PE) spectra [68, 69], namely, $9.31 - 9.32$ eV for the Fermi energy, $0.61 - 0.64$ eV for the Δ_{222100}, and $0.98 - 1.25$ eV for Δ_{311111} pseudogaps. This is a sound support for a self-consistency of the QC electron energy spectrum model suggested – it nicely reproduces experimental data for both the optical, and PE response of the fci-ZnMgRE quasicrystals at actually the same values of energy spectrum parameters.

The broadening parameter $\Gamma_{\mathcal{G}}$ of the interband transitions across pseudogaps, which was assumed to be the same for Δ_{222100} and Δ_{311111}, is of about $0.62 - 0.68$ eV (Table 5.3). It differs from the broadening parameter determined in PE analysis, $\Gamma_{\mathrm{PE}} \approx 0.22 - 0.24$ eV. We do not know the exact reasons for the difference, moreover that the broadening in the optical and PE data analysis is introduced by different phenomenological schemes, – in optics, as the Lorentzian-type broadening of the spectral lines (see the K-kernel formula (5.27)), in PE, as the Gaussian convolution of the density of states.

The broadening parameter $\Gamma_{g \notin \mathcal{G}}$ of the interband transitions induced by the pseudopotentials with low structure factors is of about $0.35 - 0.55$ eV

(Table 5.3). Since the line-shape of $\sigma_{\mathrm{ib},g\notin\mathcal{G}}(\omega)$ is determined solely by the broadening parameter (see eq. (5.35)), the pseudopotentials $V_{g\notin\mathcal{G}}$ and the corresponding pseudogaps $\Delta_{g\notin\mathcal{G}} = 2|V_{g\notin\mathcal{G}}|$ can not be directly deduced from the optical spectra analysis. They determine only the spectral weight of the $\{g \notin \mathcal{G}\}$-transitions,

$$W_{g\notin\mathcal{G}} = \sum_{g\notin\mathcal{G}} \frac{e^2 g \Delta_{g\notin\mathcal{G}}}{48\hbar^2} C. \tag{5.41}$$

A rough estimate of the $\Delta_{g\notin\mathcal{G}}$ pseudogaps can be obtained assuming that all $\boldsymbol{g}$-vectors contributing to the (5.41) sum have the same moduli, $g \approx 2k_{\mathrm{F}}$, and correspond to the same pseudogap values. Then, under assumption that a multiplicity of the $g \notin \mathcal{G}$ vectors is 60 and that $C \approx 1$, we obtain the $\Delta_{g\notin\mathcal{G}} \sim 0.03 - 0.04$ eV estimate. Though the estimate indicates to very low $\Delta_{g\notin\mathcal{G}}$ pseudogap values as compared to those of Δ_{222100} and Δ_{311111}, it is in accord with results of the fci-ZnMgRE XRD study (Chapter 2), which resolves the Bragg peaks with their intensity ratios below $\sim 10^{-5}$ (see, e. g., Fig. 2.9).

Discussion

Finally we would like to point out that, due to a rather smooth spectral shape of ZnMgRE optical spectra, a determination of both intraband, and interband parameters, most probably, is not unambiguous.

The fci-ZnMgRE and si-ZnMgHo optical conductivity spectra, previously recorded in the narrower spectral range of $0.1 - 6$ eV [4, 2]*, can be qualitatively interpreted as due to interband transitions across a single, 311111, pseudogap (Fig. 5.17). However, this requires for very short Drude relaxation times, $\tau \sim 0.03\ 10^{-14}$ s ($\hbar/\tau \sim 2$ eV), for a decrease of the Δ_{311111} value down to ~ 0.8 eV and for an increase of the Fermi energy up to $9.7 - 9.8$ eV.

The reliability of the set of parameters, determined in an analysis of the wide spectral range fci-ZnMgRE data, is soundly confirmed by the fact, that the electron energy spectrum in a vicinity of the Fermi level is predicted by the optical data analysis to have the same structure as that predicted by the photoemission spectra analysis – the Fermi level is slightly above the 222100 pseudogap, and is positioned in a lower part of the 311111 pseudogap. This is illustrated in Fig. 5.18 for fci-ZnMgY quasicrystal. The same holds true for fci-ZnMgHo and fci-ZnMgEr (see Table 5.3).

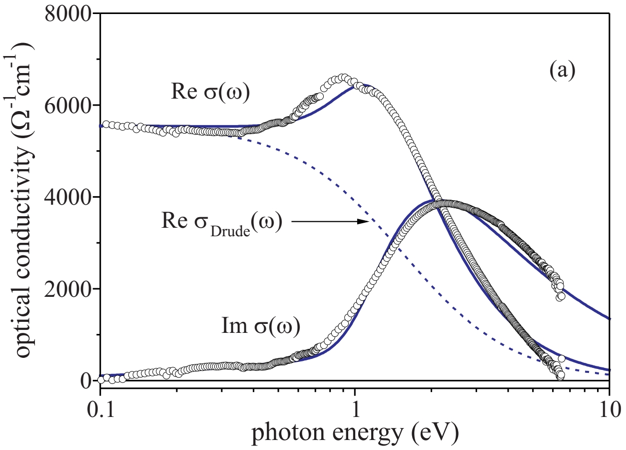

Figure 5.17: The total (a) and interband (b) optical conductivity spectra of si-ZnMgHo quasicrystal [2]*. Dots and curves present, respectively, experimental data and results of the theoretical simulation under an assumption of interband transitions across a single (311111) pseudogap.

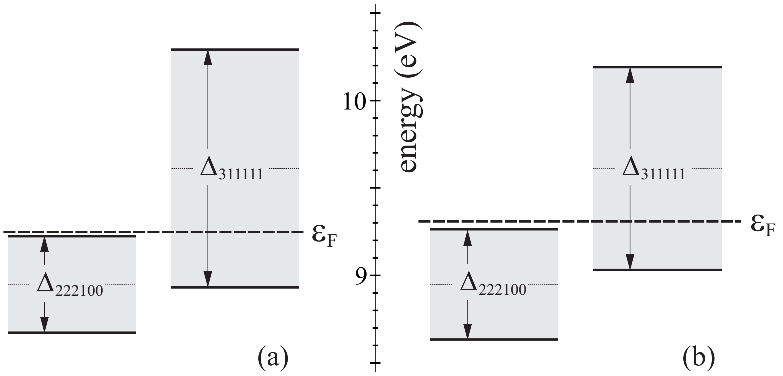

Figure 5.18: Scheme of the fci-ZnMgY electron energy spectrum in a vicinity of the Fermi level, predicted from analysis of optical (a) and photoemission spectroscopy (b) data.

5.4 Resumé

Summarizing, the optical spectra of ZnMgRE quasicrystals are comprised of a distinct interband optical feature at about 1 eV and the intraband Drude-type contribution at low frequencies.

The combined spectroscopic ellipsometry and reflectance spectroscopy technique allowed for a recording of the wide-spectral-range, 0.01 – 6 eV, fci-ZnMgRE (RE = Y, Ho, Er) optical conductivity $\sigma(\omega)$ spectra.

The Ashcroft and Sturm scheme of the $\sigma(\omega)$ theoretical calculations was extended to account for various positions of the Fermi level with respect to a pseudogap.

An analysis of the fci-ZnMgRE optical conductivity spectra shows that the intraband, Drude-type, optical transitions contribute to the total optical conductivity with a relative spectral weight of about 10 %. The Drude relaxation times are of about 0.14 – 0.4 10^{-14} s.

The interband optical conductivity is predominantly due to the optical transitions across 222100 and 311111 pseudogaps. Their relative spectral weight is of about 80 %. An influence of the low structure-factor pseudopotentials on the optical response of ZnMgRE quasicrystals was revealed. The relative spectral weight of the low-S_g contribution is of about 10 %.

The experimental fci-ZnMgRE optical conductivity spectra are perfectly reproduced by theoretical calculations performed within the framework of the suggested electron energy spectrum model. The set of the electron energy spectrum parameters determined from an analysis of the optical data predicts actually the same structure of the Fermi-level vicinity electron energy spectrum as was previously predicted from an analysis of photoemission data.

Main results and conclusions

- The XRD study of ZnMgRE quasicrystals, carried out with the state-of-the-art diffractometers, equipped, however, with the usual copper-anode X-ray sources, revealed a rich structure of ZnMgRE reciprocal lattice, which is usually observed in the synchrotron-radiation facilities XRD studies only.

- The fci-ZnMgY diffraction peaks with the unusually large complementary reciprocal lattice vectors up to $g_{\perp}a = 23.9$ were resolved (as compared to the literature result of $g_{\perp}a = 17.3$, obtained in the synchrotron-facilities fci-ZnMgY XRD study). The manifestation of the large complementary $\boldsymbol{g}_{\perp}$-vectors indicates an exceptional structural quality of the studied ZnMgRE quasicrystals.

- The combined spectroscopic ellipsometry and reflectance spectroscopy technique, based on a suggested anchor-window method, was worked out. The anchor-window method essentially improves an accuracy of the dielectric function and/or optical conductivity determination from reflectivity spectra.

- The most effective tool for ZnMgRE optical-surface preparation proved to be a combined mechanical polishing and plasma-etching technique.

- High-accuracy fci-ZnMgRE (RE = Y, Ho, Er) optical conductivity $\sigma(\omega)$ spectra were recorded in the wide, 0.01 – 6 eV, spectral range.

- The model of ZnMgRE electron energy spectrum, previously suggested for an interpretation of the experimental ZnMgRE photoemission spectra, was developed. The nearly-free-electron gas model of independent intersections was formulated in the extended zone presentation.

- The electron subsystem in ZnMgRE quasicrystals maintains the nearly free electron gas character. The energy spectrum of electrons in a vicinity of the Fermi level is determined by the Fermi surface intersections with (222100) and (311111) families of Bragg planes.

- The Ashcroft and Sturm scheme of the theoretical $\sigma(\omega)$ calculations was extended to account for various positions of the Fermi level with respect to a pseudogap.

- The optical response of ZnMgRE quasicrystals, as of other metallic compounds, is determined by the intraband Drude-type and interband optical transitions. The intraband transitions contribute to the total optical conductivity with a relative spectral weight of about 10 %. The Drude relaxation times are of about $0.14 - 0.4\ 10^{-14}$ s. The intersections of Fermi surface with Bragg planes lead to an essential increase of the optical mass in quasicrystals, as compared to the usual crystalline metals. The ZnMgRE optical mass is of the order of 10 m_0.

- The interband ZnMgRE optical conductivity is predominantly due to the optical transitions across 222100 and 311111 pseudogaps. Their relative spectral weight is of about 80 %. An influence of the low structure-factor pseudopotentials on the ZnMgRE optical response was revealed. The relative spectral weight of the low-$S_{\boldsymbol{g}}$ contribution is of about 10 %.

- The experimental fci-ZnMgRE optical conductivity spectra are reproduced in detail by theoretical $\sigma(\omega)$ calculations performed within the framework of the suggested electron energy spectrum model. The set of the electron energy spectrum parameters determined from an analysis of the optical data predicts actually the same structure of the Fermi level-vicinity electron energy spectrum, as was previously predicted from an analysis of photoemission data.

Notations and abbreviations

Main notations

a, the quasilattice constant, 6

C-coefficient, 76
C_n, the n-fold rotation symmetry axis

$\Delta_{\boldsymbol{g}}$, the pseudogap, 44, 91
$\delta\varepsilon_{\boldsymbol{g}}(\boldsymbol{k})$, a deviation of the electron energy spectrum from a parabolic dispersion due to an intersection with a single Bragg plane, 43

$\boldsymbol{e}_i$, the unit vectors of icosahedron, 7
ε_∞, the high frequency dielectric constant, 89
ε_0, the intersection energy, 44
ε_{F}, the Fermi energy, 91
$\varepsilon(\omega)$, the dielectric function

$f_{\boldsymbol{k}}$, the Fermi distribution function
$f_{\boldsymbol{k}'\boldsymbol{k}}$, the oscillator strength, 79

Γ, the broadening parameter, 69, 94
$\mathcal{G}$ star, 40
$\boldsymbol{g}$, the reciprocal lattice vector, 10
$\boldsymbol{g}_\perp$, the complementary reciprocal lattice vector, 10

$\boldsymbol{k}$, the wave vector
$\boldsymbol{k}$, the electron quasimomentum, 40
k_{F}, the Fermi wave vector, 13

m_{opt}, the optical mass, 74, 90

n, the valence electron concentration, 13

ω_{p}, the plasma frequency, 89

$\boldsymbol{q}$, the diffraction vector, 21

$R(\omega)$, the reflectivity spectrum

σ_{dc}, the static electric conductivity, 74, 91
$\sigma(\omega)$, the optical conductivity, 70
$\sigma_{\mathrm{Drude}}(\omega)$, the intraband optical conductivity, 90
$\sigma_{\mathrm{ib}}(\omega)$, the interband optical conductivity, 91
S-function, 76
$S_{\boldsymbol{g}}$, the structure factor of the reciprocal lattice, 10

τ, the golden mean, 5
τ, the relaxation time, 74, 91
ϑ-2ϑ, theta-2theta diffraction, 20

$V_{\boldsymbol{g}}$, the Fourier amplitude of QC potential, the pseudopotential, 38

W, the spectral weight, 78
w, the relative spectral weight, 90

Abbreviations

1D, one-dimensional
2D, two-dimensional
3D, three-dimensional

AW, the anchor-widow, 55

bci, body-centred icosahedral, 8

DOS, the density of states, 37

EDX, the energy dispersive X-ray spectroscopy

fci, face-centred icosahedral, 8
FIR, far-infrared
FT, Fourier transform, 54

IR, infrared

KK, Kramers–Kronig, 55

NFE, nearly free electron approximation, 39
NIR, near-infrared

PDF, the pseudodielectric function, 49
PE, the photoemission spectroscopy

QC, quasicrystal, quasicrystalline
QCs, quasicrystals

RE, rare earth element, 2
RSM, reciprocal space mapping, 29

SE, spectroscopic ellipsometry, 47
si, simple icosahedral, 8

TB-LMTO, the tight-binding linear-muffin-tin-orbital method
TEM, transmission electron microscopy

UHV, ultra-high vacuum
UV, ultraviolet

XPS, X-ray photoemission spectroscopy
XRD, X-ray diffraction, 15

Bibliography

[1] V. Karpus, G.-J. Babonas, A. Rėza, A. Suchodolskis, S. Tumėnas, O. Hunderi, W. Assmus, and S. Brühne, Optical response of fci-ZnMgHo quasicrystal, *Acta Phys. Pol. A* **113**(3), 1005–1008 (2008).

[2] V. Karpus, G.-J. Babonas, A. Rėza, S. Tumėnas, H. Arwin, W. Assmus, and Stefan Brühne, Optical response of si-ZnMgHo quasicrystal, *Zietschrift für Kristallographie* **224**(1–2), 39–41 (2009).

[3] S. Tumėnas, I. Kašalynas, V. Karpus, and H. Arwin, Infrared reflectance Kramers–Kronig analysis by anchor-window technique, *Acta Phys. Pol. A* **119**(2), 140–142 (2011).

[4] S. Tumėnas, V. Karpus, H. Arwin, and W. Assmus, Optical conductivity of fci-ZnMgRE quasicrystals, *Thin Solid Films* **519**(9), 2951–2954 (2011).

[5] V. Karpus, S. Tumėnas, A. Suchodolskis, H. Arwin, and W. Assmus, Optical spectroscopy and electronic structure of the face-centered icosahedral quasicrystals Zn-Mg-R (R = Y, Ho, Er), *Phys. Rev. B* (submitted for publication).

[6] V. Karpus, G.-J. Babonas, A. Rėza, A. Suchodolskis, S. Tumėnas, W. Assmus, and S. Brühne, Dielectric function of i-ZnMgHo quasicrystals, *13th Int. Symposium on Ultrafast Phenomena in Semiconductors 13-UFPS (Vilnius, 2007.08.26–29). Abstracts* (Vilnius, 2007), p. 26.

[7] V. Karpus, G.-J. Babonas, A. Rėza, S. Tumėnas, H. Arwin, W. Assmus, and S. Brühne, Optical response of si-ZnMgHo quasicrystal, *10th Int. Conf. on Quasicrystals ICQ10 (Zürich, 2008.07.07–11). Program and Abstracts* (Zürich, 2008), p. 94.

[8] S. Tumėnas, V. Karpus, H. Arwin, and W. Assmus, Optical conductivity of fci-ZnMgRE quasicrystals, *5th Int. Conf. on Spectroscopic Ellipsometry ICSE-V (Albany NY, 2010.05.23–28). Oral and Poster Abstracts.*

[9] S. Tumėnas, I. Kašalynas, V. Karpus, and H. Arwin, Infrared reflectance Kramers–Kronig analysis by anchor-window technique, *14th Int. Symposium on Ultrafast Phenomena in Semiconductors 14-UFPS (Vilnius, 2010.08.23–25).*

[10] F. Eriksson, S. Olsson, V. Karpus, S. Tumenas, J. Birch, and L. Hultman, Investigations of ZnMgY quasicrystals in reciprocal space, *BIT's 1st Annual Conference and EXPO of AnalytiX-2012 (Beijing, 2012.03.23–25). Program* (Beijing, 2012).

[11] S. Tumėnas, V. Karpus, R. Kondrotas, and H. Arwin, Spectroscopic ellipsometry study of moncrystalline Zn, *6th Int. Conf. on Spectroscopic Ellipsometry ICSE-VI (Kyoto, 2013.05.26–31). Conference Program and Abstracts*, p. 79.

[12] S. Tumėnas, V. Karpus, A. Rėza, H. Arwin, Dielektrinė paprastųjų ikosaedrinių cinkas-magnis-holmis kvazikristalų funkcija, *XII-oji jaunųjų mokslininkų konferencija "Mokslas – Lietuvos ateitis. Fizika ir fizinė kompiuterija" (Vilnius, 2009.04.02). Programa* (Vilnius, 2009).

[13] S. Tumėnas, I. Kašalynas, V. Karpus, Inkaro lango metodas Kramerso–Kronigo analizėje, *XIII-oji jaunųjų mokslininkų konferencija "Mokslas – Lietuvos ateitis. Fizika ir fizinė kompiuterija" (Vilnius, 1010).*

[14] S. Tumėnas, V. Karpus, I. Kašalynas, D. Seliuta, L. Žigas, Optical IR response of fci-ZnMgY quasicrystals, *38th Lithuanian National Conference on Physics (Vilnius, 2009.06.08–10). Program and Abstracts* (Vilnius, 2009), p. 79.

[15] S. Tumėnas, V. Karpus, and F. Eriksson, X-ray θ-2θ diffraction of ZnMgY quasicrystal, *39th Lithuanian National Conference on Physics (Vilnius, 2011.06.06–08). Program and Abstracts* (Vilnius, 2011), p. 69.

[16] S. Tumėnas, R. Juškėnas, V. Karpus, F. Eriksson, S. Olsson, J. Birch, L. Hultman, and W. Assmus, Phason strain in fci-ZnMgY quasicrystals, *40th Lithuanian National Conference on Physics (Vilnius, 2013.06.10–12). Program and Abstracts* (Vilnius, 2013), p. 149.

[17] S. Tumėnas, V. Karpus, R. Kondrotas, and H. Arwin, Ellipsometric measurements of zinc dielectric function tensor, *40th Lithuanian National Conference on Physics (Vilnius, 2013.06.10–12). Program and Abstracts* (Vilnius, 2013), p. 148.

[18] R. Kondrotas, R. Juškėnas, S. Tumėnas, V. Karpus, and S. Raman, XPS study of ZnMgRE quasicrystal surface layers, *40th Lithuanian National Conference on Physics (Vilnius, 2013.06.10–12). Program and Abstracts* (Vilnius, 2013), p. 98.

[19] S. Tumėnas, Trijų aplinkų heterostruktūros atspindžio amplitudės, *10-osios Lietuvos jaunųjų mokslininkų konferencijos "Mokslas – Lietuvos ateitis" (Vilnius, 2007.04.06) medžiaga* (Vilnius, 2007), p. 112–116.

[20] S. Tumėnas, V. Karpus, K. Bertulis, and H. Arwin, Dielectric function and refractive index of $\mathrm{GaAs}_{1-x}\mathrm{Bi}_x$ ($x = 0.035,\ 0.052,\ 0.075$), *Phys. Status Solidi C* **9**(7), 1633–1635 (2012).

[21] V. Bukauskas, A. Šetkus, I. Šimkienė, S. Tumėnas, I. Kašalynas, A. Rėza, J. Babonas, V. Časaitė, S. Povilonienė, and R. Meškys, Solid surface dependent layering of self-arranged structures with fibril-like assemblies of alpha-synuclein, *Applied Surface Science* **258**, 4383–4390 (2012).

[22] Z. Balevicius, A. Makaraviciute, G.-J. Babonas, S. Tumenas, V. Bukauskas, A. Ramanaviciene, and A. Ramanavicius, Study of optical anisotropy in thin molecular layers by total internal reflection ellipsometry, *Sensors and Actuators B* **181**, 119–124 (2013).

[23] S. Tumėnas, V. Karpus, K. Bertulis, and H. Arwin, Refractive index of $\mathrm{GaAs}_{1-x}\mathrm{Bi}_x$ ($x \approx 0.075$), *16th Semiconducting and Insulating Materials Conference SIMC XVI (Stockholm, 2011.06.19–23). Programme and Abstracts*, p. Tu3–11.

[24] Z. Balevicius, A. Makaraviciute, I. Baleviciute, S. Tumenas, A. Stirke, A. Ramanaviciene, and A. Ramanavicius, *In situ* study of ligand-receptor interaction by total internal reflection ellipsometry, *6th Int. Conf. on Spectroscopic Ellipsometry ICSE-VI (Kyoto, 2013.05.26–31). Conference Program and Abstracts*, p. 238.

[25] D. Shechtman, I. Blech, D. Gratias, and J. W. Cahn, Metallic phase with long-range orientational order and no translational symmetry, *Phys. Rev. Lett.* **53**(20), 1951–1953 (1984).

[26] D. Levine and P. J. Steinhardt, Quasicrystals: A new class of ordered structures, *Phys. Rev. Lett.* **53**(26), 2477–2480 (1984).

[27] D. Levine and P. J. Steinhardt, Quasicrystals. I. Definition and structure, *Phys. Rev. B* **34**(2), 596–616 (1986).

[28] J. E. S. Socolar and P. J. Steinhardt, Quasicrystals. II. Unit-cell configurations, *Phys. Rev. B* **34**(2), 617–647 (1986).

[29] L. Bindi, P. J. Steinhardt, N. Yao, and P. J. Lu, Natural quasicrystals, *Science* **324**, 1306–1309 (2009).

[30] B. Dubost, J.-M. Lang, M. Tanaka, P. Sainfort, and M. Audier, Large AlCuLi single quasicrystals with triacontahedral solidification morphology, *Nature* **324**, 48–50 (1986).

[31] A.-P. Tsai, A. Inoue, and T. Masumoto, A stable quasicrystal in Al-Cu-Fe system, *Jpn. J. Appl. Phys.* **26**(9), L1505–L1507 (1987).

[32] A. P. Tsai, A. Inoue, Y. Yokoyama, and T. Masumoto, New icosahedral alloy with superlattice ordering in the AlPdMn system prepared by rapid solidification, *Phil. Mag. Lett.* **61**(1), 9–14 (1990).

[33] Z. P. Luo, S. Q. Zhang, Y. L. Tang, and D. S. Zhao, Quasicrystals in as-cast Mg-Zn-RE alloys, *Scripta Metall. Mater.* **28**, 1513 (1993).

[34] A. P. Tsai, A. Niikura, A. Inoue, T. Masumoto, Y. Nishida, K. Tsuda, and M. Tanaka, Highly ordered structure of icosahedral quasicrystals in Zn-Mg-RE (RE: rare earth element) systems, *Phil. Mag. Lett.* **70**, 169 (1994).

[35] I. R. Fisher, Z. Islam, A. F. Panchula, K. O. Cheon, M. J. Kramer, P. C. Canfield, and A. I. Goldman, Growth of large-grain R-Mg-Zn quasicrystals from the ternary melt (R=Y, Er, Ho, Dy, Tb), *Phil. Mag. B* **77**(6), 1601–1615 (1998).

[36] Z. V. Vardeny, A. Nahata, and A. Agrawal, Optics of photonic quasicrystals, *Nature Photonics* **7**(3), 177–187 (2013).

[37] T. Dotera, Toward the discovery of new soft quasicrystals: From a numerical study viewpoint, *Journal of Polymer Science Part B: Polymer Physics* **50**, 155–167 (2012).

[38] L. X. He, X. Z. Li, Z. Zhuang, and K. H. Kuo, One-dimensional quasicrystal in rapidly solidified alloys, *Phys. Rev. Lett.* **61**, 1116–1118 (1988).

[39] A. D. Bianchi, F. Bommeli, E. Felder, M. Kenzelmann, M. A. Chernikov, L. Degiorgi, H. R. Ott, and K. Edagawa, Low-temperature thermal and optical properties of single-grained decagonal Al-Ni-Co quasicrystals, *Phys. Rev. B* **58**(6), 3046–3056 (1998).

[40] C. Janot, *Quasicrystals* (Oxford University Press, 1994).

[41] R. Penrose, The role of aesthetics in pure and applied mathematical research, *Bull. Inst. Math. Appl.* **10**, 266 (1974).

[42] P. Kramer and R. Neri, On periodic and non-periodic space fillings of E^m obtained by projection, *Acta Cryst. A* **40**, 580–587 (1984).

[43] M. Duneau and A. Katz, Quasiperiodic patterns, *Phys. Rev. Lett.* **54**(25), 2688–2691 (1985).

[44] П. А. Калугин, А. Ю. Китаев, Л. С. Левитов, $Al_{0.86}Mn_{0.14}$ – шестимерный кристалл, *Письма в ЖЭТФ* **41**(3), 119–121 (1985).

[45] V. Elser, The diffraction pattern of projected structures, *Acta Crystal. A* **42**, 36–43 (1986).

[46] V. Elser and C. L. Henley, Crystal and quasicrystal structures in Al-Mn-Si alloys, *Phys. Rev. Lett.* **55**(26), 2883–2886 (1985).

[47] C. Henley and V. Elser, Quasicrystal structure of $(Al, Zn)_{49}Mg_{32}$, *Phil. Mag. B* **53**(3), L59–L66 (1986).

[48] V. Elser, Indexing problems in quasicrystal diffraction, *Phys. Rev. B* **32**(8), 4892–4898 (1985).

[49] A. Langsdorf, F. Ritter, and W. Assmus, Determination of the primary solidification area of the icosahedral phase in the ternary phase diagram of Zn-Mg-Y, *Phil. Mag. Lett.* **75**(6), 381–387 (1997).

[50] A. Langsdorf and W. Assmus, Growth of large single grains of the icosahedral quasicrystal ZnMgY, *J. Cryst. Growth* **192**, 152–156 (1998).

[51] S. Brühne, E. Uhrig, K.-D. Luther, W. Assmus, M. Brunelli, A. S. Masadeh, and S. J. L. Billinge, Atom location in quasicrystals from atomic pair distribution function refinement, *ESRF Highlights 2006* (ESRF, 2006), p. 22–23.

[52] S. Brühne, E. Uhrig, C. Gross, and W. Assmus, Local 3D real space atomic structure of the simple icosahedral $Ho_{11}Mg_{15}Zn_{74}$ quasicrystal from PDF data, *Cryst. Res. Technol.* **38**(12), 1023–1036 (2003).

[53] S. Brühne, R. Sterzel, E. Uhrig, C. Gross, and W. Assmus, Medium range real atomic structure of face-centred icosahedral $Ho_9Mg_{26}Zn_{65}$, *Z. Kristallogr.* **219**, 245–258 (2004).

[54] S. Brühne, E. Uhrig, C. Gross, W. Assmus, A. S. Masadeh, and S. J. L. Billinge, The local atomic quasicrystal structure of the icosahedral $Mg_{25}Y_{11}Zn_{64}$ alloy, *J. Phys.: Condens. Matter* **17**, 1561–1572 (2005).

[55] S. Brühne, E. Uhrig, K.-D. Luther, W. Assmus, M. Brunelli, A. S. Masadeh, and S. J. L. Billinge, PDF from X-ray powder diffraction for nanometer-scale atomic structure analysis of quasicrystalline alloys, *Z. Kristallogr.* **220**, 962–967 (2005).

[56] M. Boudard, M. De Boissieu, J. P. Simon, J. F. Berar, and B. Doisneau, Phason strain in a mechanically polished Al-Pd-Mn icosahedral single quasicrystal, *Phil. Mag. Lett.* **74**(6), 429–437 (1996).

[57] A. Létoublon, I. R. Fisher, T. J. Sato, M. de Boissieu, M. Boudard, S. Agliozzo, L. Mancini, J. Gastaldi, P. C. Canfield, A. I. Goldman,

and A.-P. Tsai, Phason strain and structural perfection in the Zn–Mg–rare-earth icosahedral phases, *Materials Science and Engineering A* **294–296**, 127–130 (2000).

[58] M. de Boissieu, S. Francoual, Y. Kaneko, and T. Ishimasa, Diffuse scattering and phason fluctuations in the Zn-Mg-Sc icosahedral quasicrystal and its Zn-Sc periodic approximant, *Phys. Rev. Lett.* **95**, 105503 (2005).

[59] T. Janssen, G. Chapuis, and M. de Boissieu, *Aperiodic Crystals. From Modulated Phases to Quasicrystals* (Oxford University Press, 2007).

[60] T. C. Lubensky, J. E. S. Socolar, P. J. Steinhardt, P. A. Bancel, and P. A. Heiney, Distortions and peak broadening in quasicrystal diffraction patterns, *Phys. Rev. Lett.* **57**(12), 1440–1443 (1986).

[61] M. de Boissieu, Phason modes in quasicrystals, *Phil. Mag.* **88**(13–15), 2295–2309 (2008).

[62] T. Fujiwara, Theory of electronic structure in quasicrystals, *Physical Properties of Quasirystals*, ed. Z. M. Stadnik (Springer, 1999), p. 169–207.

[63] J. Hafner and M. Krajčí, Elementary excitations and physical properties, *Physical Properties of Quasirystals*, ed. Z. M. Stadnik (Springer, 1999), p. 209–256.

[64] Y. Ishii and T. Fujiwara, Electronic structures and stability mechanism of quasicrystals, *Quasicrystals*, eds. T. Fujiwara and Y. Ishii (Elsevier, 2008), p. 171–208.

[65] T. Fujiwara and T. Yokokawa, Universal pseudogap at the Fermi energy in quasicrystals, *Phys. Rev. Lett.* **66**(3), 333–336 (1991).

[66] A. P. Smith and N. W. Ashcroft, Pseudopotentials and quasicrystals, *Phys. Rev. Lett.* **59**(12), 1365–1368 (1987).

[67] A. Suchodolskis, W. Assmus, B. Čechavičius, J. Dalmas, L. Giovanelli, M. Göthelid, U. O. Karlsson, V. Karpus, G. Le Lay, R. Sterzel, and E. Uhrig, Pseudogap structure in icosahedral ZnMgY and ZnMgHo quasicrystals, *Appl. Surf. Sci.* **212–213**, 485–490 (2003).

[68] A. Suchodolskis, W. Assmus, L. Giovanelli, U. O. Karlsson, V. Karpus, G. Le Lay, R. Sterzel, and E. Uhrig, Indication of van Hove singularities in the density of states of ZnMg(Y,Ho) quasicrystals, *Phys. Rev. B* **68**, 054207 (2003).

[69] A. Suchodolskis, W. Assmus, L. Giovanelli, U. O. Karlsson, V. Karpus, G. Le Lay, and E. Uhrig, Valence band structure of i-ZnMgEr quasicrystal: Photoemission study, *J. Phys.: Condens. Matter* **16**, 9137–9142 (2004).

[70] V. Karpus, A. Suchodolskis, J. Taulavičius, U. O. Karlsson, W. Assmus, S. Brühne, and E. Uhrig, Photoemission spectroscopy study of si-ZnMgHo quasicrystals, *Opt. Mater.* **30**(1), 690–692 (2008).

[71] M. Krajčí and J. Hafner, Electronic and magnetic properties of hexagonal rare-earth-Zn-Mg compounds and their relation to the properties of icosahedral alloys, *J. Phys.: Condens. Matter* **12**, 5831–5842 (2000).

[72] K. Oshio and Y. Ishii, Electronic structures of large approximants of Zn-Mg-Y, *J. Alloys Compounds* **341**(1–2), 402–404 (2002).

[73] N. W. Ashcroft and N. D. Mermin, *Solid State Physics* (Holt, Rinehart and Winston, 1976).

[74] A. Suchodolskis, *Photoelectron and Optical Spectroscopy of i-ZnMg(Y,Ho,Er) Quasicrystals*, Doctoral dissertation (Vilnius, 2004).

[75] R. M. A. Azzam and N. M. Bashara. *Ellipsometry and Polarized Light* (North-Holland Publ., 1984).

[76] H. G. Tompkins, *A User's Guide to Ellipsometry* (Academic Press, 1993).

[77] H. Fujiwara, *Spectroscopic Ellipsometry: Principles and Applications* (Wiley, 2007).

[78] V. Karpus, A. Rėza, A. Suchodolskis, G. J. Babonas, W. Assmus, R. Sterzel, V. Kazlauskienė, J. Miškinis, and A. Miniotas, Optical properties of surface layers of i-ZnMg(Y,Ho) quasicrystals, *Materials Science (Medžiagotyra)* **6**(3), 148–152 (2000).

[79] V. Karpus, A. Rėza, G.-J. Babonas, A. Suchodolskis, W. Assmus, R. Sterzel, V. Kazlauskienė, J. Miškinis, and A. Miniotas, Surface oxide layers on *i*-ZnMg(Y,Ho) quasicrystals, *Thin Film Deposition of Oxide Multilayers. Industrial Scale Processing*, eds. B. Vengalis and A. Abrutis (Vilnius University, 2000), p. 142–145.

[80] B. Johs and J. S. Hale, Dielectric function representation by B-splines, *Phys. Stat. Sol. (a)* **205**(4), 715–719 (2008).

[81] K.-E. Peiponen and J. J. Saarinen, Generalized Kramers–Kronig relations in nonlinear optical- and THz-spectroscopy, *Rep. Prog. Phys.* **72**, 056401 (2009).

[82] R. K. Ahrenkiel, Modified Kramers–Kronig analysis of optical spectra, *J. Opt. Soc. Am.* **61**(12), 1651–1655 (1971).

[83] V. Karpus, G.-J. Babonas, L. Rėza, W. Assmus, and R. Sterzel, Dispersion of dielectric function of *i*-ZnMgY quasicrystals, *Lith. J. Phys.* **40**(1–3), 118–123 (2000).

[84] R. V. Kasowski, Temperature-dependent optical properties of Zn and Cd: A theoretical study, *Phys. Rev.* **187**(3), 885–891 (1969).

[85] G. W. Rubloff, Normal-incidence reflectance. Optical properties, and electronic structure of Zn, *Phys. Rev. B* **3**(2), 285–292 (1971).

[86] P. A. Thiel and J.-M. Dubois, Quasicrystals. Reaching maturity for technological applications, *Materials Today* **2**(3), 3–7 (1999).

[87] P. A. Thiel, A. I. Goldman, and C. J. Jenks, Surface science of quasicrystals, *Physical Properties of Quasicrystals*, ed. Z. M. Stadnik (Springer, 1999), p. 327–360.

[88] D. Rouxel and P. Pigeat, Surface oxidation and thin film preparation of AlCuFe quasicrystals, *Progress in Surface Science*, **81**, 488–514 (2006).

[89] J.-M. Frigerio and J. Rivory, Optical properties of Al-Mn quasicrystalline phases prepared by solid state interdiffusion, *J. Non-Cryst. Solids* **117/118**, 812–815 (1990).

[90] C. C. Homes, T. Timusk, X. Wu, Z. Altounian, A. Sahnoune, and J. O. Ström-Olsen, Optical conductivity of the stable icosahedral quasicrystal $Al_{63.5}Cu_{24.5}Fe_{12}$, *Phys. Rev. Lett.* **67**(19), 2694–2696 (1991).

[91] V. Demange, A. Milandri, M. C. de Weerd, F. Machizaud, G. Jeandel, and J. M. Dubois, Optical conductivity of Al-Cr-Fe approximant compounds, *Phys. Rev. B* **65**(14), 144205 (2002).

[92] L. Degiorgi, M. A. Chernikov, C. Beeli, and H. R. Ott, The electrodynamic response of the icosahedral quasicrystal $Al_{70}Mn_9Pd_{21}$, *Solid State Commun.* **87**(8), 721–726 (1993).

[93] M. A. Chernikov, L. Degiorgi, A. Bernasconi, C. Beeli, and H. R. Ott, DC and optical conductivity of icosahedral $Al_{70}Mn_9Pd_{21}$, *Physica B* **194–196**, 405–406 (1994).

[94] D. N. Basov, F. S. Pierce, P. Volkov, S. J. Poon, and T. Timusk, Optical conductivity of insulating Al-based alloys: Comparison of quasiperiodic and periodic systems, *Phys. Rev. Lett.* **73**(13), 1865–1868 (1994).

[95] H. Werheit, R. Schmechel, K. Kimura, R. Tamura, and T. Lundström, On the electronic properties of icosahedral quasicrystals, *Solid State Commun.* **97**(2), 103–107 (1996).

[96] A. D. Bianchi, F. Bommeli, M. A. Chernikov, U. Gubler, L. Degiorgi, and H. R. Ott, Electrical, magneto-, and optical conductivity of quasicrystals in the Al-Re-Pd system, *Phys. Rev. B* **55**(9), 5730–5735 (1997).

[97] X. Wu, C. C. Homes, S. E. Burkov, T. Timusk, F. S. Pierce, S. J. Poon, S. L. Cooper, and M. A. Karlow, Optical conductivity of the icosahedral quasicrystal $Al_{75.5}Mn_{20.5}Si_4$ and its 1/1 crystalline approximant α-$Al_{72.5}Mn_{17.4}Si_{10.1}$, *J. Phys.: Condens. Matter* **5**, 5975–5990 (1993).

[98] D. N. Basov, T. Timusk, F. Barakat, F. J. Greedan, and B. Grushko, Anisotropic optical conductivity of decagonal quasicrystals, *Phys. Rev. Lett.* **72**(12), 1937–1941 (1994).

[99] A. Suchodolskis, W. Assmus, G.-J. Babonas, L. Giovanelli, U. O. Karlsson, V. Karpus, G. Le Lay, A. Rėza, and E. Uhrig, Photoemission and optical spectroscopy of i-ZnMgEr quasicrystal, *Acta Phys. Pol. A* **107**(2), 412–419 (2005).

[100] M. A. Chernikov, S. Paschen, E. Felder, P. Vorburger, B. Ruzicka, L. Degiorgi, H. R. Ott, I. R. Fisher, and P. C. Canfield, Low-temperature transport, thermal, and optical properties of single-grain quasicrystals of icosahedral phases in the Y-Mg-Zn and Tb-Mg-Zn alloy systems, *Phys. Rev. B* **62**(1), 262–272 (2000).

[101] T. Fujiwara, S. Yamamoto, and G. T. de Laissardière, Band structure effects of transport properties in icosahedral quasicrystals, *Phys. Rev. Lett.* **71**(25), 4166–4169 (1993).

[102] S. E. Burkov, T. Timusk, and N. W. Ashcroft, Optical conductivity of icosahedral quasi-crystals, *J. Phys.: Condens. Matter* **4**, 9447–9458 (1992).

[103] A. Langsdorf, W. Assmus, G. J. Babonas, and A. Rėza, Structural and optical properties of Bridgman-grown Zn-Mg-Y quasicrystals, *Lith. J. Phys.* **37**(1), 40–45 (1997).

[104] V. Karpus, G. J. Babonas, A. Rėza, W. Assmus, A. Langsdorf, O. Hunderi, and E. Wold, Optical properties of ZnMgY quasicrystals and related compounds, *Lith. J. Phys.* **37**(6), 463–466 (1997).

[105] N. W. Ashcroft and K. Sturm, Interband absorption and the optical properties of polyvalent metals, *Phys. Rev. B* **3**(6), 1898–1910 (1971).

[106] M. H. Cohen, Optical constants, heat capacity and the Fermi surface, *Phil. Mag.* **3**(31), 762–775 (1958).

[107] H. Ehrenreich, H. R. Philipp, and B. Segall, Optical properties of aluminum, *Phys. Rev.* **132**(5), 1918–1928 (1963).

[108] H. Ehrenreich and M. H. Cohen, Self-consistent field approach to the many-electron problem, *Phys. Rev.* **115**(4), 786–790 (1959).

[109] H. Ehrenreich and H. R. Philipp, Optical properties of Ag and Cu, *Phys. Rev.* **128**(4), 1622–1629 (1962).

[110] P. N. Butcher, The absorption of light by alkali metals, *Proc. Phys. Soc. (London) A* **64**(381A), 756–772 (1951).

[111] W. A. Harrison, Parallel-band effects in interband optical absorption, *Phys. Rev.* **147**(2), 467–469 (1966).

[112] А. И. Головашкин, А. И. Копелиович, Г. П. Мотулевич, Определение Фурье-компонент псевдопотенциала по межзонным переходам в оптической области, *ЖЭТФ* **53**(6), 2053–2062 (1967).

[113] I. R. Fisher, K. O. Cheon, A. F. Panchula, P. C. Canfield, M. Chernikov, H. R. Ott, and K. Dennis, Magnetic and transport properties of single-grain R-Mg-Zn icosahedral quasicrystals [R = Y, $(\mathrm{Y}_{1-x}\mathrm{Gd}_x)$, $(\mathrm{Y}_{1-x}\mathrm{Tb}_x)$, Tb, Dy, Ho, and Er], *Phys. Rev. B* **59**(1), 308–321 (1999).